



**HAL**  
open science

# Effects of TiB<sub>2</sub> nanoparticles on the interfacial precipitation and mechanical properties of Al-Zn-Mg-Cu matrix composites

Yu Ma

► **To cite this version:**

Yu Ma. Effects of TiB<sub>2</sub> nanoparticles on the interfacial precipitation and mechanical properties of Al-Zn-Mg-Cu matrix composites. Material chemistry. Université Paris Saclay (COMUE), 2019. English. NNT : 2019SACLS252 . tel-03793792

**HAL Id: tel-03793792**

**<https://theses.hal.science/tel-03793792>**

Submitted on 2 Oct 2022

**HAL** is a multi-disciplinary open access archive for the deposit and dissemination of scientific research documents, whether they are published or not. The documents may come from teaching and research institutions in France or abroad, or from public or private research centers.

L'archive ouverte pluridisciplinaire **HAL**, est destinée au dépôt et à la diffusion de documents scientifiques de niveau recherche, publiés ou non, émanant des établissements d'enseignement et de recherche français ou étrangers, des laboratoires publics ou privés.

# Effects of $TiB_2$ nanoparticles on the interfacial precipitation and mechanical properties of Al-Zn- Mg-Cu matrix composites

Thèse de doctorat de l'Université Paris-Saclay  
préparée à Université Paris Sud

École doctorale n°571 Sciences chimiques : molécules, matériaux,  
instrumentation et biosystèmes (2MIB)  
Spécialité de doctorat : Chimie

Thèse présentée et soutenue à Orsay Ville, le 19 Sep. 2019, par

**M. Yu MA**

Composition du Jury :

|   |                       |
|---|-----------------------|
| <b>Mme. Anne-Laure HELBERT</b><br>Professeur, Université Paris-Sud                | Président             |
| <b>M. Jean-François SILVAIN</b><br>Directeur de Recherche, CNRS Bordeaux          | Rapporteur            |
| <b>M. Rajashekhara SHABADI</b><br>Maitre de Conférences, HDR, Université de Lille | Rapporteur            |
| <b>M. Zhe CHEN</b><br>Professeur Associé, Shanghai Jiaotong University            | Examineur             |
| <b>M. Gang JI</b><br>Chargé de Recherche, HDR, CNRS Lille                         | Co-Directeur de thèse |
| <b>M. Vincent JI</b><br>Professeur, Université Paris-Sud                          | Co-Directeur de thèse |
| <b>M. Ahmed ADDAD</b><br>Ingénieur, CNRS Lille                                    | Invité                |

**Titre :** Effet de nanoparticules  $\text{TiB}_2$  sur la précipitation interfaciale et les propriétés mécaniques des composites à matrice de Al-Zn-Mg-Cu

**Mots clés :** Alliage d'aluminium, Composite à matrice métallique, Nanoparticules, Précipitation interfaciale, Renforcement de l'interface, Fissuration sous chargement de fatigue

**Résumé :** L'influence des renforts nanoparticules de  $\text{TiB}_2$  (6 wt.%) sur la précipitation interfaciale de la phase  $(\text{Zn}_{1.5}\text{Cu}_{0.5})\text{Mg}$ , la résistance à la traction et la fissuration sous chargement de fatigue (fatigue crack growth-FCG) des composites à matrice de Al-Zn-Mg-Cu ont été étudiées. Des échantillons de composites ont été obtenus par réaction in-situ pendant le moulage suivi d'un FSP (friction stir processing) et une extrusion à chaud. Seuls les échantillons moulés et extrudés ont été utilisés pour étude de FCG à cause de la limitation de la taille après FSP. Des observations au microscope électronique à balayage (SEM), avec la diffraction des électrons rétrodiffusés (SEM/EBSD) et au microscope électronique en transmission à haute résolution (HRSTEM) ont été réalisées pour caractériser la microstructure.

Des échantillons présentent une structure des grains équi-axiaux et des nanoparticules de  $\text{TiB}_2$  sont distribuées de façon homogène dans la matrice. En état de solution solide, l'interface  $\text{TiB}_2/\text{Al}$  est de nature semi-cohérente et très propre. En état de vieillissement

ou sur vieillissement, la précipitation interfaciale hétérogène de la phase  $(\text{Zn}_{1.5}\text{Cu}_{0.5})\text{Mg}$  a été observée. La cinétique de la précipitation interfaciale a été discutée. Les interfaces entre  $\text{Al}/(\text{Zn}_{1.5}\text{Cu}_{0.5})\text{Mg}/\text{TiB}_2$  sont quasi cohérentes et l'interface  $\text{TiB}_2/\text{Al}$  a été renforcée grâce à la réduction de l'énergie de l'interface. Ce mécanisme de précipitation interfaciale peut expliquer l'effet de renforcement de l'interface contribuant simultanément l'augmentation de la résistance et de l'élongation des échantillons de composite.

La majorité de nanoparticules  $\text{TiB}_2$  tentent de s'agglomérer le long des joints de grains dans des échantillons sans FSP. La vitesse de croissance de fissure a été augmentée à l'intérieur des grains avec un facteur d'intensité ( $\Delta K$ ) intermédiaire ou important à cause de l'affinement de grains. Cependant, la vitesse de croissance de fissure a été diminuée aux joints de grains avec ( $\Delta K$ ) faible ou intermédiaire à cause de la présence des clusters de  $\text{TiB}_2$  tandis que cette vitesse augmente avec ( $\Delta K$ ) important à cause de la coalescence des micropores.

**Title :** Effects of  $\text{TiB}_2$  nanoparticles on the interfacial precipitation and mechanical properties of Al-Zn-Mg-Cu matrix composites.....

**Keywords :** Aluminum alloy, Metal matrix composites, Nanoparticles, Interface precipitation, Interface strengthening, Fatigue crack growth

**Abstract :** The influences of  $\text{TiB}_2$  reinforcement nanoparticles (6 wt.%) on the interfacial precipitation of  $(\text{Zn}_{1.5}\text{Cu}_{0.5})\text{Mg}$  phase, the associated tensile and fatigue crack growth (FCG) properties of the Al-Zn-Mg-Cu matrix composites have been studied. The composite samples were produced by in-situ reaction during casting followed by friction stir processing (FSP) and hot extrusion, while only casted and extruded samples were used for evaluating FCG due to size limit of the nugget zone after FSP. Scanning electron microscopy (SEM), electron backscatter diffraction (EBSD) and high-resolution scanning transmission electron microscopy (HRSTEM) were employed for the microstructure characterization.

The as-processed composite samples contain the fine equiaxed-grain structure, where  $\text{TiB}_2$  nanoparticles are homogeneously distributed. At solid-solution state, the  $\text{TiB}_2/\text{Al}$  interfaces are featured by the clean and semi-coherent nature. At the peak-aged and overaged states,

the interface precipitate determined as  $(\text{Zn}_{1.5}\text{Cu}_{0.5})\text{Mg}$  phase was formed, and the underlying heterogeneous interfacial precipitation kinetics was discussed. The  $\text{Al}/(\text{Zn}_{1.5}\text{Cu}_{0.5})\text{Mg}/\text{TiB}_2$  multi-interfaces were revealed to be almost coherent, and the  $\text{TiB}_2/\text{Al}$  interfaces were thus strengthened due to the greatly reduced coherency strains. This mechanism was proposed as precipitation assisted interface strengthening, which has contributed to the simultaneously enhanced tensile strength and uniform elongation of the as-processed composite.

The majority of  $\text{TiB}_2$  nanoparticles tend to aggregate along grain boundaries (GBs) in the composite samples without FSP. The FCG rate is increased inside grains at intermediate and high stress intensity factor ( $\Delta K$ ) ranges due to the refined grain size. However, the FCG rate at the GBs is decreased at the low and intermediate  $\Delta K$  ranges by fatigue crack deflection and trapping due to the presence of  $\text{TiB}_2$  clusters, while it increases at the high  $\Delta K$  range due to microvoid coalescence.

# CONTENT

|   |           |
|---|-----------|
| <b>Chapter 1 General Introduction.....</b>  | <b>1</b>  |
| <b>Chapter 2 Literature Review .....</b>  | <b>5</b>  |
| 2.1 Al-Zn-Mg(-Cu) alloys .....  | 5         |
| 2.1.1 Development history of Al-Zn-Mg(-Cu) alloys.....  | 5         |
| 2.1.2 Precipitation reactions in Al-Zn-Mg(-Cu) alloys.....  | 7         |
| 2.2 TiB <sub>2</sub> reinforcement phase.....   | 9         |
| 2.3 TiB <sub>2</sub> /Al composites .....   | 9         |
| 2.3.1 Development history of TiB <sub>2</sub> /Al composites.....   | 9         |
| 2.3.2 Investigations on TiB <sub>2</sub> /Al interfaces.....  | 10        |
| <b>Chapter 3 Methodology of Research.....</b>   | <b>13</b> |
| 3.1 Material processing .....   | 13        |
| 3.2 Sample preparation.....   | 15        |
| 3.2.1 SEM and EBSD sample preparation.....  | 16        |
| 3.2.2 STEM sample preparation .....   | 16        |
| 3.2.3 Tensile and FCG tests sample preparation.....   | 16        |
| 3.3 Experimental methods.....   | 17        |
| 3.3.1 SEM and EBSD .....  | 17        |
| 3.3.2 STEM.....   | 18        |
| 3.3.3 Tensile and FCG tests .....   | 19        |
| <b>Chapter 4 Atomic-scale Investigation of the Interface Precipitation in a TiB<sub>2</sub> Nanoparticles Reinforced Al-Zn-Mg-Cu Matrix Composite..</b> | <b>21</b> |
| 4.1 Introduction .....  | 22        |
| 4.2 Experimental procedure .....  | 25        |
| 4.2.1 Materials processing .....  | 26        |
| 4.2.2 Microstructure characterization .....   | 26        |
| 4.3 Results .....   | 27        |
| 4.3.1 The TiB <sub>2</sub> /Al interface structure in the solid-solution treated composite ....   | 27        |
| 4.3.2 The TiB <sub>2</sub> /Al interface structures in the peak-aged and over-aged  |           |

|  |           |
|--|-----------|
| composites.....  | 29        |
| 4.3.2.1 Structure determination of the formed interphase precipitate.....  | 30        |
| 4.3.2.2 OR-dependent precipitations at the TiB <sub>2</sub> /Al interfaces .....   | 32        |
| 4.3.2.3 Atomic structure of the Al/(Zn <sub>1.5</sub> Cu <sub>0.5</sub> )Mg interphase/TiB <sub>2</sub> multi-<br>interfaces .....   | 35        |
| 4.4 Discussion.....  | 40        |
| 4.4.1 Reduced nucleation energy barrier for the interphase precipitation .....   | 41        |
| 4.4.2 Accelerated growth rate for the interphase precipitation .....   | 42        |
| 4.4.3 Preferential TiB <sub>2</sub> /Al interfaces for suppressing the interphase precipitation<br>.....   | 44        |
| 4.4.4 Crystallographic ORs between TiB <sub>2</sub> nanoparticles, interphase and Al alloy<br>matrix .....   | 45        |
| 4.4.5 Effect of the aging conditions on the interphase evaluation .....  | 47        |
| 4.5 Conclusions .....  | 48        |
| <b>Chapter 5 Simultaneously Increasing the Strength and Ductility of<br/>TiB<sub>2</sub> Nanoparticles Reinforced Al-Zn-Mg-Cu Matrix Composite via<br/>Precipitation-assisted Interface Strengthening.....</b> | <b>50</b> |
| 5.1 Introduction .....   | 50        |
| 5.2 Experimental procedure .....   | 52        |
| 5.3 Results .....  | 54        |
| 5.3.1 Tensile properties.....  | 54        |
| 5.3.2 Microstructure.....  | 55        |
| 5.4 Discussion.....  | 59        |
| 5.4.1 Precipitation assisted interface strengthening.....  | 59        |
| 5.4.2 Mechanisms for high strength and ductility.....  | 60        |
| 5.5 Conclusion.....  | 63        |
| <b>Chapter 6 Study of the Mechanisms of Nanoparticles Influencing<br/>Fatigue Crack Growth in TiB<sub>2</sub>/Al-Zn-Mg-Cu Composite .....</b>  | <b>65</b> |
| 6.1 Introduction .....   | 65        |
| 6.2 Experimental procedure .....   | 67        |
| 6.2.1 Materials processing and heat treatment.....   | 68        |

|   |            |
|---|------------|
| 6.2.2 Sample preparation and fatigue crack growth testing.....                    | 68         |
| 6.2.3 Microstructure characterization .....                                       | 69         |
| <b>6.3 Results .....</b>  | <b>70</b>  |
| 6.3.1 Microstructure.....   | 70         |
| 6.3.2 Fatigue crack growth rate.....  | 74         |
| 6.3.3 Fractographic features of crack propagation.....                            | 75         |
| <b>6.4 Discussion.....</b>  | <b>77</b>  |
| 6.4.1 FCG inside grains .....   | 77         |
| 6.4.2 FCG at GBs.....   | 80         |
| 6.4.2.1 Reduced FCG rate at low $\Delta K$ range.....                             | 80         |
| 6.4.2.2 Reduced FCG rate at intermediate $\Delta K$ range.....                    | 82         |
| 6.4.2.3 Increased FCG rate at high $\Delta K$ range .....                         | 83         |
| <b>6.5 Conclusion.....</b>  | <b>86</b>  |
| <b>Chapter 7 Conclusion and Prospect.....</b>                                     | <b>88</b>  |
| 7.1 Conclusion.....   | 88         |
| 7.2 Remark .....  | 91         |
| 7.2.1 Effects of TiB <sub>2</sub> nanoparticles on interfacial precipitation..... | 91         |
| 7.2.2 Effects of TiB <sub>2</sub> nanoparticles on tensile properties.....        | 91         |
| 7.2.3 Effects of TiB <sub>2</sub> nanoparticles on FCG .....                      | 92         |
| 7.2.4 General remark.....   | 92         |
| 7.3 Prospect of future work .....   | 93         |
| <b>References.....</b>  | <b>95</b>  |
| <b>Index of Abbreviations .....</b>   | <b>110</b> |
| <b>Acknowledgements .....</b>   | <b>112</b> |
| <b>Résumé en Français .....</b>   | <b>113</b> |

# Chapter 1 General Introduction

Aluminum (Al) alloys have been one of the most important structural materials in the past century due to their low density, remarkable corrosion resistance and abundant reserves on earth. Among them, age-hardenable Al alloys (e.g., 2xxx, 6xxx and 7xxx series) are widely applied in space, aeronautic and automobile industries considering their superior strength and good ductility [1-3]. It has been well established that precipitation hardening, i.e., a homogenous distribution of nanoscale precipitates originating from solid-state precipitation reactions during aging treatments, is one of the most effective strengthening mechanisms in age-hardenable Al alloys [4-6].

Subsequently, micron- (or submicron-)sized reinforcement particles (MRPs), such as SiC, Al<sub>2</sub>O<sub>3</sub> and B<sub>4</sub>C, have been successfully introduced into the matrix of age-hardenable Al alloys, aiming to further enhance the specific stiffness, specific strength and fatigue limit in order to meet the growing requirements in industrial applications [7-11]. However, it should be noted that the thermoelastic stress induced dislocations (TSIDs) and the incoherent MRP/Al interfaces have been widely reported to critically influence the precipitation reactions in the surrounding Al alloys matrix by promoting the formation of coarse precipitate zones (CPZs) and precipitate free zones (PFZs), respectively [12-22]. In addition, although the introduced MRPs can improve the tensile strength, the concurrently formed MRP/Al interfaces become the dominant defects and thereby severely reduce the ductility of the Al-based metal matrix composites (MMCs) [23, 24]. Moreover, numerous studies have confirmed that the fatigue crack growth (FCG) resistance of MRPs reinforced Al-based MMCs is deteriorated at the intermediate and high stress intensity factor ( $\Delta K$ ) ranges due to the MRP fracture and MRP/Al interface debonding under cyclic stress [25-27].

In parallel with the developments in nanotechnology, the dimensions of reinforcement particles (RPs) have decreased from micron/submicron scale to

nanoscale ( $\leq 100$  nm) over the last decades [28, 29]. The presence of nanosized reinforcement particles (NRPs) is supposed to have disparate influences on precipitation reactions in the surrounding Al alloys matrix, and in turn, the macroscopic mechanical properties of Al-based MMCs considering the NRP/Al interface structure is very different from the MRP/Al one. For example, Kim *et al.* [30] proposed that the intensity of TSIDs shows a strong particle size dependence. The TSIDs density increases significantly only when the size of RPs reaches the micron level. For the NRPs reinforced Al-based MMCs, the thermoelastic stress can be lower than the effective yield stress such that no TSIDs and no CPZ (caused by TSIDs) in the surrounding matrix should be generated [31, 32]. Notably, it has been well documented that the CPZs formation is detrimental for mechanical properties of MMCs [33-35]. Thus, it is expected that their absence in NRPs reinforced Al-based MMCs should be conducive to their mechanical performance.

In addition, unlike the MRP/Al interface, it has been well established that NRPs generally have preferential crystallographic orientation relationships (ORs) with the Al alloy matrix [28, 36]. Meanwhile, the phase interfaces are effective heterogeneous precipitation sites. As such, it is of theoretical possibility to have ORs in between the NRPs, interface precipitates and Al alloys matrix to minimize nucleation energy barrier [37, 38]. Hence, the NRP/Al interfaces can be strengthened, which is also beneficial for the mechanical properties of the Al-based MMCs. Moreover, it is worth noting that the volume fraction of particle/matrix interfaces increases proportionally as:  $V_2 = (r_1/r_2)^3 V_1$ , where  $r_1$  and  $r_2$  are the radius of spherical reinforcements with different dimensions,  $V_1$  and  $V_2$  are the corresponding interface volumes of the spherical reinforcements [39]. Thus, it is expected that structure evolution of NRP/Al interfaces during the aging treatment can play an increasingly important role in influencing mechanical properties (e.g., tensile and fatigue properties) of the Al-based MMCs. However, no experimental evidences at the nano- and atomic scales of the influences of NRPs on the interfacial precipitation and furthermore, macroscopic mechanical

properties of NRPs reinforced Al-based MMCs have been properly revealed up to now, which constitutes these most important fundamental problems still unclear.

In view of the discussions above, the present thesis aims to provide a fundamental insight into the effects of NRPs on the interfacial precipitation, tensile properties and FCG behaviors of Al-based MMCs. With high melting point (3173 K), high modulus (565 GPa), high hardness (2500 HV) and good thermal stability [40], TiB<sub>2</sub> nanoparticles have widely been used in Al-based MMCs [41-43]. Meanwhile, Al-Zn-Mg-Cu series alloys possess the highest strength and an excellent ductility in age-hardenable Al alloys. Consequently, the TiB<sub>2</sub> nanoparticles reinforced Al-Zn-Mg-Cu alloy matrix composite (TiB<sub>2</sub>/Al-Zn-Mg-Cu nanocomposite) has been the most ideal model materials for this investigation. Correspondingly, the literature review in Chapter 2 summarizes the development history and precipitation reactions of Al-Zn-Mg(-Cu) alloys, the essential information about TiB<sub>2</sub> reinforcement phase, TiB<sub>2</sub>/Al composites and TiB<sub>2</sub>/Al interfacial characteristics. Chapter 3 introduces the material processing procedure, the mechanical testing methods and the characterization methods. Scanning electron microscopy (SEM), electron backscatter diffraction (EBSD) and transmission electron microscopy (TEM) were employed for microstructure characterization. In particular, high-resolution scanning TEM (HRSTEM) was used in order to provide a fundamental insight (at the atomic scale) into the effects of TiB<sub>2</sub> nanoparticles on the heterogeneous interfacial precipitation during ageing treatments, and in turn, macroscopic mechanical properties of the TiB<sub>2</sub>/Al-Zn-Mg-Cu nanocomposite. Chapter 4-6 are three articles published or in submission based on the work of this thesis. Chapter 4 and Chapter 5 aim to provide a fundamental insight into the effects of uniformly distributed NRPs on interface precipitation and tensile properties of Al-based MMCs. For reaching this goal, the model material, i.e. Al-Zn-Mg-Cu alloy matrix composite reinforced with 6wt. % uniformly distributed TiB<sub>2</sub> nanoparticles, was successfully produced by *in-situ* reaction during casting followed by friction stir processing (FSP) and hot extrusion and systematically examined at the solid-solution, peak-aged and overaged states. Our

results demonstrate that the  $\text{TiB}_2$  nanoparticles have a significant impact on the precipitation in the adjacent matrix next to the  $\text{TiB}_2/\text{Al}$  interface. The misfit dislocations at the  $\text{TiB}_2/\text{Al}$  interfaces have promoted the heterogeneous precipitation at certain  $\text{TiB}_2/\text{Al}$  interfaces, and the interface precipitate (interphase) was determined as  $(\text{Zn}_{1.5}\text{Cu}_{0.5})\text{Mg}$  phase. It is also found that the mismatch of the  $\text{Al}/\text{interphase}/\text{TiB}_2$  multi-interfaces are greatly reduced compared to the original  $\text{TiB}_2/\text{Al}$  interfaces, i.e., the  $\text{TiB}_2/\text{Al}$  interfaces are greatly strengthened by the heterogeneous interface precipitation considering the significantly reduced coherency strains. Correspondingly, the  $\text{TiB}_2/\text{Al}-\text{Zn}-\text{Mg}-\text{Cu}$  nanocomposite presents a remarkable combination of strength (yield strength of 600 MPa) and ductility (uniform elongation of 12%), being higher than any Al or Al based materials ever reported. Chapter 6 investigated the effects of NRPs on the FCG property of Al-based MMCs. Due to size limit of the nugget zone after FSP, the model material, i.e., an Al-Zn-Mg-Cu alloy matrix composite reinforced with 6wt. %  $\text{TiB}_2$  nanoparticles, was produced by *in-situ* reaction during casting directly followed by hot extrusion and examined at the peak-aged state. The majority of  $\text{TiB}_2$  nanoparticles tend to aggregate along grain boundaries (GBs) due to the lack of FSP. The FCG rate of the as-process composite is increased inside grains at intermediate and high  $\Delta K$  ranges due to the refined grain size. However, the FCG rate at GBs is decreased at low and intermediate  $\Delta K$  ranges by fatigue crack deflection and fatigue crack trapping respectively due to the coexisting  $\text{TiB}_2$  bands, while it increases at the high  $\Delta K$  range due to microvoid coalescence. Chapter 7 is the conclusion and remark and the prospect of future work.

# Chapter 2 Literature Review

## 2.1 Al-Zn-Mg(-Cu) alloys

### 2.1.1 Development history of Al-Zn-Mg(-Cu) alloys

Al-Zn-Mg(-Cu) alloys (i.e., 7xxx series Al alloys), have been widely used as structural materials in aerospace and other transportation applications in the past century, partly due to their high strength and relatively low density [44-46]. The development history of Al-Zn-Mg(-Cu) alloys are concluded as follows.

In 1926, the German scientists Sander and Meissner found that the Al-Zn-Mg alloy showed very high strength after quenching and aging treatment. This phenomenon was attributed to the precipitation of  $MgZn_2$  phase during the heat treatment [44]. In 1932, Webber improved the corrosion resistance of Al-Zn-Mg alloy by adding Cu element. This is the first kind of high strength Al-Zn-Mg-Cu alloy in history. The yield strength, ultimate tensile strength and elongation of this Al-Zn-Mg-Cu alloy were up to 549 MPa, 588 MPa and 6%, respectively [46]. However, these materials were not actually applied in industry because of their relatively strong stress corrosion cracking (SCC).

Until 1936, Igarashi [47] at Sumitomo Metal invented the highest strength (over 600MPa) Al alloy on earth, the extra super duralumin (ESD) with a chemical composition of Al-8%Zn-1.5%Mg-2.0%Cu-0.5%Mn. This Al alloy contains 0.25% chromium in order to prevent the SCC. The ESD was immediately applied to the main wings of Zero fighters in World War II for the first time in the world [47]. In 1943, the 7075Al alloy was developed by the United States and subsequently used on the B29 aircraft, which was also used in the Pacific Theater during World War II. Soon afterwards, a higher-strength 7178Al alloy was developed and used for the upper wing structure of the Boeing 707 [48]. During the same period, France also developed a similar alloy with a chemical composition of Al-7.8%Zn-2%Mg-1.5%Cu-0.25%Cr.

The improving requirement for strength, fracture toughness and SCC resistance, caused the development of some new 7075Al derivative alloys (7175Al alloy, forgings; 7475Al alloy, mill products). In 1969, the 7475Al alloy, which showed the highest fracture toughness in 7xxx series alloys, was developed in the United States owe to the tighter control over impurity levels. Subsequently, it was applied to the military aircraft by Europe and America army. In 1971, based on the 7075Al alloy, the United States developed the famous 7050Al alloy by increasing the content of Zn and Cu, and replacing 0.2%Cr with 0.1%Zr, in order to refine the grain size, improve the fracture toughness and solve the problem of quenching sensitivity. The 7050Al alloy shows considerably high strength, stress corrosion resistance and fracture toughness [45]. During this period, the Al-Zn-Mg-Cu alloys developed fast and were widely applied to the aircraft industry.

Since the mid-1970s, the researches focused on improving the already existed Al-Zn-Mg-Cu alloys by exerting tighter control on alloying component and impurity elements such as iron and silicon, and developing new heat treatment technology. In 1978, the 7150Al alloy was developed by adjusting alloying component and reducing the content of Fe and Si. The fracture toughness and exfoliation corrosion resistance of the 7150Al alloy were improved, and it was applied to Boeing 757, Boeing 767 and Airbus A301 [49]. In the 1980s, by further reducing the Fe and Si content and increasing the Zn/Mg element ratio of 7150Al alloy, the America company developed the 7055Al alloy. The strength of the 7055Al alloy was improved 10% and 30% compared to the 7150Al and 7075Al alloy, respectively. The fracture toughness and FCG resistance of the 7055Al alloy were also very high [45]. In addition, the improvements in thermomechanical and heat-treatment practices (e.g., T74, T76, and T77) also played important roles in the further improving the mechanical performance of Al-Zn-Mg-Cu alloys. For example, the 7055-T77 alloy showed the highest strength of any commercially available 7xxx series alloys, with good combinations of fracture toughness and SCC capabilities [49]. It was applied by Boeing for the upper wing skins

and other components of the Boeing 777. Fig. 2.1 shows the Al-Zn-Mg-Cu alloys and tempers used on the Boeing 777 [50].

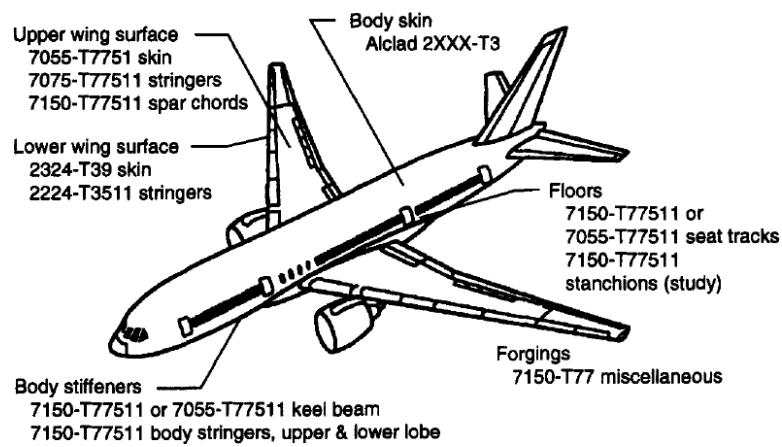


Fig. 2.1 Al-Zn-Mg-Cu alloys and tempers used on the Boeing 777 [50].

### 2.1.2 Precipitation reactions in Al-Zn-Mg(-Cu) alloys

Precipitation strengthening is one of the most important strengthening mechanisms in Al-Zn-Mg(-Cu) alloys. Homogeneously distributed nanoscale precipitates play an role as obstacles to dislocation motion, generate in the Al alloy matrix during heat treatment and therefore strengthen the Al-Zn-Mg(-Cu) alloys [4].

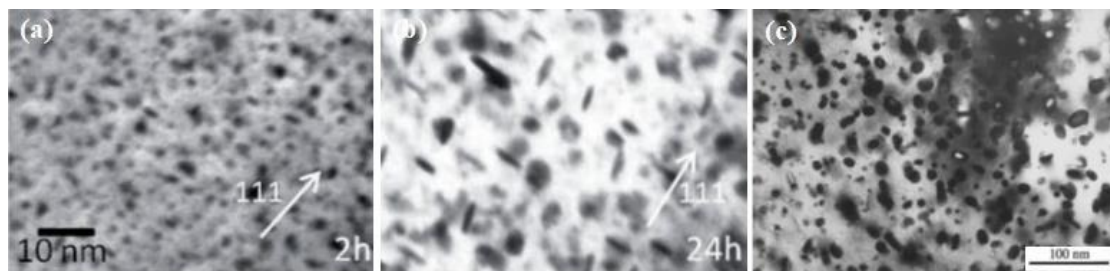


Fig. 2.2 TEM images of (a) GP zones at underaged state, (b)  $\eta'$  phase at peak-aged state [51] and (c)  $\eta$  phase at overaged state [52].

The precipitation sequence in Al-Zn-Mg(-Cu) alloys has been well studied and can be summarized as follows: supersaturated solid solution (SSS)  $\rightarrow$  Guinier-Preston (GP) zones  $\rightarrow$  metastable  $\eta'$  phase ( $\text{MgZn}_{1-2}$ )  $\rightarrow$  stable  $\eta$  phase ( $\text{MgZn}_2$ ) [6, 53, 54]. The TEM images showing the corresponding precipitation sequence in Al-Zn-Mg(-Cu) alloys are given in Fig. 2.2. The GP zones are isostructural with the Al matrix while the

intermediate or equilibrium precipitate phases have different crystal structures. Therefore, the GP zones have a lower interfacial energy than the intermediate or equilibrium precipitate [55]. As a result, the nucleation energy barrier for GP zones is very small. The precipitation sequence in Al-Zn-Mg(-Cu) alloys therefore starts with the precipitation of coherent metastable Guinier-Preston (GP) zones with the size in the order of a few nanometers [56, 57]. Subsequently, the fully coherent GP zones are replaced by the metastable semi-coherent  $\eta'$  ( $\text{MgZn}_{1-2}$ ) phase, which has a size around 8-10 nm [52, 58]. When the Al-Zn-Mg(-Cu) alloys are subject to higher aging temperature and longer aging time, the incoherent equilibrium hexagonal  $\eta$  ( $\text{MgZn}_2$ ) phase showing a size larger than 50 nm forms from  $\eta'$  phase [59]. The aging kinetics in Al-Zn-Mg(-Cu) alloys can be accelerated with the elevated aging temperature [60].

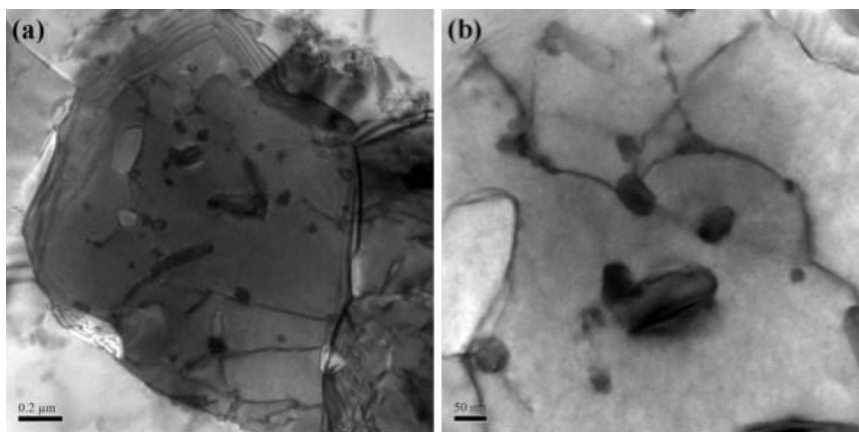


Fig. 2.3 (a) TEM images show the precipitates are either on the dislocations or in the vicinity of dislocations. (b) Higher magnification image of (a) [61].

Notably, it has been well established that precipitation reactions in Al-Zn-Mg(-Cu) alloys are particularly sensitive to the existence of structural defects (e.g., dislocations, grain boundaries and inclusion/matrix interfaces) [62, 63]. These defects can alter the precipitation sequence either by heterogenous precipitation or by modification of bulk precipitation kinetics [52, 58]. The structural defects act as sinks to absorb and cause the annihilation of vacancies surrounding them [52, 64]. Considering the strong influence of vacancy concentration on the precipitation of GP zones [55, 61], the presence of structural defects thus causes the surrounding PFZs due to solute depletion

[63, 65]. On the other hand, the interaction between defects and solutes can result in a solute flux towards defects [66-69], leading to the faster and coarser precipitation, and therefore, the formation of CPZs near the defects [53, 54, 70]. Fig. 2.3 shows the coarse precipitates precipitated either on the dislocations or in the vicinity of dislocations [61].

## 2.2 TiB<sub>2</sub> reinforcement phase

Titanium diboride (TiB<sub>2</sub>) is well known as a ceramic material with relatively high strength and durability as characterized by the relatively high values of its melting point, hardness, strength to density ratio, and wear resistance [41-43]. Commonly, TiB<sub>2</sub> phase is fabricated by in-situ processing technologies [28, 71]. TiB<sub>2</sub> exhibits hexagonal symmetry with space group P6/mmm. The lattice parameters are as follows:  $a=b\neq c$ ,  $\alpha=\beta=90^\circ$ ,  $\gamma=120^\circ$ , 1 formula unit per cell, Ti at (0,0,0), B at (1/3,2/3,1/2) and (2/3,1/3,1/2) [72, 73]. The SEM and TEM images showing the morphology of the TiB<sub>2</sub> phase are presented in Fig. 2.4a and Fig. 2.4b, respectively [74].

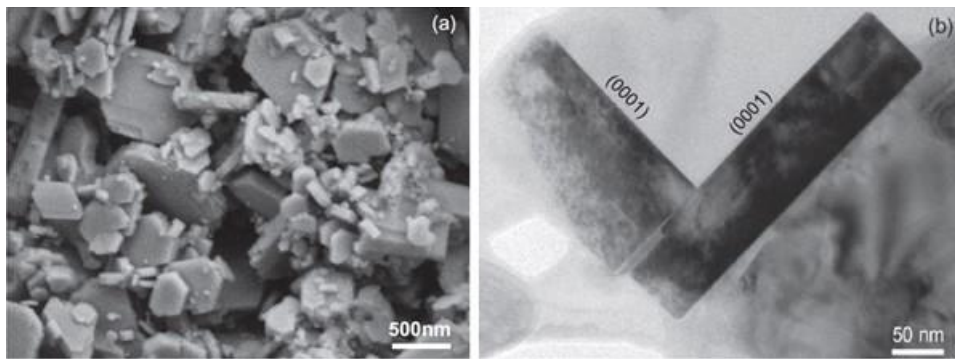


Fig. 2.4. (a) SEM image and (b) TEM image presenting the hexagonal morphology of TiB<sub>2</sub> phase with typically faceted (0001) planes [74].

## 2.3 TiB<sub>2</sub>/Al composites

### 2.3.1 Development history of TiB<sub>2</sub>/Al composites

TiB<sub>2</sub>/Al composite was first reported by Westwood in 1988 [71]. The TiB<sub>2</sub>/Al composite was proposed by the exothermic dispersion process (XD<sup>TM</sup>), with the moduli

turned out to be 40% higher than pure Al matrix [71]. The strength of the TiB<sub>2</sub>/Al composite retains at elevated temperatures, and the wear resistance as well as fatigue limit were also improved. Soon afterwards, the TiB<sub>2</sub>/Al composites were rapidly developed [28]. In the 1990s, a series of TiB<sub>2</sub>/Al composites with advanced mechanical properties (e.g., TiB<sub>2</sub>/Al composite, (Al<sub>2</sub>O<sub>3</sub>+TiB<sub>2</sub>)/Al composite and (Al<sub>2</sub>O<sub>3</sub>+ TiB<sub>2</sub>+ Al<sub>3</sub>Ti)/Al composite) were synthesized by varied preparation methods, such as solid-liquid reaction process, vapor-liquid-solid (VLS) reaction process and solid-solid reaction process [75-78]. Subsequently, the specific preparation technology for TiB<sub>2</sub> particles reinforced Al alloys matrix composites were further optimized by Wang et al. [42, 43, 79, 80]. A series of reliable and efficient TiB<sub>2</sub>/Al alloys-based composites, such as TiB<sub>2</sub>/Al-Mg-Si, TiB<sub>2</sub>/Al-Cu-Mg and TiB<sub>2</sub>/Al-Zn-Mg-Cu composites were prepared and applied in varied industry fields [42, 79-81].

### 2.3.2 Investigations on TiB<sub>2</sub>/Al interfaces

The TiB<sub>2</sub>/Al interface characteristics have been widely studied for they critically influence the mechanical properties of Al-based MMCs [75, 82, 83]. Ma *et al.* [75] conducted the studies on an *in-situ* formed Al<sub>2</sub>O<sub>3</sub>, TiB<sub>2</sub> and Al<sub>3</sub>Ti mixture-reinforced Al matrix composite, and proposed that the TiB<sub>2</sub>/Al interfaces are clean, and TiB<sub>2</sub> particles show no crystallographic OR with the Al matrix. On the contrary, Fan *et al.* [74] studied the TiB<sub>2</sub>/Al interface when they conducted the researches on the grain refining mechanism in the Al/Al-Ti-B system. They reported the formation of a Ti-rich monolayer on the (0001) TiB<sub>2</sub> surface, which was confirmed as a (112) Al<sub>3</sub>Ti two-dimensional compound (2DC). The OR between Al matrix, Al<sub>3</sub>Ti 2DC and TiB<sub>2</sub> is (0001)[11 $\bar{2}$ 0]<sub>TiB<sub>2</sub></sub>//(112)[ $\bar{2}$ 01] Al<sub>3</sub>Ti 2DC//((111)[0 $\bar{1}$ 1]Al. Schaffer *et al.* [84] carried out the crystallographic analysis of the ORs between Al matrix and TiB<sub>2</sub> particles by EBSD. The ORs between intra- and inter-granular TiB<sub>2</sub> and the Al matrix were determined by convergent beam Kikuchi pattern analysis. They proposed that when the ORs between the Al matrix and TiB<sub>2</sub> for the particles have their [0001]<sub>TiB<sub>2</sub></sub> direction within 10° of the [111]<sub>Al</sub> direction, the ORs are [11 $\bar{2}$ 0]<sub>TiB<sub>2</sub></sub>// ( $\bar{1}$ 10)<sub>Al</sub>, (0001)<sub>TiB<sub>2</sub></sub>//(111)<sub>Al</sub>; when the ORs

have their  $[0001]_{\text{TiB}_2}$  direction within  $10^\circ$  of the  $[001]_{\text{Al}}$  direction, the ORs are  $[2\bar{1}\bar{1}0]_{\text{TiB}_2} // (110)_{\text{Al}}$ ,  $(0001)_{\text{TiB}_2} // (001)_{\text{Al}}$ .

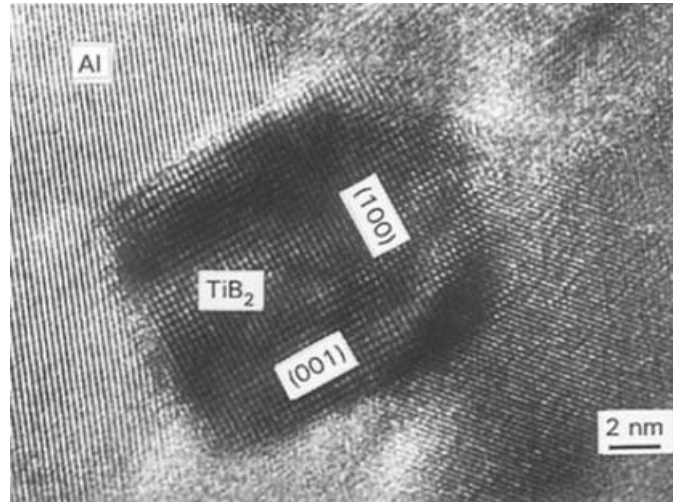


Fig. 2.5 HRTEM image of  $\text{TiB}_2$  nanoparticle and the surrounding Al matrix [75].

In addition, Mitra *et al.* [83] reported that nearly periodic misfit dislocations were observed at the semi-coherent  $\text{TiB}_2/\text{Al}$  interfaces through their study on a  $\text{TiB}_2/2024\text{Al}$  composite prepared by the XD<sup>TM</sup> technology. As is shown in Fig. 2.5, similar result also has been reported by Ma *et al.* [75]. Recently, however, Tang *et al.* [79] proposed that suggested by the absence of strain anisotropy in X-ray line profile analysis (XLPA), negligible dislocation density was found near the  $\text{TiB}_2/\text{Al}$  interface in a Al- $\text{TiB}_2$  composite. They also confirmed the  $\text{TiB}_2$  particles in the Al matrix obey the orientation relationships  $(0001)_{\text{TiB}_2} // (111)_{\text{Al}}$ ,  $[11\bar{2}0]_{\text{TiB}_2} // (\bar{1}10)_{\text{Al}}$ . Meanwhile, as is shown in Fig. 2.6, Li *et al.* [85] studied the  $\text{TiB}_2/\text{Al}$  interfaces in a  $\text{TiB}_2/\text{AlSi10Mg}$  composite fabricated by selective laser melting (SLM). They reported that Al matrix and  $\text{TiB}_2$  had a highly coherent interface for no misfit dislocations were observed. Besides, once again, they determined the existence of the well-reported OR  $[11\bar{2}0]_{\text{TiB}_2} // [110]_{\text{Al}}$ ,  $(0001)_{\text{TiB}_2} // (\bar{1}11)_{\text{Al}}$  and  $(\bar{1}10\bar{1})_{\text{TiB}_2} // (001)_{\text{Al}}$  between Al matrix and  $\text{TiB}_2$  particles.

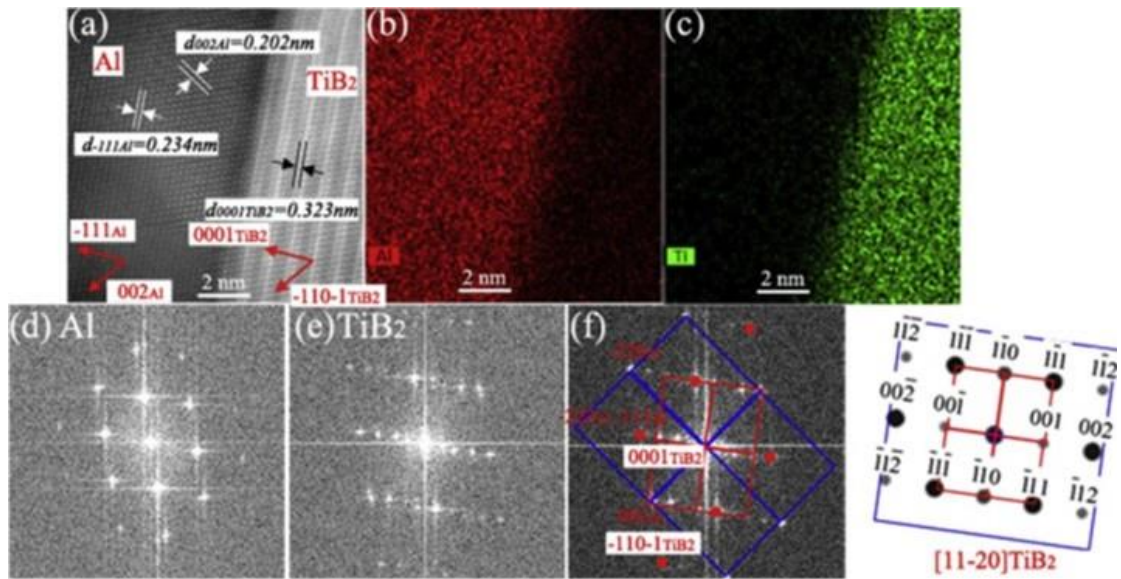


Fig. 2.6 HRSTEM high-angle annular dark-field (HRSTEM-HAADF) image showing the interface between Al matrix and TiB<sub>2</sub> nanoparticles and the STEM energy dispersive spectrometer (EDS) mapping of (b) Al and (c) Ti elements. Corresponding fast Fourier transform (FFT) patterns of (d) Al, (e) the TiB<sub>2</sub>/Al interface, (f) indexing of the FFT patterns in (e) compared to the simulated [11 $\bar{2}$ 0]<sub>TiB<sub>2</sub></sub>, giving the relative OR [85].

# Chapter 3 Methodology of Research

## 3.1 Material processing

Aiming to produce *in-situ* Al matrix composites, the London Scandinavian Metallurgical Company first developed the mixed-salt reaction cast method [28]. With an atomic ratio in accordance with Ti/2B, the mixed salts of  $K_2TiF_6$  and  $KBF_4$  are introduced into a stirred Al melt during the synthesis. The exothermal reactions between the introduced salts and the molten Al are as follows [28, 86]:

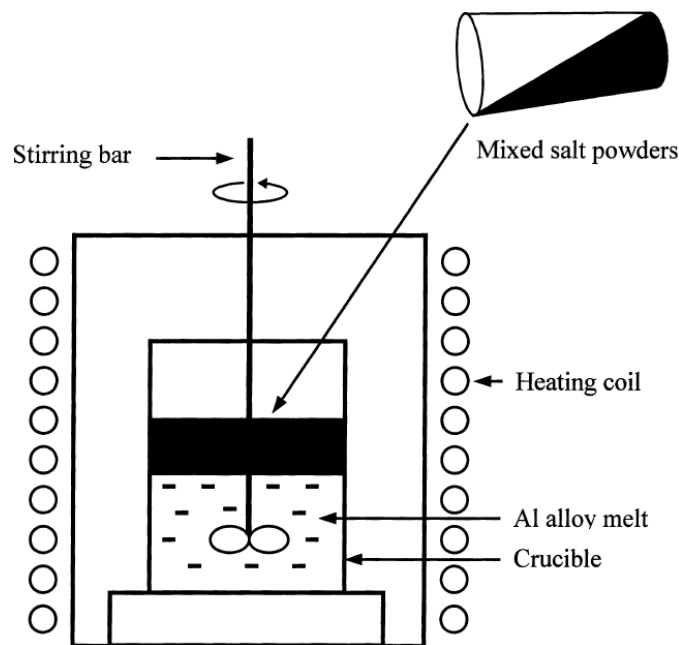


Fig. 3.1 Schematic diagram of an apparatus for fabricating *in-situ* MMCs via mixed-salt reaction cast [28].

The stirring is stopped when the reaction is finished to remove the slug containing  $KAlF_4$  and  $K_3AlF_6$ . Afterwards, the molten composite is cast into a mold. The viscosity

of the melt process controls the amount of *in-situ* formed  $\text{TiB}_2$ . The corresponding schematic diagram of an apparatus for fabricating *in-situ* MMCs via mixed-salt reaction cast is shown in Fig. 3.1 [28].

In this thesis, the  $\text{TiB}_2/\text{Al-Zn-Mg-Cu}$  nanocomposite sample was fabricated by the mixed-salt reaction cast method. First,  $\text{K}_2\text{TiF}_6$  and  $\text{KBF}_4$  reactive salts with high purity were mixed and added into molten Al metal in a high-purity graphite crucible heated at  $900\text{ }^\circ\text{C}$  in an electrical resistance furnace. The melt was mechanically stirred at 600 revolutions per minute (rpm) for 15 min and was casted in a permanent mold to acquire the pure Al composite reinforced with pre-synthesized master  $\text{TiB}_2$ . Mg, Zn and Al-Cu master alloy were added into the re-melted pre-synthesized master  $\text{TiB}_2/\text{Al}$  composite subsequently followed by a homogenization of 10 min. Following this, the Al-Zn-Mg-Cu alloy reinforced with 6 wt.%  $\text{TiB}_2$  particles was fabricated by direct chill casting. The chemical composition of the matrix was Al-6.5Zn-2.3Mg-2.3Cu.

Friction stir processing (FSP) is a method to modify the microstructure and mechanical properties of metal materials through the intense, localized plastic deformation produced by forcibly inserting a non-consumable tool into the workpiece, and revolving the tool in a stirring motion as it is pushed laterally through the workpiece [87, 88]. In FSP, a rotating tool is used with a pin and a shoulder to a single piece of material. Friction between the tool and workpieces results in localized heating that softens and plasticizes the workpiece [89]. A volume of processed material is produced by movement of materials from the front of the pin to the back of the pin. During this process, the material undergoes intense plastic deformation and this creates a microstructure with fine, equiaxed grains, leading to the improved tensile strength, ductility and fatigue property of the metal materials [90]. The corresponding schematic diagram of FSP is shown in Fig. 3.2 [91].

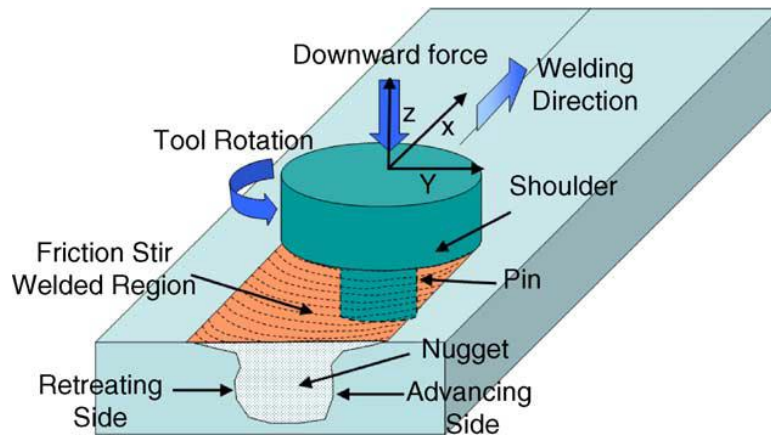


Fig. 3.2 Schematic drawing of FSP [91].

For the investigations on the interfacial precipitation and tensile properties of  $\text{TiB}_2/\text{Al-Zn-Mg-Cu}$  composite, plates with the dimension of  $200 \times 100 \times 16$  mm were cut from the cast ingot and annealed at  $470^\circ\text{C}$  for 24 h. An optimized (4-pass) FSP process was carried out on the plates with a tool rotation rate of 600 rpm, a tool tilt angle of  $2.5^\circ$ , a traverse speed of 80 mm/min and a processing depth of 8 mm. Hot extrusion ( $420^\circ\text{C}$ , extrusion ratio of 20:1) was carried out on the sample cut from the nugget zone after the homogenization at  $470^\circ\text{C}$  for 24 h. Finally, the as-extruded samples were subjected to T6 heat treatment ( $477^\circ\text{C}/70$  min + water quenching +  $120^\circ\text{C}/24\text{h}$ ) and T76 heat treatment ( $477^\circ\text{C}/70$  min + water quenching +  $120^\circ\text{C}/5\text{h}$  +  $160^\circ\text{C}/18\text{h}$ ), respectively. The quenched, peak-aged and overaged samples were used for detailed characterization.

Because the size of the nugget zone after FSP cannot meet the dimensional requirement of compact tension (CT) samples for FCG testing, FSP was not conducted on the samples used for the investigation on the FCG property of  $\text{TiB}_2/\text{Al-Zn-Mg-Cu}$  nanocomposite. The as-cast billets were annealed at  $470^\circ\text{C}$  for 24 h, then directly extruded at  $420^\circ\text{C}$  with the extrusion ratio of 10:1. Afterwards, the samples were subjected to T6 heat treatment ( $477^\circ\text{C}/70$  min + water quenching +  $120^\circ\text{C}/24\text{h}$ ).

### 3.2 Sample preparation

### **3.2.1 SEM and EBSD sample preparation**

Samples were cut from the center of extrusion rod along and normal to extrusion direction (ED). Then, the samples were mechanically milled by using silicon carbide papers of 400, 800, 1200 and 2400 grits successively. Subsequently, the samples were polished on a polishing disk by using diamond abrasive paste of 3, 1 and 1/4  $\mu\text{m}$  for 5, 4 and 2 minutes, respectively. DP-Lubricant Red was used during the polishing. The polished samples were ultrasonically cleaned in ethanol so as to remove the residual polishing agents. After mechanical polishing, the samples were subjected to ion polishing for 15 minutes. The voltage was 5 kV, the contact angle of the ion beams was  $5^\circ$  and the samples rotated at 7 rpm. Afterwards, the ion polished samples were applied for SEM and EBSD characterization.

### **3.2.2 STEM sample preparation**

Samples were cut from the center of the extrusion rod along ED. Subsequently, the samples were subjected to mechanical milling by using silicon carbide papers of 800, 1200 and 2400 grits successively. When the thickness of the samples was milled to  $\sim 80\mu\text{m}$ , they were polished on a polishing disk by using diamond abrasive paste of 3, 1 and 1/4  $\mu\text{m}$  for 3, 2 and 1 minutes, respectively. DP-Lubricant Red was used during the polishing. To remove the residual polishing agents, the polished samples were ultrasonically cleaned in acetone. Afterwards, small disks with a diameter of 3 mm were punched from the thin film and subjected to final ion milling by a GATAN precision ion polishing system, operated at  $-150^\circ\text{C}$  using liquid nitrogen. The voltage was set as 5 kV, the contact angles of the ion beams were  $\pm 10^\circ$  and the rotation speed of the sample was 1.5 rpm.

### **3.2.3 Tensile and FCG tests sample preparation**

For the tensile testing, the dog-bone specimens were machined along ED with gauge length of  $2\text{ mm} \times 3\text{ mm} \times 10\text{ mm}$ .

For the FCG testing, the extruded rods were cut by linear cutting to obtain plates, as is shown by the schematic diagram in Fig. 3.3a. Those plates were then machined into CT specimens for FCG testing according to the ASTM E647-2013a standard with a size of 45×43.2×6 (mm) [92]. The detailed dimensions of the specimens are shown in Fig. 3.3b. After the mechanical processing, all of the specimens were subjected to mechanical polishing to minimize the effect of machining defects, such as surface damage or subsurface alternation. The notch and the pre-crack (~2 mm in length) were perpendicular to ED.

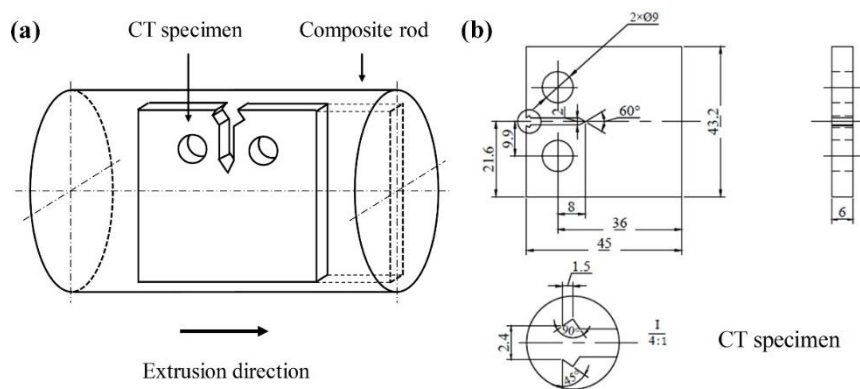


Fig. 3.3 (a) Schematic diagram and (b) dimensions of the CT specimens for the FCG rate testing.

### 3.3 Experimental methods

#### 3.3.1 SEM and EBSD

Scanning electron microscopy (SEM) acquires the image of the sample by scanning the surface with a focused beam of electrons. The interaction between the atoms of the sample and the electron results in the production of various signals that contain the composition or surface topography of the sample. Scanning with a raster scan pattern, the intensity of the detected signal is combined with the position of the beam [93].

Electron backscatter diffraction (EBSD) is conducted on the SEM equipped with an EBSD detector. Microstructure, microtexture, grain morphology and phase of the crystalline materials can be characterized by this technique [94]. The sample is placed

with at a tilted angle  $70^\circ$  away from the horizontal in order to improve the contrast of EBSD pattern. When the electron beam is focused on the sample, some electrons will backscatter near to the Bragg angle and diffract to generate Kikuchi bands. The Kikuchi bands are corresponding to the diffraction lattice plane, which can be indexed by the Miller indices. The crystal orientation also can be revealed from the diffraction pattern. Generally, EBSD is used to simultaneously characterize the phase and microstructure of a selected region of the sample.

In this thesis, the microstructural and fatigue fracture morphology of the  $\text{TiB}_2/\text{Al-Zn-Mg-Cu}$  nanocomposite were observed by SEM (JSM-7800F) equipped with EDS. The EBSD was conducted on NOVA NanoSEM 230 with the step size of 0.1 and 0.2  $\mu\text{m}$  depending on the grain size. The obtained micrographs were analyzed using the Channel 5 software to achieve the grain size distributions and average grain sizes.

### **3.3.2 STEM**

Scanning transmission electron microscopy (STEM) can simultaneously acquire the atomic-scale crystal information and elemental composition of material, thus it is very appropriate for nanostructure characterization. Being analogous to SEM, the STEM works by scanning the TEM sample with a focused electron beam. After the interaction with sample, the transmission beam is collected by a CCD chip (TEM mode) or HAADF detector. In TEM mode, due to more scattering of the electrons, the dense zone or zone contains heavy elements are dark. In STEM mode, the sensitivity of the HAADF detector to differences of the element irradiated based on the atomic number (Z-contrast) lead to the opposite situation [95]. The schematic diagrams of the illumination part in STEM is shown in Fig. 3.4. The STEM imaging can be used in combination with other useful analysis techniques such as EDS, energy filtered TEM (EFTEM) and electron energy loss spectroscopy (EELS) [96].





Fig. 3.5 MTS 809 servohydraulic testing machine system

The FCG testing was conducted on the MTS 809 servohydraulic testing machine at room temperature and laboratory air environment (Fig. 3.5). A sinusoidal cyclic constant loading with a stress ratio ( $R=\sigma_{\min}/\sigma_{\max}$ ) of 0.1 and a frequency of 10 Hz were applied. The MTS computer system was employed to control and detect the FCG rates during the FCG testing. The crack growth was measured by the crack tip open displacement (CTOD) method on the MTS 809 servo hydraulic testing machine. According to ASTM E647-13a [92], the test specimens were tested at a constant force ( $P$ ) range. So, as the crack length increasing,  $K$  was increasing during the test procedure. For the C(T) specimen,  $\Delta K$  is calculated as follows:

$$\Delta K = \frac{\Delta P}{B\sqrt{W}} \frac{2 + \alpha}{(1 - \alpha)^{\frac{3}{2}}} (0.886 + 4.64\alpha - 13.32\alpha^2 + 14.72\alpha^3 - 5.6\alpha^4)$$

where  $\alpha = a/W$ ,  $\Delta P = P_{\max} - P_{\min}$ ,  $a$  is the crack length,  $B$  and  $W$  are the dimensions of specimens.

# Chapter 4 Atomic-scale Investigation of the Interface Precipitation in a TiB<sub>2</sub> Nanoparticles Reinforced Al-Zn-Mg-Cu Matrix Composite

*In preparation for submission. Y. Ma, A. Addad, G. Ji, M. Zhang, W. Lefebvre, Z. Chen, V. Ji*

The effects of nanosized reinforcement particles on precipitation reactions in age-hardenable Al alloy matrix composites have been largely unknown. In this work, an Al-Zn-Mg-Cu matrix composite reinforced with uniformly distributed TiB<sub>2</sub> nanoparticles was successfully produced. The solid-soluted, peak-aged and overaged materials were then characterized, at the atomic scale using (high-resolution) scanning transmission electron microscopy, to provide a fundamental insight into the interface precipitation. Our results demonstrated that the faceted TiB<sub>2</sub> nanoparticles have a significant impact on the precipitation in matrix adjacent to the TiB<sub>2</sub>/Al interfaces. The interfaces after solid-solution treatment are tightly-bonded and oxide-free, and display two orientation relationships (ORs): the well-reported  $[2\bar{1}\bar{1}0]_{\text{TiB}_2} // [101]_{\text{Al}}$ ,  $(0001)_{\text{TiB}_2} // (\bar{1}11)_{\text{Al}}$  (OR1) and the new  $[2\bar{1}\bar{1}0]_{\text{TiB}_2} // [101]_{\text{Al}}$ ,  $(01\bar{1}0)_{\text{TiB}_2} // (11\bar{1})_{\text{Al}}$  (OR2). The interface precipitates (i.e. interphase) having the size of several tens of nanometers were formed after ageing and were determined to be  $(\text{Zn}_{1.5}\text{Cu}_{0.5})\text{Mg}$  phase. Their formations were only related to the initial OR1 and OR2 where the mutual ORs between the TiB<sub>2</sub>, interphase and Al matrix were further developed. Periodically spaced misfit dislocations were revealed at the semi-coherent TiB<sub>2</sub>/Al interfaces, which are generally considered beneficial to the heterogeneous precipitation. They not only reduced nucleation energy barrier, but also acted as short-circuit diffusion paths for transporting solute atoms and vacancies, accelerating growth rate. However, the growth of interphase at the interface parallel to

close-packed {111} Al planes was suppressed by the ultra-low accommodation factor. In addition, such an interface precipitation reduced the mismatch of the TiB<sub>2</sub>/Al interface, increasing the overall coherency and being potential for effective interface strengthening.

## 4.1 Introduction

Age-hardenable Al alloys (e.g., 2xxx, 6xxx and 7xxx series) have been widely applied as structural materials in aerospace and automobile industries, due mainly to their high specific strength and excellent processability [1-3]. Commonly, one of the most effective strengthening mechanisms involves precipitation hardening, i.e., a homogenous distribution of nanosized precipitates originating from solid-state precipitation reactions during aging treatments [4-6]. In addition, micron- (or submicron-) sized reinforcement particles (MRPs), such as SiC and B<sub>4</sub>C, have successfully been introduced to Al alloys, providing an alternative approach to further enhance their mechanical performance, particularly in case high Young's modulus is necessary [7-9]. It has been largely recognized that MRP/Al interface structure critically influences the precipitation reactions to promote the formations of coarse precipitate zone (CPZ) and precipitate free zone (PFZ) in the surrounding matrix [12-22]. This, in turn, has a significant impact on overall mechanical properties of the Al-based metal matrix composites (MMCs) [33-35].

It has been well established that the CPZ is caused by thermoelastic stress induced dislocations (TSIDs) near the MRP/Al interface [12-15]. The interaction between solute atoms and TSIDs leads to a solute flux towards dislocations resulting in faster and coarser precipitation on them [13-15]. When it comes to the PFZ formation, particularly in Al-Zn-Mg(-Cu) matrix composites, the underlying mechanism remains controversial. Some researchers have claimed that the PFZ formation is related to vacancy depletion [16-18]. As proposed, precipitation reactions at the MRP/Al interface are analogous to those at high-angle grain boundaries (GBs) in (unreinforced) Al alloys. The weakly-

bonded and incoherent MRP/Al interface as well as TSIDs can act as ideal sinks to absorb and cause the annihilation of vacancies during the solution treatment [16-18]. Considering the nucleation of *Guinier-Preston* (GP) zones in Al alloys requiring a critical vacancy concentration [64, 65], the precipitation process in the vicinity of MRPs is thereby hindered leading to the PFZ formation. On the contrary, some studies revealed that the number of quenched-in vacancies has no influence on the GP zone formation in Al-Zn-Mg(-Cu) alloys [97, 98]. It was thus indicated that the PFZ formation is likely attributed to the solute atoms rather than vacancy depletion [19-21]. For example, Hong *et al.* [19] observed the formation of numerous MgO particles with the size of tens of nanometers at the SiC/Al interface in the Al-Zn-Mg-Cu matrix composite reinforced with 20 vol.% SiC particles. They proposed that this results in the depletion of Mg atoms in the surrounding matrix and then the suppression of precipitation in the vicinity of SiC particles during the aging process [19].

In addition to the two well-documented CPZ and PFZ mentioned above, Strangwood *et al.* [22] reported that the MRP/Al interface can play the role as an ideal nucleation substrate to promote interracial segregation and precipitation on it in the SiC particles reinforced 2xxx and 7xxx matrix composites. They also found that the heterogeneous interfacial precipitations have a close correlation with the aging conditions [22]. In the case of 7xxx matrix composite, it was found that, in the underaged composite, the SiC/Al interface was covered by a continuous precipitate layer which extended the thickness of around 10-20 nm into the Al matrix. Within the precipitate layer, discrete  $\eta$  particles ( $\text{MgZn}_2$ ) with 24-40 nm in diameter and spaced at approximately 70-80 nm intervals were discerned. However, in the overaged composite, the diffuse interfacial  $\eta'/\eta$  layer dissolved, giving rise to a series of fairly regularly (45-70 nm) spaced T phase ( $\text{Mg}_{32}(\text{Al}, \text{Zn})_{49}$ ) with size of ranging from 20 to 30 nm in diameter surrounding the interface.

In parallel with the developments in nanotechnology, the dimensions of reinforcement particles (RPs) have decreased from micron/submicron scale to nanoscale ( $\leq 100$  nm) over the last decades [28, 29]. Accordingly, volume fraction of

the particle/matrix interfaces increases proportionally as:  $V_2 = (r_1/r_2)^3 V_1$ , where  $r_1$  and  $r_2$  are the radius of spherical reinforcements,  $V_1$  and  $V_2$  are corresponding interface volumes of the spherical reinforcements [39]. Thus, it is expected that structure evolution of nanosized reinforcement particle (NRP)/Al interfaces during the aging treatments can play a more important and critical role in influencing mechanical properties of the Al-based MMCs. Furthermore, considering interfacial structure of the NRP/Al interface being very different compared with that of the MRP/Al one, one realized that the presence of NRPs should have a disparate influence on the precipitation reactions in the Al alloy matrix. But, up to now no experimental evidences, at the nano- and atomic scales, have been properly disclosed, which constitutes one of the most important fundamental problems still unclear in the NRPs reinforced Al-based MMCs.

In spite of this, some hypotheses based on the pioneer works can be proposed. Firstly, Kim *et al.* [30] proposed that the intensity of TSIDs shows a strong particle size dependence. It increases significantly only when the size of RPs reaches the micron level. At the finer scales the thermoelastic stress can be lower than the effective yield stress such that no TSIDs and no CPZ (caused by TSIDs) in the surrounding matrix should be generated [31, 32]. Secondly, in contrast to the incoherent MRP/Al interface [36, 99], semi-coherent NRP/Al interface is more analogous to low-angle GBs, becoming inefficient vacancy sinks [83, 100-102]. The NRP/Al interface is thus incapable to lead to vacancy depletion in the surrounding matrix. It was also reported that no oxide particles or amorphous layers have been found at the NRP/Al interface, suggesting no solute depletion caused by interfacial oxide formation [79, 81, 85]. Consequently, no PFZ shall generate in NRPs reinforced Al-based MMCs whatever its formation mechanisms due to vacancy or solute depletion. Thirdly, unlike the MRP/Al interface, it has been well established that NRPs generally have preferential crystallographic orientation relationships (ORs) with the Al alloy matrix [28, 36]. As such, it is of theoretical possibility to have ORs in between the NRPs, interfacial precipitates and Al alloy matrix in order to minimize the nucleation energy barrier [37, 38]. Finally, considering the NRP/Al interfacial precipitation reactions being analogous

to those at low-angle GBs, the transformation of precipitates from  $\eta$  to T phases observed at the SiC/Al interface (being analogous to high-angle GBs) during the ageing treatments [22], can most probably occur in a different way in NRPs reinforced 7xxx matrix composites [65, 102].

In view of the discussions above, the present work aims to provide a fundamental insight into the influences of NRPs on the precipitation reactions in Al-based MMCs. With high melting point (3173 K), high modulus (565 GPa), high hardness (2500 HV) and good thermal stability [40], TiB<sub>2</sub> nanoparticles have widely been used as one of the most ideal NRPs in Al-based MMCs [41-43]. In this work, an Al-Zn-Mg-Cu matrix composite reinforced with homogeneously distributed TiB<sub>2</sub> nanoparticles was successfully fabricated and heat treated at different conditions, including solid-solution, peak-ageing and over-ageing treatments, followed by comprehensive characterization. Probe-corrected (high-resolution) scanning transmission electron microscopy ((HR)STEM), in particular, high-angle annular dark-field (HAADF) imaging associated with energy dispersive spectrometer (EDS) mapping was used, which provides access to the nature of the precipitation reactions with spatial resolution at the nano- and atomic scales. We found significant microstructural evolutions at the TiB<sub>2</sub>/Al interface during the aging treatments. The interface was initially clean after solid-solution treatment. Heterogeneous interfacial precipitates (hereafter referred to as interphase, abbr. IP), determined to be (Zn<sub>1.5</sub>Cu<sub>0.5</sub>)Mg phase, were only formed at the preferential TiB<sub>2</sub>/Al interfaces during ageing. The crystallographic ORs between the TiB<sub>2</sub> nanoparticle, interphase and Al matrix were determined. The atomic structure of the Al/interphase/TiB<sub>2</sub> multi-interfaces was systematically characterized and analyzed. Based on these experimental evidences, the kinetics of the TiB<sub>2</sub> nanoparticles exerted to the interface precipitation, including nucleation, growth rate, preferential precipitation TiB<sub>2</sub>/Al interfaces, effects of aging conditions are discussed in detail.

## 4.2 Experimental procedure

#### 4.2.1 Materials processing

An *in-situ* mixed salt method was used to produce the TiB<sub>2</sub> nanoparticles (6 wt.%) reinforced Al-Zn-Mg-Cu composite ingot using high-purity reactive salts of K<sub>2</sub>TiF<sub>6</sub> and KBF<sub>4</sub> [42]. Composite melts were synthesized at 900 °C in an electrical resistance furnace, and then cast into a graphite mould. 200 × 100 × 16 mm plates were then cut from the equal-axis grain zones of the ingot and homogenized at 465 °C for 24 h. Subsequently, a 4-pass friction stir processing (FSP) process was carried out with a tool rotation rate of 600 rpm, a tool tilt angle of 2.5°, a traverse speed of 80 mm/min and a processing depth of 8 mm [103]. Afterwards, hot extrusion with an extrusion ratio of 20:1 was carried out on the samples cut from the nugget zone. Finally, the as-extruded samples were subjected to T6 (470 °C/70 min + water quenching + 120°C/20h) and T76 (470 °C/70 min + water quenching + 120°C/5h + 160°C/18h) heat treatments. The as-quenched and both aged samples were characterized in more details using STEM.

#### 4.2.2 Microstructure characterization

STEM specimens with 3 mm in diameter were prepared through mechanical polishing and final ion milling in a GATAN precision ion polishing system, operated at - 150 °C. A state-of-the-art FEI Titan Themis 300 microscope equipped with a probe aberration corrector, operated at 200 kV, was used to acquire (HR)STEM images. The probe size was set to 0.1 nm with a convergence semi-angle of 22.5 mrad. Collection angle of the HAADF detector was in the range 80-150 mrad. Contrasts in an HAADF image is proportional to  $Z^{1.7-2}$ , meaning that the bright contrast indicates relatively heavy atomic composition [95]. In this case, the bright and dark contrasts can be considered as Zn (Cu)-rich and Mg-rich areas in the Al matrix, respectively. The equipped highly efficient (4 quadrant) EDS system was used for chemical analyses of possible precipitates formed at the TiB<sub>2</sub>/Al interface. Interface characterization was done by tilting the Al matrix to the [101] orientation in terms of the well-documented preferential ORs of the TiB<sub>2</sub>/Al interfaces [84]. JEMS software was used for generating

theoretical electron diffraction patterns by considering the kinematic approximation [104]. Dr. Probe software was used for simulating atomic-scale HRSTEM-HAADF images [105]. VESTA, a 3-D visualization program for structural models, was used to construct interfacial atomic structure configurations [106].

## 4.3 Results

### 4.3.1 The TiB<sub>2</sub>/Al interface structure in the solid-solution treated composite

Our previous studies of the TiB<sub>2</sub>/Al-Mg-Si [107] and TiB<sub>2</sub>/Al-Zn-Mg-Cu composites [103] demonstrated that the fabrication process combining casting (*in-situ* reaction), FSP and extrusion is efficient to acquire a desired microstructure in the nugget zone. It is featured with a fine equiaxed grain structure (a few micrometers in the average size) and uniformly distributed TiB<sub>2</sub> nanoparticles.

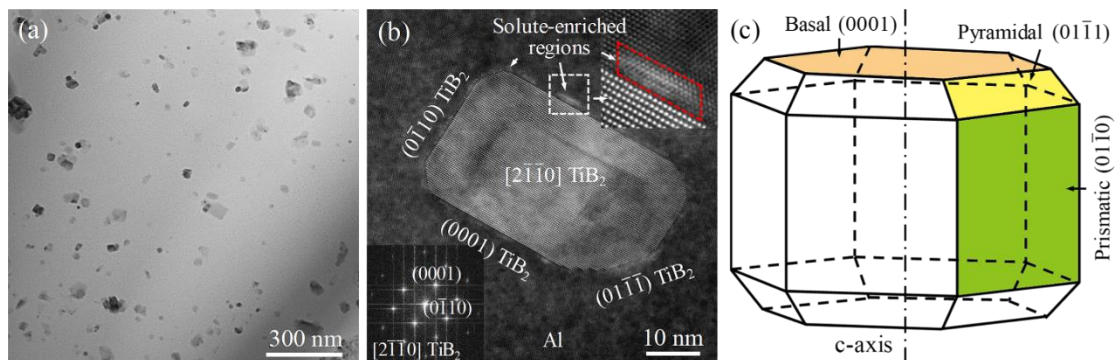


Fig. 4.1 (a) Bright-field TEM image showing homogenous distribution of TiB<sub>2</sub> nanoparticles in the Al-Zn-Mg-Cu matrix grain at the as-quenched state, (b) STEM-HAADF image showing a typical TiB<sub>2</sub>/Al interface and (c) schematic drawing illustrating the faceted shape of the TiB<sub>2</sub> nanoparticle. Insets in (b) at the left bottom and top right sides highlight corresponding FFT pattern of the TiB<sub>2</sub> nanoparticle and solute-enriched regions, respectively.

Fig. 4.1a shows the uniform distribution of the majority TiB<sub>2</sub> nanoparticles within an Al grain. Fig. 4.1b shows a typical TiB<sub>2</sub> nanoparticle that has faceted shape with identified basal {0001}, prismatic {0110} and pyramidal {0111} facets, which is

illustrated in Fig. 4.1c. This is consistent with previous results [108, 109]. The TiB<sub>2</sub>/Al interface is tightly bonded and free of oxide particles, where solute-enriched zones having a size of several nanometers are present.

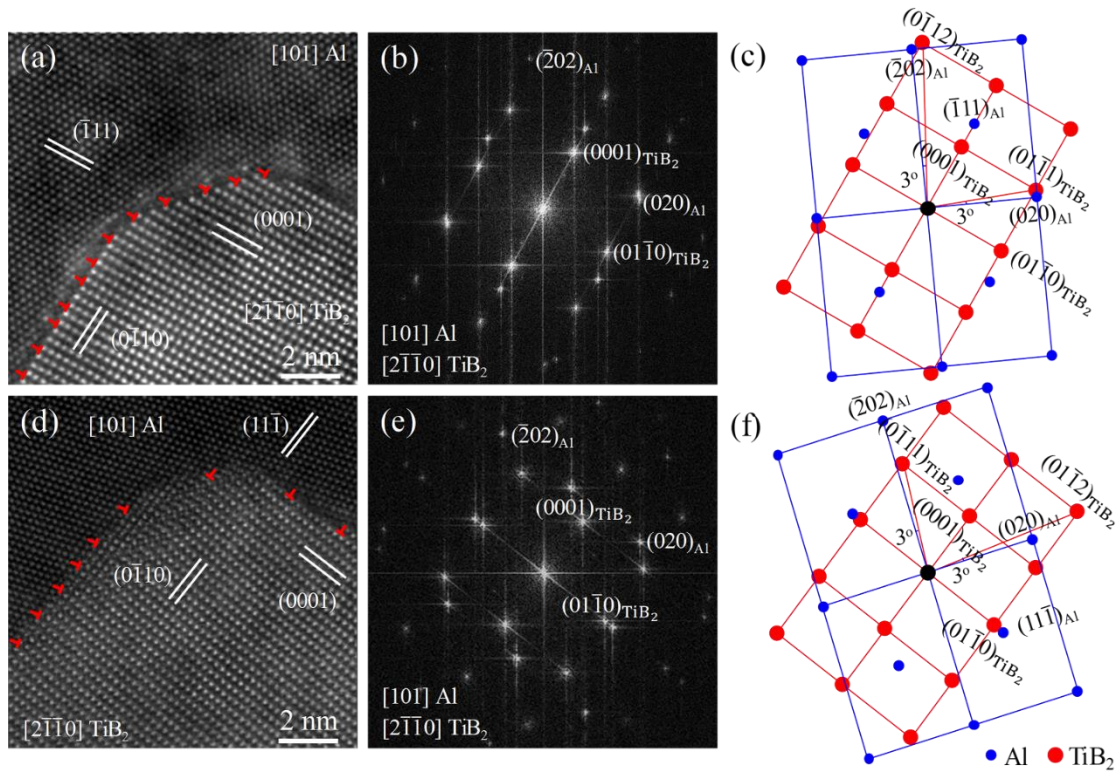


Fig. 4.2 (a) and (d) HRSTEM-HAADF images showing TiB<sub>2</sub>/Al interface structures at the OR1 and OR2 conditions, respectively, (b) and (e) corresponding FFT patterns of (a) and (d), and (c) and (f) corresponding simulated diffraction patterns for indexing, respectively. The projection direction is  $[2\bar{1}\bar{1}0]_{\text{TiB}_2} // [101]_{\text{Al}}$ . See the text for more details.

Fig. 4.2 presents two typical HRSTEM images and the associated fast Fourier transform (FFT) patterns, showing two ORs between the TiB<sub>2</sub> nanoparticle and the Al matrix, namely OR1 (Figs. 4.2a-c) and OR2 (Figs. 4.2d-f). The OR1 is consistent with previous result reported in Refs. [84, 110]. But, the OR2 is new. From Figs. 4.2a and 4.2d one can also observe the periodically-spaced misfit dislocations next to the TiB<sub>2</sub>/Al interface for both ORs, which are highlighted in red.

OR1:  $[2\bar{1}\bar{1}0]_{\text{TiB}_2} // [101]_{\text{Al}}$ ,  $(0001)_{\text{TiB}_2} // (\bar{1}11)_{\text{Al}}$ ,

$(01\bar{1}1)_{\text{TiB}_2}$   $3^\circ$  from  $(020)_{\text{Al}}$ ,  $(0\bar{1}12)_{\text{TiB}_2}$   $3^\circ$  from  $(\bar{2}02)_{\text{Al}}$

OR2:  $[2\bar{1}\bar{1}0]_{\text{TiB}_2} // [101]_{\text{Al}}$ ,  $(01\bar{1}0)_{\text{TiB}_2} // (11\bar{1})_{\text{Al}}$ ,

$(0\bar{1}12)_{\text{TiB}_2}$   $3^\circ$  from  $(020)_{\text{Al}}$ ,  $(01\bar{1}1)_{\text{TiB}_2}$   $3^\circ$  from  $(\bar{2}02)_{\text{Al}}$

#### 4.3.2 The $\text{TiB}_2/\text{Al}$ interface structures in the peak-aged and over-aged composites

After peak ageing, interphase precipitates can be observed in between the  $\text{TiB}_2$  nanoparticle and the Al matrix as shown in Figs. 4.3a-d. But no discernible CPZ or PFZ were found in the vicinity of  $\text{TiB}_2$  nanoparticle. The interphases formed on preferential facets of the  $\text{TiB}_2$  nanoparticle with a specific contact angle of around  $60^\circ$ . In addition to such interphase precipitates, finer precipitates with a high density can also be seen being homogeneously distributed in the Al matrix away from  $\text{TiB}_2$  nanoparticles, as shown in Fig. 4.3b. These finer precipitates are the plate-like GP zones with the diameter of  $\sim 8$  nm (Fig. 4.3c) and rectangle  $\eta'$  phase on the  $\{111\}_{\text{Al}}$  planes, which is roughly 2 nm in thickness and 8 nm in length (Fig. 4.3d). Both GP zones and  $\eta'$  phase are fully coherent with the Al matrix.

Similar to the peak-aged sample, neither obvious CPZ nor PFZ were observed in the over-aged sample, but interphase precipitates formed at the  $\text{TiB}_2/\text{Al}$  interface with a contact angle of around  $60^\circ$ , as shown in Fig. 4.3e. In addition, dense rectangle  $\eta$  (type  $\text{MgZn}_2$  [59]) precipitates on  $\{111\}_{\text{Al}}$  planes are found being uniformly distributed in the matrix (Fig. 4.3f). They are about 7 nm thick and 26 nm long (Fig. 4.3g). This  $\eta$  phase is semi-coherent with the Al matrix due to the misfit dislocations at the Al/ $\eta$  interface (Fig. 4.3h).

Results in Figs. 4.2 and 4.3 indicate that the  $\text{TiB}_2/\text{Al}$  interfaces were preferred sites for promoting the precipitation reactions. While, within the Al matrix away from the interface, the observed precipitation sequence was supersaturated solid solution  $\rightarrow$  GP zones  $\rightarrow$  metastable  $\eta'$   $\rightarrow$  stable  $\eta$ . This agrees with the results well-documented in the Al-Zn-Mg-Cu alloy [53]

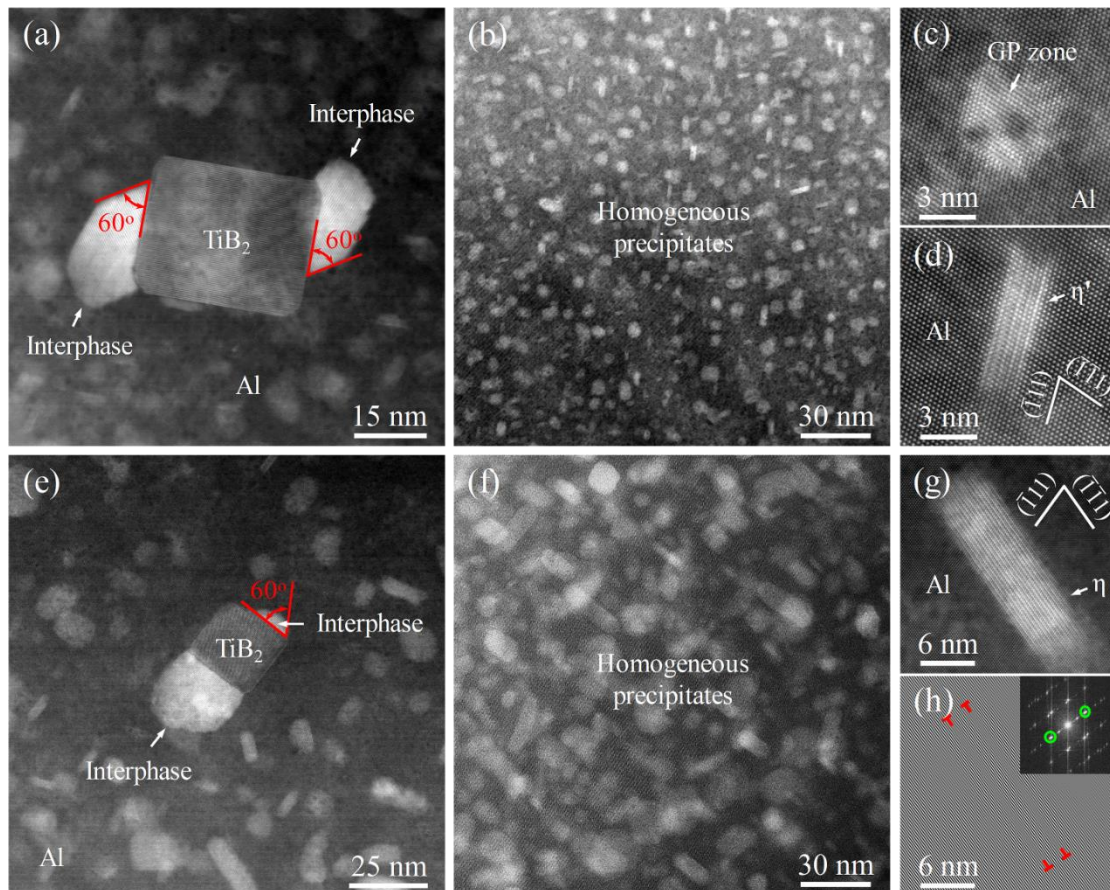


Fig. 4.3 (a) and (b) STEM-HAADF images showing heterogeneous precipitates at the  $\text{TiB}_2/\text{Al}$  interfaces and finer precipitates in the matrix away from the interface at the peak-aged state, respectively. HRSTEM-HAADF images highlighting (c) plate-like GP zone and (d) elongated  $\eta'$  phase in (b); (e) and (f) STEM-HAADF image showing the heterogeneous precipitates at the  $\text{TiB}_2/\text{Al}$  interfaces and finer precipitates in the matrix away from the interface at the overaged state, respectively. (g) HRSTEM-HAADF image highlighting lath-like  $\eta$  phase in (f) and (h) corresponding inverse FFT pattern of (g) showing misfit dislocations at the  $\text{Al}/\eta$  interfaces. Inset in (h) shows the corresponding FFT pattern of (g). The projection direction is  $[101]_{\text{Al}}$ .

#### 4.3.2.1 Structure determination of the formed interphase precipitate

Using STEM/EDS elemental mapping, it was identified that the interphase precipitates in both the peak-aged and over-aged samples were enriched with Zn, Mg, Cu and Al as exemplified in Fig. 4.4. However, it was hard to figure out if Al is the

constituent element considering possible overlapping with the Al matrix. To solve this problem, semi-quantitative EDS data were randomly acquired from different areas containing the interphase, and the results are listed in Table 4.1. Despite the variations of Al content, the elemental content ratio of Zn, Mg and Cu remains constant and presents a specific value approximately 3:2:1. This indicates the absence of Al and suggests that the interphase precipitate is possibly the  $(\text{Zn}_{1.5}\text{Cu}_{0.5})\text{Mg}$  phase (Hexagonal,  $a=5.124 \text{ \AA}$ ,  $c=16.820 \text{ \AA}$ ,  $P63/mmc$ , No. 194) [111]. From a HAADF image as shown in Fig. 4.5 the interplanar spacing of the (0004) and  $(\bar{1}\bar{1}20)$  planes were measured to be 0.421 nm and 0.256 nm, respectively, which accords with that of the  $(\text{Zn}_{1.5}\text{Cu}_{0.5})\text{Mg}$  phase. The corresponding FFT pattern of the  $(\text{Zn}_{1.5}\text{Cu}_{0.5})\text{Mg}$  phase matches the structure of this phase well [111]. Furthermore, the simulated HAADF image of  $(\text{Zn}_{1.5}\text{Cu}_{0.5})\text{Mg}$  phase (overlapped in Fig. 4.5a) fits with the intensity of the experimental result of the interphase. Thus, the interphase is identified to be the  $(\text{Zn}_{1.5}\text{Cu}_{0.5})\text{Mg}$  phase. Note that this method was also used to identify the interphase precipitates formed in the overaged sample, confirming the same crystal structure of the phase.

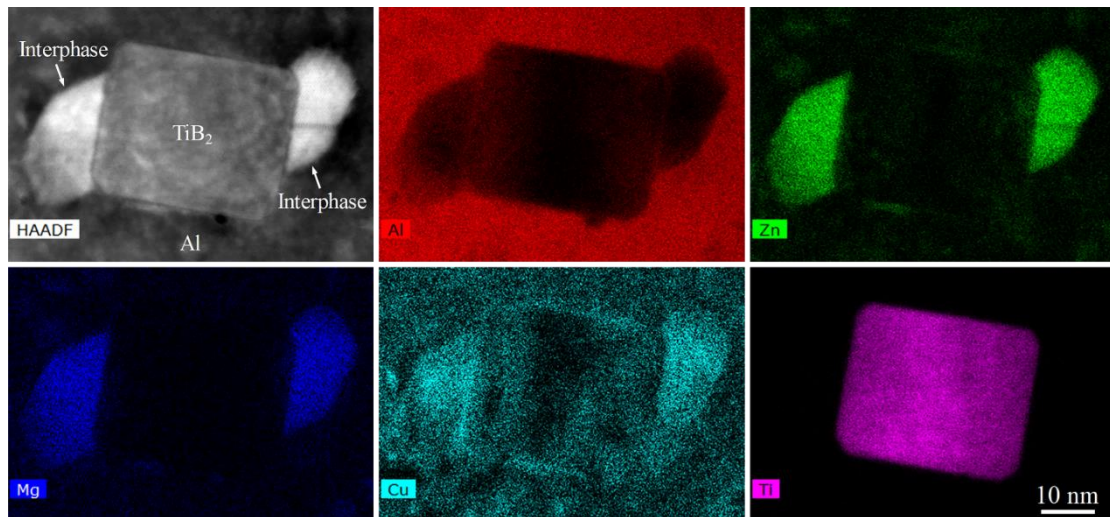


Fig. 4.4 STEM-HAADF image of the Al/interphase/TiB<sub>2</sub> interfaces and corresponding Al, Zn, Mg, Cu and Ti elemental EDS maps.

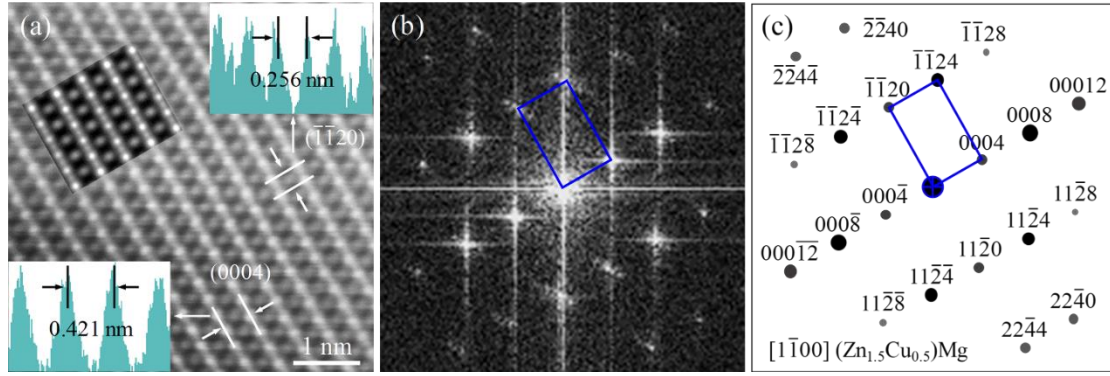


Fig. 4.5 (a) HRSTEM-HAADF image showing atomic structure of the interphase, (b) and (c) corresponding FFT and simulated diffraction patterns, respectively. Insets in (a) are the simulated HRSTEM-HAADF image of  $[1\bar{1}00]$   $(\text{Zn}_{1.5}\text{Cu}_{0.5})\text{Mg}$  phase overlapped and intensity profiles used for measuring interplanar spacing.

Table 4.1 Elemental content ratio of Al, Zn, Mg and Cu recorded from the four interphases acquired by STEM/EDS mapping.

| Interphase number | Atomic composition (at. %) |       |       |       |
|-------------------|----------------------------|-------|-------|-------|
|                   | Al                         | Zn    | Mg    | Cu    |
| 1                 | 46.16                      | 25.30 | 18.29 | 10.26 |
| 2                 | 59.72                      | 19.63 | 12.80 | 7.85  |
| 3                 | 63.32                      | 18.71 | 11.64 | 6.33  |
| 4                 | 69.51                      | 15.28 | 9.91  | 5.31  |

#### 4.3.2.2 OR-dependent precipitations at the $\text{TiB}_2/\text{Al}$ interfaces

As shown in Fig. 4.6, the prismatic  $\{01\bar{1}0\}$  and pyramidal  $\{01\bar{1}1\}$  facets of the  $\text{TiB}_2$  nanoparticles are the preferential heterogeneous precipitation sites at the OR1 condition (Figs. 4.6a-6c), while the two basal  $\{0001\}$  facets are the sites at the OR2 (Figs. 4.6d-6f). Figs. 4.7 and 4.8 show the ORs between the interphase precipitates, the  $\text{TiB}_2$  nanoparticle and the Al matrix. At the peak-aged/OR1 condition (Fig. 4.7), the reproducible ORs, namely the OR3 between interphase and Al matrix and the OR4 between interphase and  $\text{TiB}_2$  were determined. They are:

The OR3:  $[1\bar{1}00]_{\text{IP}}//[101]_{\text{Al}}$ ,  $(11\bar{2}4)_{\text{IP}}//(11\bar{1})_{\text{Al}}$ ,  
 $(\bar{1}\bar{1}20)_{\text{IP}}$   $3^\circ$  from  $(\bar{2}02)_{\text{Al}}$ ,  $(0008)_{\text{IP}}$   $3^\circ$  from  $(020)_{\text{Al}}$

The OR4:  $[2\bar{1}\bar{1}0]_{\text{TiB}_2} // [1\bar{1}00]_{\text{IP}}$ ,  $(01\bar{1}1)_{\text{TiB}_2} // (0008)_{\text{IP}}$ ,  $(01\bar{1}0)_{\text{TiB}_2} // (11\bar{2}8)_{\text{IP}}$

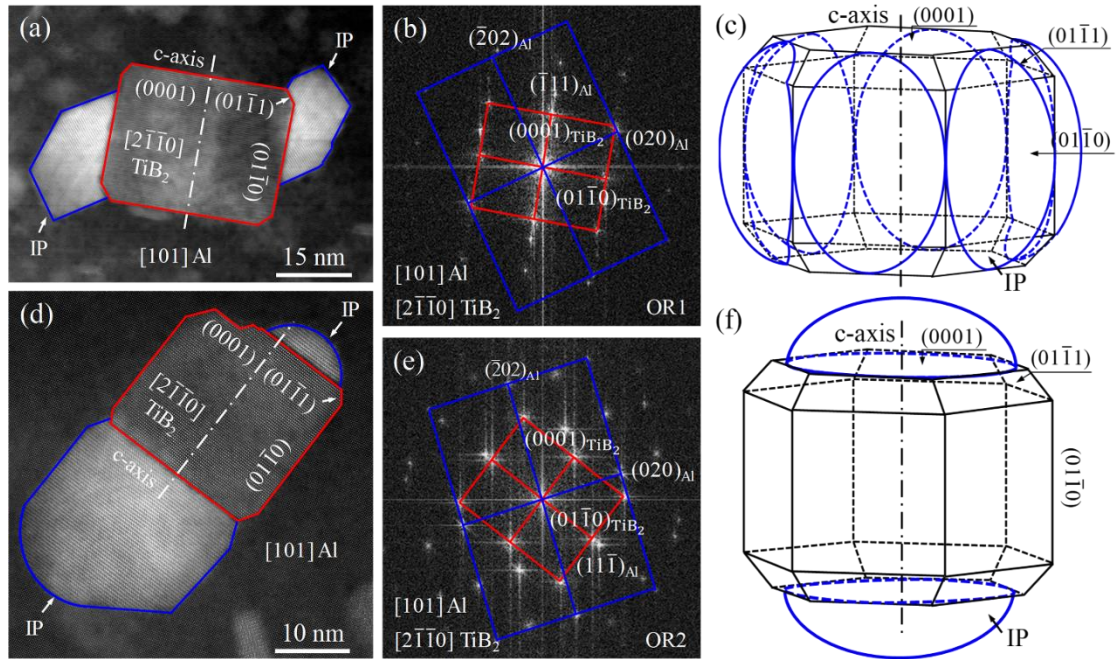


Fig. 4.6 (a) STEM-HAADF image showing interphase formed at the  $\text{TiB}_2/\text{Al}$  interface exhibiting the OR1 between  $\text{TiB}_2$  nanoparticle and Al matrix revealed by corresponding FFT pattern (b) and schematic drawing (c). (d) STEM-HAADF image showing another interphase formed at the  $\text{TiB}_2/\text{Al}$  interfaces exhibiting the OR2 between  $\text{TiB}_2$  nanoparticle and Al matrix revealed by corresponding FFT pattern (e) and schematic drawing (f). The projection direction is  $[2\bar{1}\bar{1}0]_{\text{TiB}_2} // [101]_{\text{Al}}$ . See the text for more details.

At the overaged/OR2 condition (Fig. 4.8), two ORs, the OR5 between interphase and Al matrix, and the OR6 between  $\text{TiB}_2$  and interphase, were observed. They are:

The OR5:  $[1\bar{1}00]_{\text{IP}} // [101]_{\text{Al}}$ ,  $(11\bar{2}0)_{\text{IP}} // (11\bar{1})_{\text{Al}}$ ,

$(\bar{1}\bar{1}24)_{\text{IP}}$   $3^\circ$  from  $(\bar{2}02)_{\text{Al}}$ ,  $(11\bar{2}8)_{\text{IP}}$   $3^\circ$  from  $(020)_{\text{Al}}$

The OR6:  $[2\bar{1}\bar{1}0]_{\text{TiB}_2} // [1\bar{1}00]_{\text{IP}}$ ,  $(0001)_{\text{TiB}_2} // (0004)_{\text{IP}}$ ,  $(01\bar{1}0)_{\text{TiB}_2} // (11\bar{2}0)_{\text{IP}}$

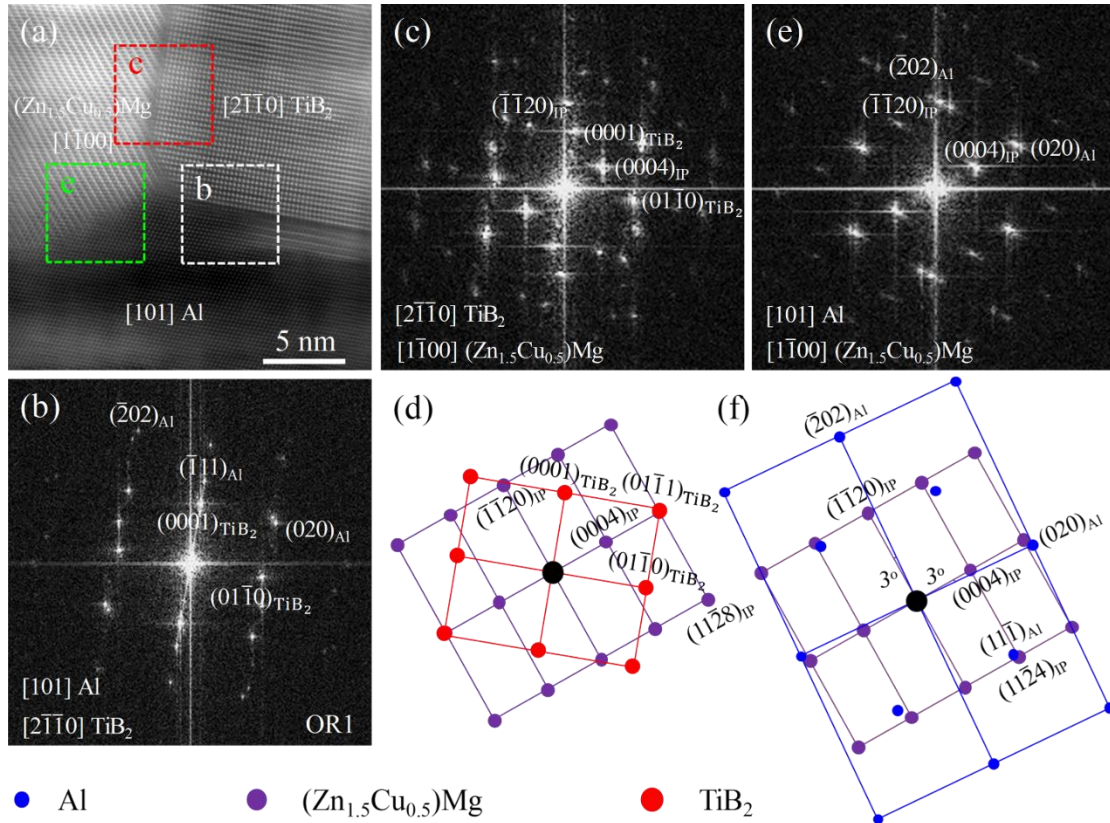


Fig. 4.7 (a) HRSTEM-HAADF image showing the Al/IP/TiB<sub>2</sub> multi-interfaces at the OR1; (b), (c) and (e) corresponding FFT patterns of box areas namely b, c and e given in (a) exhibiting the mutual ORs between the TiB<sub>2</sub> nanoparticle, interphase and Al matrix; (d) and (f) simulated diffraction patterns corresponding to (c) and (e), respectively. The projection direction is  $[2\bar{1}\bar{1}]_{\text{TiB}_2}/[1\bar{1}0]_{\text{IP}}/[101]_{\text{Al}}$ . See the text for more details.

It should be noted, in terms of extensive STEM examinations, that the ORs related to the interphase are only associated with the initial OR1 and OR2 between the TiB<sub>2</sub> nanoparticle and Al matrix at the solid-solution state. There is no correlation with the ageing treatments (peak- or over ageing).

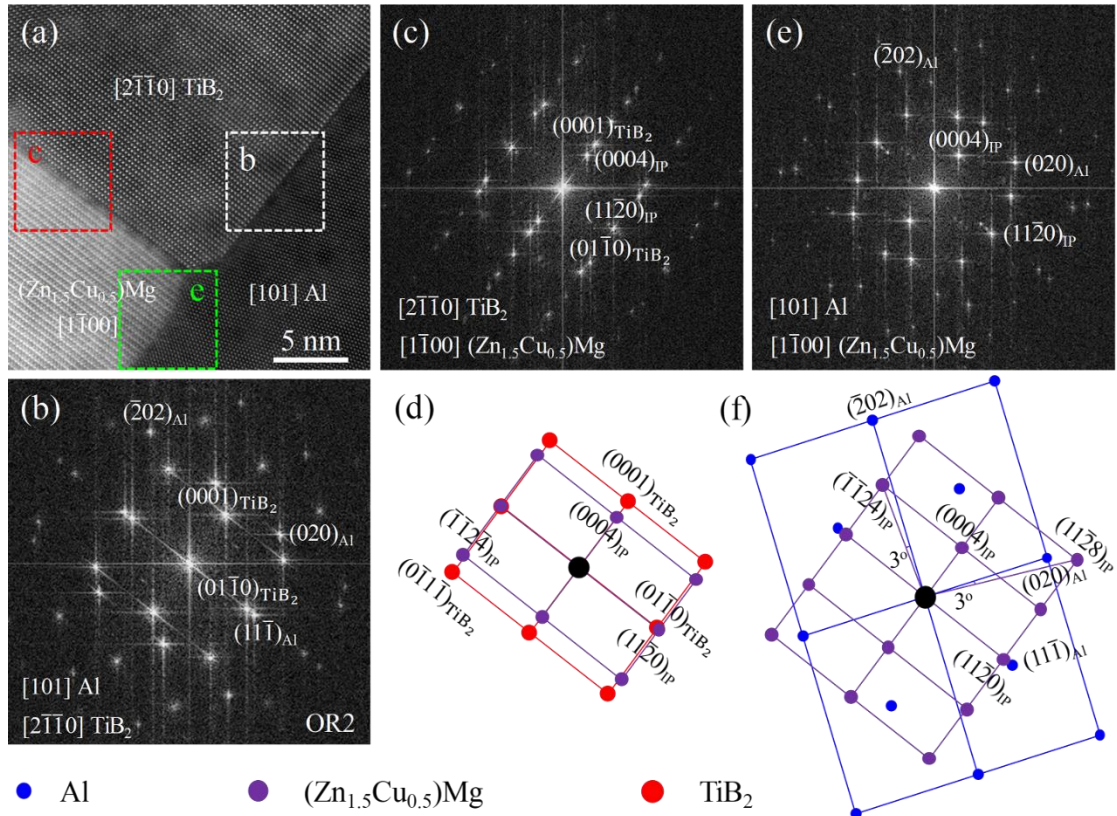


Fig. 4.8 (a) HRSTEM-HAADF image showing the Al/IP/TiB<sub>2</sub> multi-interfaces at the OR2. (b), (c) and (e) corresponding FFT patterns of box areas namely b, c and e given in (a) exhibiting the mutual ORs between the TiB<sub>2</sub> nanoparticle, interphase and Al matrix; (d) and (f) simulated diffraction patterns corresponding to (c) and (e), respectively. The projection direction is  $[2\bar{1}\bar{1}]_{\text{TiB}_2}/[1\bar{1}0]_{\text{IP}}/[101]_{\text{Al}}$ . See the text for more details.

#### 4.3.2.3 Atomic structure of the Al/(Zn<sub>1.5</sub>Cu<sub>0.5</sub>)Mg interphase/TiB<sub>2</sub> multi-interfaces

At the interphase/Al interfaces (i.e. the OR3, Fig. 4.9), the interphase precipitate grew based on  $(0008)_{\text{IP}}$  planes along the growth direction  $\langle 0001 \rangle_{\text{IP}}$ . It includes a half-grown zone (HGZ) at the growth front and a fully-grown zone (FGZ) next to it. The atomic structure of both zones is slightly different where the FGZ exhibits the typical structure corresponding to the  $(\text{Zn}_{1.5}\text{Cu}_{0.5})\text{Mg}$  phase without misfit dislocations inside. The two formed FGZ/Al interfaces  $(\bar{1}\bar{1}20)_{\text{IPFGZ}}$   $3^\circ$  from  $(\bar{2}02)_{\text{Al}}$  and  $(11\bar{2}4)_{\text{IPFGZ}}/(11\bar{1})_{\text{Al}}$  contain one and no misfit dislocation and agree with the theoretical mismatch values of

3.31 and 0.08 % (Table 4.2), respectively. Comparatively, the structure of the HGZ suggests its transition feature. From the growth front (i.e. the fully-coherent interface  $(020)_{Al} // (0008)_{IP_{HGZ}}$ ) to the HGZ/FGZ interface, the  $(0008)_{IP}$  plane gradually deviates up to  $3^\circ$  away from the initial direction being completely parallel to  $(020)_{Al}$ , while its interplanar spacing increases from 0.203 to 0.210 nm. Similar structure evolution of the  $(11\bar{2}4)_{IP}$  plane is also observed where its interplanar spacing decreases from 0.234 to 0.219 nm. The HGZ contains misfit dislocations where the four periodically spaced misfit dislocations (Fig. 4.9b) formed at the arc-shaped HGZ/FGZ interface and two misfit dislocations inside the zone (Fig. 4.9c). Furthermore, a few misfit dislocations are observed at the HGZ/Al interfaces  $(11\bar{2}4)_{IP_{HGZ}} // (11\bar{1})_{Al}$  and  $(\bar{1}\bar{1}20)_{IP_{HGZ}} // 3^\circ$  from  $(\bar{2}0\bar{2})_{Al}$ . As detailed in Fig. 4.10, the interphase/TiB<sub>2</sub> interface  $(11\bar{2}8)_{IP} // (01\bar{1}0)_{TiB_2}$  contains two periodically spaced misfit dislocations (Fig. 4.10b) having the low mismatch of 2.94 % (Table 4.2). However, the interface  $(0008)_{IP} // (01\bar{1}1)_{TiB_2}$  displays four misfit dislocations (Fig. 4.10c), suggesting that the observed interphase was not directly nucleated at this interface considering the precipitation kinetics and the very high mismatch of 60.74 % (Table 4.2).

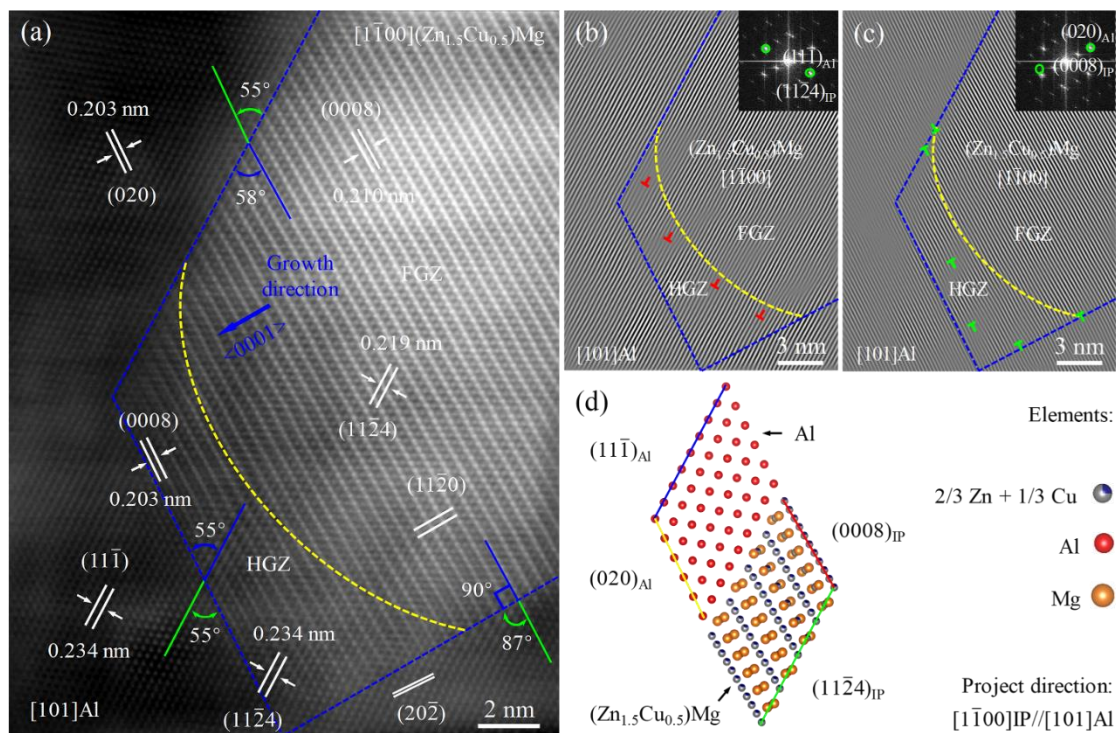


Fig. 4.9 (a) HRSTEM-HAADF image showing atomic structure of the Al/IP interfaces at the OR1. (b) and (c) inverse FFT patterns of (a) using different reflection pairs selected in corresponding FFT patterns in insets and (d) simulated atomic structure model showing the Al/IP interface  $(11\bar{1})_{Al} // (11\bar{2}4)_{IP}$ . The projection direction is  $[1\bar{1}00]_{IP} // [101]_{Al}$ . See the text for more details.

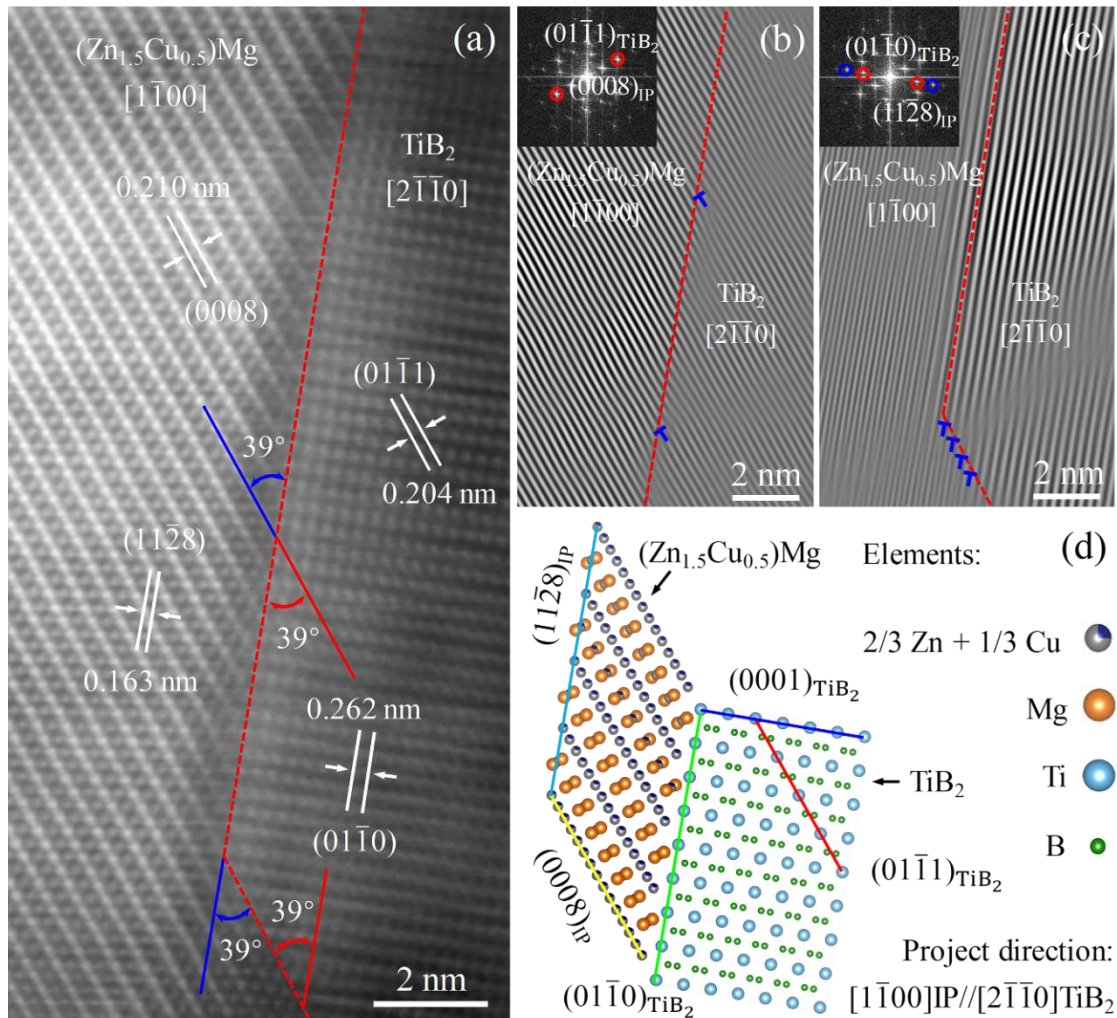


Fig. 4.10 (a) HRSTEM-HAADF image showing atomic structure of the IP/TiB<sub>2</sub> interfaces at the OR1. (b) and (c) inverse FFT patterns of (a) using different reflection pairs selected in corresponding FFT patterns in insets and (d) simulated atomic structure model showing the IP/TiB<sub>2</sub> interface  $(11\bar{2}8)_{IP} // (01\bar{1}0)_{TiB_2}$ . The projection direction is  $[2\bar{1}\bar{1}0]_{TiB_2} // [1\bar{1}00]_{IP}$ . See the text for more details.

At the overaged/OR2 condition (Fig. 4.11), the interphase grew based on the

(0004)<sub>IP</sub> planes along the growth direction  $\langle 0001 \rangle_{IP}$ , being the same as in the peak-aged/OR1 case. However, the whole interphase is fully developed without the HGZ and no misfit dislocations visible inside (Figs. 4.11b and 4.11d). Only the misfit dislocations, spaced at approximately 2.7 and 1.25 nm intervals (Table 4.2), are observed at the arc-like (Figs. 4.11a and 4.11b) and shape interphase/Al interfaces (Figs. 4.11c and d), respectively. Finally, Fig. 4.12 shows that the interphase/TiB<sub>2</sub> interface displays only one misfit dislocation, being in agreement with the theoretical mismatch of 2.34 % (Table 4.2).

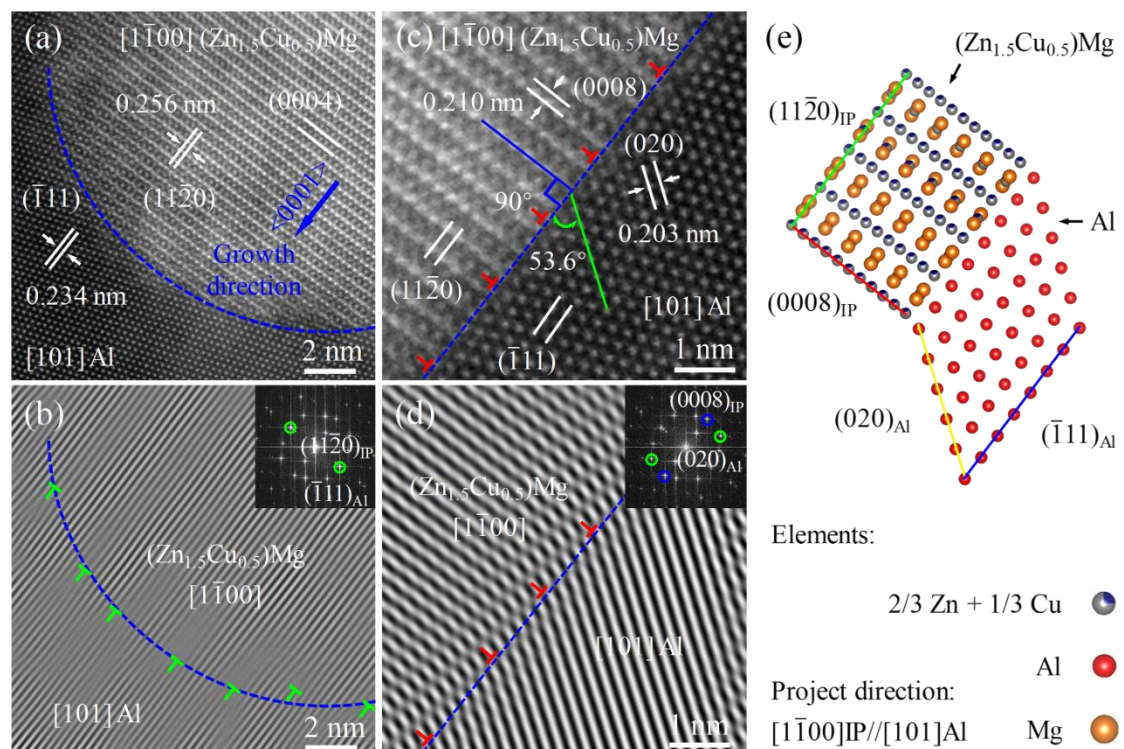


Fig. 4.11 HRSTEM-HAADF images showing atomic structure of the Al/IP interfaces at the OR2: (a) the arc-shaped interface at the growth front of the interphase and (c) interface  $(\bar{1}11)_{Al} // (11\bar{2}0)_{IP}$ . (b) and (d) inverse FFT patterns of (a) and (c) using different reflection pairs selected in corresponding FFT patterns in insets, respectively and (e) Simulated atomic structure models showing the Al/IP interface  $(\bar{1}11)_{Al} // (11\bar{2}0)_{IP}$ . The projection direction is  $[1\bar{1}00]_{IP} // [101]_{Al}$ . See the text for more details.

Table 4.2 Coherency of the Al/interphase/TiB<sub>2</sub> multi-interfaces at the OR1 and OR2 conditions. Note that high, intermediate and low interface coherency are defined as the interface mismatch below 5%, in the range 5-25% and above 25%, respectively.

| ORs between TiB <sub>2</sub> and Al | Interface type                     | Interface planes  | Interface mismatch (%) | Misfit dislocation interval (nm) | Interface Coherency |
|-------------------------------------|------------------------------------|---|------------------------|----------------------------------|---------------------|
| OR1 (Fig.4.7)                       | Al/IP<br>(Fig. 4.9)                | (020) <sub>Al</sub> //(0008) <sub>IP<sub>HGZ</sub></sub>                                    | 0                      | —                                | High                |
|                                     |                                    | (11 $\bar{1}$ ) <sub>Al</sub> //(11 $\bar{2}$ 4) <sub>IP<sub>FGZ</sub></sub>                | 0.08                   | 322.99                           | High                |
|                                     |                                    | ( $\bar{2}$ 02) <sub>Al</sub> 3° from<br>( $\bar{1}\bar{1}$ 20) <sub>IP<sub>FGZ</sub></sub> | 3.31                   | 6.35                             | High                |
|                                     | IP/TiB <sub>2</sub><br>(Fig. 4.10) | (11 $\bar{2}$ 8) <sub>IP</sub> //(01 $\bar{1}$ 0) <sub>TiB<sub>2</sub></sub>                | 2.94                   | 11.35                            | High                |
|                                     |                                    | (0008) <sub>IP</sub> //(01 $\bar{1}$ 1) <sub>TiB<sub>2</sub></sub>                          | 60.74                  | 0.68                             | Low                 |
| OR2 (Fig. 4.8)                      | Al/IP<br>(Fig. 4.11)               | Arc-shaped  | 9.40                   | 2.70                             | Intermediate        |
|                                     |                                    | (11 $\bar{1}$ ) <sub>Al</sub> //(11 $\bar{2}$ 0) <sub>IP<sub>FGZ</sub></sub>                | 20.10                  | 1.25                             | Intermediate        |
|                                     | IP/TiB <sub>2</sub><br>(Fig. 4.12) | (11 $\bar{2}$ 0) <sub>IP</sub> //(01 $\bar{1}$ 0) <sub>TiB<sub>2</sub></sub>                | 2.34                   | 11.18                            | Low $\delta$        |

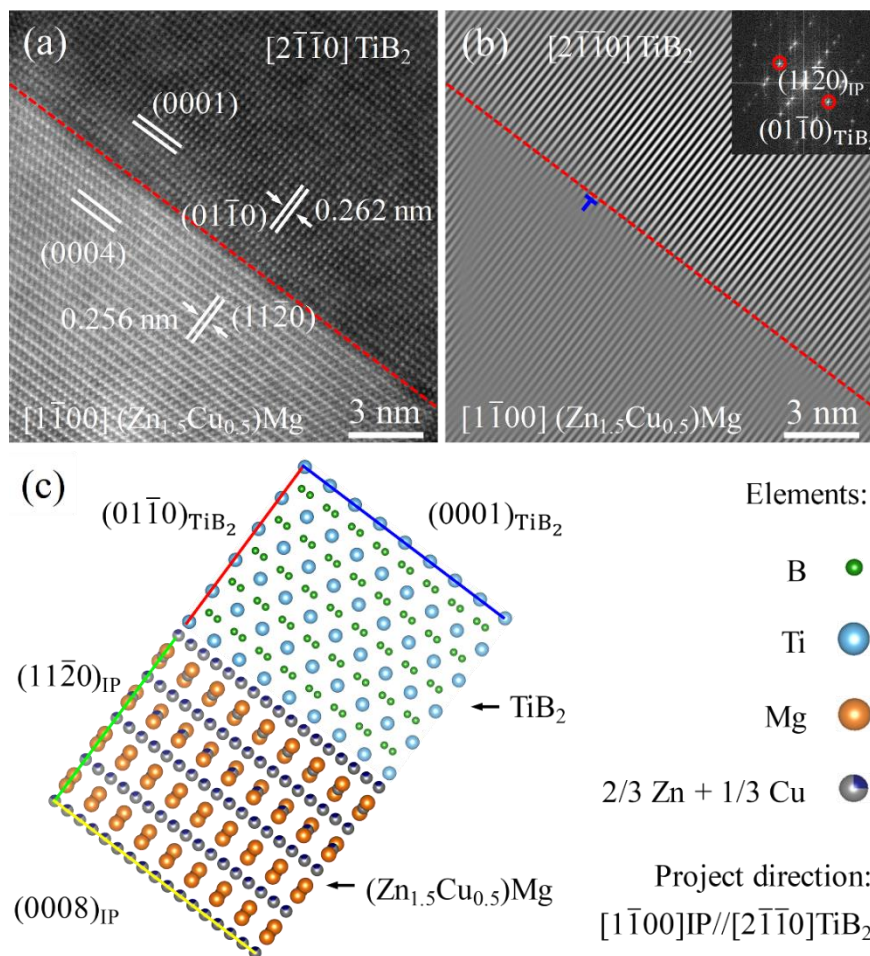


Fig. 4.12 (a) HRSTEM-HAADF image showing atomic structure of the IP/TiB<sub>2</sub> interface at the OR2. (b) inverse FFT pattern of (a) using reflection pairs selected in corresponding FFT pattern in inset and (c) simulated atomic structure model showing the IP/TiB<sub>2</sub> interface (0001)<sub>TiB<sub>2</sub></sub>//(0008)<sub>IP</sub>. The projection direction is  $[2\bar{1}\bar{1}0]_{\text{TiB}_2} // [1\bar{1}00]_{\text{IP}}$ . See the text for more details

#### 4.4 Discussion

In the TiB<sub>2</sub>/Al-Zn-Mg-Cu composite, our atomic scale investigation clearly demonstrates that the homogenous distribution of TiB<sub>2</sub> nanoparticles has exerted disparate influences on the precipitation reactions in the Al matrix near the TiB<sub>2</sub>/Al interface (i.e. the NRP/Al type). Such an interface had following features: (1) No CPZs were formed (Figs. 4.3a and 4.3e) due to the absence of TSIDs (Fig. 4.1a). (2) The semi-coherent and clean TiB<sub>2</sub>/Al interface (Figs. 4.2a and 4.2d) is incapable to lead to vacancy or solute depletion, and thus no PFZs formed [83, 100-102]. It has been well documented that the formation of CPZs or PFZs is detrimental to mechanical properties of MMCs [33-35]. Thus, it is expected that their absence would be beneficial to the present MMCs. (3) The OR-dependent heterogeneous precipitations were promoted at the TiB<sub>2</sub>/Al interface considering the much larger sizes of the interphase in comparison with those of the nano-precipitates formed in the matrix away from the interface (Fig. 4.3). The interphase precipitates in both the peak-aged and overaged samples were identified to be the (Zn<sub>1.5</sub>Cu<sub>0.5</sub>)Mg phase and show specific ORs with the TiB<sub>2</sub> nanoparticle and the Al matrix (Figs. 4.6-4.8). The main difference is that the HGZ only exists at the growth front of the interphase at the peak-aged state witnessing its transitional nature (Fig. 4.9). The corresponding underlying mechanisms of the heterogeneous precipitation reactions at the TiB<sub>2</sub>/Al interfaces are discussed in detail below.

#### 4.4.1 Reduced nucleation energy barrier for the interphase precipitation

For the homogenous precipitation in the Al alloy matrix, the minimum activation energy barrier  $\Delta G_{hom}^*$  can be expressed using the following equation [37]:

$$\Delta G_{hom}^* = -\frac{16\pi\gamma_{\alpha\beta}^3}{3(\Delta G_V - \Delta G_S)^2} \quad (4.1)$$

where  $\gamma_{\alpha\beta}$  and  $\Delta G_V$  are the interfacial energy and difference in free energy (per unit volume) between the Al matrix ( $\alpha$ ) and the precipitate ( $\beta$ ), respectively;  $\Delta G_S$  is the misfit strain energy (per unit volume) of the precipitate. Analogously, for the heterogeneous precipitation at the TiB<sub>2</sub>/Al interface, the equation for the minimum activation energy barrier  $\Delta G_{het}^*$  is expressed by [37, 38]:

$$\Delta G_{het}^* = -\frac{4}{3}\pi \frac{\gamma_{\alpha\beta}^3}{(\Delta G_V - \Delta G_S)^2} (2 - 3\cos\theta + \cos\theta^3) \quad (4.2)$$

where  $\gamma_{\alpha\beta}$ ,  $\Delta G_V$  and  $\Delta G_S$  are the same as in Eq. (4.1),  $\theta$  is the contact angle between the nucleus of the interphase and the TiB<sub>2</sub> substrate.

Consequently, the relationship between  $\Delta G_{hom}^*$  and  $\Delta G_{het}^*$  is acquired and expressed by the following equation:

$$\frac{\Delta G_{het}^*}{\Delta G_{hom}^*} = \frac{1}{4} (2 - 3\cos\theta + \cos\theta^3) = f(\theta) \quad (4.3)$$

According to Fig. 4.3, the contact angle between the interphase and TiB<sub>2</sub> substrate was measured to be 60°. Thus,  $f(\theta)$  is calculated to be 0.156. Obviously, the energy barrier for the heterogeneous precipitations at the TiB<sub>2</sub>/Al interface is considerably reduced compared with the homogeneous nucleation in the Al matrix away from the interface.

In addition, from Fig. 4.2, highly-dense misfit dislocations are observed at the TiB<sub>2</sub>/Al interfaces in the sample after solid-solution treatment. The stress field generated by these misfit dislocations could be the driving force for the migration of solute atoms (Zn, Mg, Cu etc.) on the substitutional sites towards the dislocations [112, 113]. The segregation of solute atoms along the misfit dislocation lines at the TiB<sub>2</sub>/Al interfaces therefore led to the formation of Cottrell atmospheres. This is in good agreement with the observed solute-enriched regions at the TiB<sub>2</sub>/Al interfaces in Fig.

4.1b. Moreover, it has been well-documented that vacancies, being essential for the nucleation of precipitates, are readily affected by the stress field caused by dislocations [22, 114]. Vacancies could migrate towards the misfit dislocations at the TiB<sub>2</sub>/Al interfaces during the subsequent aging treatments [114]. Solute-vacancy clusters thus form and transform to the nucleus once vacancies approach solute atoms in the solute-enriched regions located at the TiB<sub>2</sub>/Al interfaces [55, 115]. The interactions between the solute atoms, vacancies and misfit dislocations at the TiB<sub>2</sub>/Al interfaces can be beneficial to the nucleation of the interphase precipitates [112, 116].

#### 4.4.2 Accelerated growth rate for the interphase precipitation

As proposed by the previous studies, the lattice distortion near dislocation cores effectively lower the activation energy for solute atoms diffusion [62, 117, 118]. The dislocation cores can act as fast diffusion paths for solute atoms enabling the rapid growth of precipitates on dislocations [58, 65] and promoting the precipitation of nanoscale precipitates [61, 119]. In this case, the accelerated growth of the interphase (Fig. 4.3) is also attributed to the misfit dislocations presenting at the semi-coherent TiB<sub>2</sub>/Al interface (Fig. 4.2).

As a diffusion-controlled phase transformation, the precipitation in Al-Zn-Mg(-Cu) alloys depends on the diffusion of solute atoms, i.e., Mg, Zn (Cu) in the Al matrix [38]. For the ideal crystal structure with no defects, the solute atoms diffuse randomly by substitution, advancing a radial distance according to the following equation [60]:

$$\begin{cases} x = \sqrt{6Dt} \\ D = D_0 \exp \frac{-Q}{RT} \end{cases} \quad (4.4)$$

where D is the bulk diffusivity with units (m<sup>2</sup>/s); D<sub>0</sub> is a material constant; Q is the activation energy for substitutional diffusion; R is the universal gas constant (=8.3145 J/mol K); and T is the absolute temperature in Kelvin. According to the reports of Ma *et al.* [63], the bulk diffusivity rates of Mg and Zn (Cu) are 1.7 × 10<sup>-21</sup> m<sup>2</sup>/s and 7.4 × 10<sup>-22</sup> m<sup>2</sup>/s at the aging temperature of 120 °C, respectively. Zn (Cu) thus is the diffusion-

rate limiting elements in Al-Zn-Mg(-Cu) alloys.

For the homogenous precipitations in Al-Zn-Mg(-Cu) alloys, the radius of the initially nucleated embryo can be illustrated by the Zener-Hillert model [38]:

$$\frac{dr}{dt} = \frac{D(c - c_e)}{r_p(c_p - c_e)} \left(1 - \frac{r_c}{r_p}\right) + \frac{1}{N} \frac{dN}{dt} (\alpha r^* - r) \quad (4.5)$$

where  $r$  is the radius of the  $\eta'$  phase;  $c$  is the current solute concentration of the matrix;  $c_e$  is the equilibrium solute concentration of the matrix and  $c_p$  is the solute concentration at the equilibrium precipitate/matrix interface;  $r_p$  is the radius of platelet tip and  $r_c$  is the critical platelet tip radius at which growth would stop for capillarity effects reducing the driving force for solute diffusion to zero;  $N$  is the precipitate density;  $\alpha$  is the numerical factor accounts for the fact that nucleated precipitates can grow only when their radius is slightly larger than the radius  $r^*$ , ( $r > r^*$  and  $dN/dt > 0$ ), otherwise, they dissolve into the matrix.

When dislocations are involved, the growth rate of the precipitate is accelerated by an enhancement factor expressed as [57, 120]:

$$f = 1 + \frac{b\sqrt{2}}{\pi r} \sqrt{f(t')} \frac{\sqrt{D_p}}{\sqrt{D}} \quad (4.6)$$

where  $f$  is the enhancement factor that pipe diffusion enhancing the precipitate growth rate,  $D$  is the bulk diffusivity of the rate-controlling solute species;  $D_p$  is the diffusivity of the rate-limiting species along the dislocation core;  $b$  is the Burgers vector; the core width of the dislocation is assumed to be equal to  $2b$ ;  $f(t')$  can be expressed by the following equation:

$$f(t') = \int_0^\infty \frac{\exp(-t'x^2)}{x[J_0^2(x) + Y_0^2(x)]} dx \quad (4.7)$$

where  $J_0(x)$  and  $Y_0(x)$  are the zeroth-order Bessel functions of the first and second kind.

The integral in Eq. (4.7) is time dependent but for typical values of time from 100-1000 s has a value from 0.85 to 0.62 [57]. Deschamps *et al.* [57, 58] have estimated that in Al-Zn-Mg(-Cu) alloys  $D_p$  is on the order of  $10^{-17}$  m<sup>2</sup>/s at the aging temperature of 120 °C.  $D$  for the rate-limiting solute species Zn(Cu) is  $7.4 \times 10^{-22}$  m<sup>2</sup>/s [63].  $b$  is 0.286

nm for Al [121].  $r$  is approximate to 4 nm as shown in Fig. 4.3b. Substituting these parameters to Eq. (4.6), the enhancement factor is approximated to be  $\sim 3.95$ . According to Fig. 4.3a, the radius of the interphase heterogeneously precipitated at the  $\text{TiB}_2/\text{Al}$  interfaces is around 17 nm. Consequently, the enhanced precipitate growth factor observed experimentally at the peak-aged state is calculated to be 4.25, which is approximate to the enhancement factor of 3.95 acquired by Eq. (4.6).

#### 4.4.3 Preferential $\text{TiB}_2/\text{Al}$ interfaces for suppressing the interphase precipitation

As shown in Fig. 4.6, the precipitation depended on the ORs between the  $\text{TiB}_2$  nanoparticles and the Al matrix. For the OR1, the interphase preferentially formed on the prismatic  $\{01\bar{1}0\}$  and pyramidal  $\{01\bar{1}1\}$  facets of the  $\text{TiB}_2$  nanoparticle. But, the OR2 resulted in the precipitation on the basal  $\{0001\}$  facets. The common feature is that the  $\text{TiB}_2/\text{Al}$  interfaces was parallel to the close-packed  $\{111\}$  planes of the Al matrix and remained ‘clean’ after the ageing treatments, i.e. the suppression of the interphase precipitation.

It has been well established that the precipitation in the Al-Zn-Mg(-Cu) alloys is caused by diffusional nucleation followed by effective growth [6, 122]. As discussed above (Section 4.4.1), the  $\text{TiB}_2/\text{Al}$  interfaces are the favorable sites for nucleation of the interphase. Indeed, a closer look confirm that, for example for the OR1 (Figs. 4.13a and 4.13b), the interphase has nucleated at the  $\text{TiB}_2/\text{Al}$  interface being parallel to the basal  $\{0001\}$  facets of the  $\text{TiB}_2$  particle, while its growth has been suppressed. It is well-known that the growth of precipitates is essentially the process where a nucleus/matrix interface migrates into the surrounding parent phase by transferring atoms across the moving interface [37]. In this case, the suppression of the precipitation can be understood by the fact that a coherent close-packed interface between the embryo of the hcp interphase and the fcc Al matrix was formed during the nucleation stage (Fig. 4.13a). As schematically illustrated in Figs. 4.13c and 4.13d and was reported in Refs. [51, 123, 124] that the atom on a C site in the fcc Al matrix must change into a B position to make the interphase growth happen. This should result in a

very high energy and unstable configuration with two atoms directly above each other on B sites [37]. In addition, a loop of Shockley partial dislocation is necessarily created around the atom [124]. An atom attempting such a jump will, therefore, be unstable and be forced back to its original position [37, 124]. Thus, the growth at the coherent close-packed embryo/Al interface is very difficult, i.e., very low accommodation factors and low mobility.

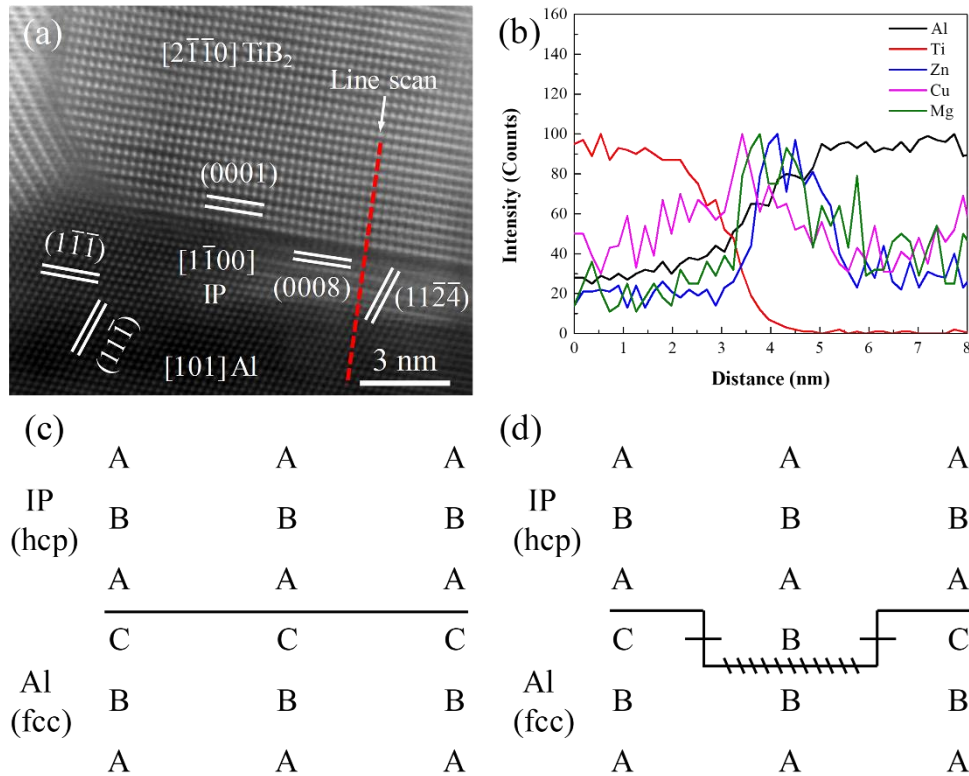


Fig. 4.13 (a) HRSTEM-HAADF image showing coherent Al/IP/TiB<sub>2</sub> interfaces parallel to the close-packed (1 $\bar{1}\bar{1}$ )<sub>Al</sub> planes, (b) EDX line profiles across the interface showing the embryo of the interphase rich in Zn, Mg and Cu elements; (c) and (d) schematic drawings illustrating the precipitation suppression mechanism associated with the growth of coherent close-packed interface between the hcp embryo of the interphase and fcc Al matrix.

#### 4.4.4 Crystallographic ORs between TiB<sub>2</sub> nanoparticles, interphase and Al alloy matrix

In order to further understand the experimentally determined ORs, the edge-to-edge

matching (E2EM) model is used to predict/calculate the possible ORs between the phases based on the basic crystallographic data, including lattice parameters and actual atomic positions, of the phases [125-127]. The E2EM calculation process includes: (a) identifying the closed-packed (CP) atomic row pairs and the CP plane pairs in phases; (b) calculating the values of interatomic spacing misfit ( $f_r$ ) and interplanar spacing mismatch ( $f_d$ ); and (c) predicting and refining the ORs between any two phases based on the rules that the matching directions must be on the matching planes and the parallel  $\Delta g_s$  conditions [128, 129]. The lattice parameter of pure Al metal is used in the present work. It is  $a = 0.40494$  nm. As a simple FCC structure, there are three possible close packed or nearly close packed directions. They are  $\langle 110 \rangle_{Al}$ ,  $\langle 100 \rangle_{Al}$  and  $\langle 112 \rangle_{Al}$ . The close packed plane for FCC is  $\{111\}_{Al}$  and this contains the  $\langle 110 \rangle_{Al}$  directions and the  $\langle 112 \rangle_{Al}$  directions.  $\{200\}_{Al}$  is the second close packed plane and this contains the  $\langle 110 \rangle_{Al}$  directions and the  $\langle 100 \rangle_{Al}$  directions. The third close packed plane is  $\{220\}_{Al}$ , and this contains all three of the above directions.  $TiB_2$  has hexagonal lattice structure with  $a = 0.3038$  nm and  $c = 0.3262$  nm and belongs to  $P6/mmm$  space group. There are four possible close or nearly close packed directions and planes of  $TiB_2$ . They are  $\langle 11\bar{2}0 \rangle_{TiB_2}$ ,  $\langle 10\bar{1}0 \rangle_{TiB_2}$ ,  $\langle 11\bar{2}3 \rangle_{TiB_2}$ ,  $\langle 0001 \rangle_{TiB_2}$  and  $\{10\bar{1}1\}_{TiB_2}$ ,  $\{10\bar{1}0\}_{TiB_2}$ ,  $\{0001\}_{TiB_2}$ ,  $\{11\bar{2}0\}_{TiB_2}$ . The interphase  $(Zn_{1.5}Cu_{0.5})Mg$  (IP) also has an hexagonal lattice structure with lattice parameters  $a = 0.5124$  nm and  $c = 1.682$  nm and space group of  $P63/mmc$  [111]. Each unit cell contains 12 Zn atoms, 8 Mg atoms and 4 Cu atoms. This interphase has three possible close or nearly close packed directions,  $\langle 11\bar{2}0 \rangle_{IP}$ ,  $\langle 10\bar{1}0 \rangle_{IP}$ , and  $\langle 0001 \rangle_{IP}$  and five close packed or nearly close packed planes,  $\{22\bar{4}0\}_{IP}$ ,  $\{11\bar{2}0\}_{IP}$ ,  $\{0008\}_{IP}$ ,  $\{11\bar{2}4\}_{IP}$  and  $\{11\bar{2}3\}_{IP}$ . Based on these crystallographic data, the E2EM calculation predicted following ORs.

The predicted ORs between the Al matrix and the  $TiB_2$  nanoparticles are:

The OR-A:  $[2\bar{1}\bar{1}0]_{TiB_2} // [101]_{Al}$ ,  $(01\bar{1}1)_{TiB_2}$   $0.6^\circ$  from  $(020)_{Al}$

The OR-B:  $[1\bar{1}00]_{TiB_2} // [\bar{1}\bar{1}2]_{Al}$ ,  $(11\bar{2}0)_{TiB_2}$   $1.2^\circ$  from  $(\bar{2}20)_{Al}$

The OR-C:  $[2\bar{1}\bar{1}0]_{TiB_2} // [101]_{Al}$ ,  $(0\bar{1}10)_{TiB_2}$   $1.5^\circ$  from  $(\bar{1}\bar{1}1)_{Al}$

Considering the inherent error in FFT, the OR-A can be regarded as the OR1 and the OR-C as the OR2. The predicted OR-B was not experimentally observed in the present work.

Four ORs between the interphase and Al were calculated. They are:

The OR-D:  $[0001]_{IP} // [101]_{Al}, (\bar{4}220)_{IP}$  1.0° from  $(1\bar{3}\bar{1})_{Al}$

The OR-E:  $[1\bar{1}00]_{IP} // [101]_{Al}, (11\bar{2}3)_{IP}$  1.2° from  $(1\bar{1}\bar{1})_{Al}$

The OR-F:  $[1\bar{1}00]_{IP} // [101]_{Al}, (0008)_{IP}$  3.7° from  $(020)_{Al}$

The OR-G:  $[1\bar{1}00]_{IP} // [101]_{Al}, (11\bar{2}\bar{4})_{IP}$  1.3° from  $(20\bar{2})_{Al}$

Although the OR-D and the OR-E were not experimentally observed in the present work, one can see that the OR-F consists with the OR3 and the OR-G agrees well with the OR5.

From the OR-A and the OR-F, following OR can be deduced.

The OR-H:  $[2\bar{1}\bar{1}0]_{TiB_2} // [1\bar{1}00]_{IP}, (01\bar{1}1)_{TiB_2}$  < 4.3° from  $(0008)_{IP}$

This OR-H actually is consistent with the OR4. Similarly, the OR6 can also be deduced from the OR-C and the OR-G.

The above crystallographic analysis indicates that the interfaces in between the TiB<sub>2</sub> nanoparticles and the Al matrix in the composite produced using the *in-situ* mixed salt method were either coherent or semi-coherent. Such interfaces acted as preferred sites for precipitation of the (Zn<sub>1.5</sub> Cu<sub>0.5</sub>)Mg interphase during ageing treatment, this in turn impact on the mechanical properties of the composites.

#### 4.4.5 Effect of the aging conditions on the interphase evaluation

It was reported that the precipitation of T phase requires a high vacancy boundary diffusivity, i.e., at high-angle GBs or MRP/Al interface [22, 64, 65]. Different from as observed in the SiC/Al MMC [22], no transformation of the interphase from η to T phases is found when the aging condition is shifted from the peak-aged to overaged states (Figs. 4.4 and 4.5). This is due to the low boundary diffusivity of the semi-coherent TiB<sub>2</sub>/Al interface being unfavorable for promoting this transformation. Alternatively, our results (Figs. 4.9 and 4.11) reveal the disappearance of the

transitional HGZ from the peak-aged to overaged states. It is well known that the precipitation in Al-Zn-Mg(-Cu) alloys involves the formation of precipitates with a different composition compared to the matrix, and therefore long-range diffusion is required [37]. This is a continuous and time-consuming phase transformation process featured by thermally activated atomic movements [37, 38]. As such, a metastable transitional HGZ zone should always exist at the growth front as long as the phase transformation process has not completely accomplished at the peak-aged state. At the overaged state, the diffusion coefficient of the solute atoms is significantly enhanced as it increases exponentially with temperature according to Eq. (4.4). This results in the final stable interphase without the HGZ.

## 4.5 Conclusions

In this work, the TiB<sub>2</sub>/Al-Zn-Mg-Cu nanocomposite component produced by casting (in-situ reaction), FSP and hot extrusion was used as the model material for (HR)STEM characterization at the atomic scale. The specific structures of the TiB<sub>2</sub>/Al interface and the matrix away from the interface at the as-quenched, peak-aged and overaged states were revealed. The results indicate the significant effects of the TiB<sub>2</sub> nanoparticle on the precipitation reactions in the Al matrix surrounding the TiB<sub>2</sub>/Al interfaces, the formation of the interphase in particular depends on the ORs between the TiB<sub>2</sub> and Al matrix. The following conclusions can be drawn.

- (1) The majority of TiB<sub>2</sub> nanoparticles are uniformly dispersed inside Al grains, featured with the basal {0001}, prismatic {01 $\bar{1}$ 0} and pyramidal {01 $\bar{1}$ 1} facets. At the as-quenched state, the well-documented crystallographic OR1 ( $[2\bar{1}\bar{1}0]_{\text{TiB}_2} // [101]_{\text{Al}}$ ,  $(0001)_{\text{TiB}_2} // (\bar{1}11)_{\text{Al}}$ ) as well as the new OR2 ( $[2\bar{1}\bar{1}0]_{\text{TiB}_2} // [101]_{\text{Al}}$ ,  $(01\bar{1}0)_{\text{TiB}_2} // (11\bar{1})_{\text{Al}}$ ) at the TiB<sub>2</sub>/Al interface are determined. Periodically spaced misfit dislocations and solute-enriched regions and no obvious TSIDs are observed in the surrounding Al matrix next to this interface.

- (2) Preferential heterogeneous interface precipitates are closely related to the OR1 or OR2 conditions between the  $\text{TiB}_2$  and Al matrix, while being independent on the ageing conditions. The interphase is identified to be the  $(\text{Zn}_{1.5}\text{Cu}_{0.5})\text{Mg}$  phase both at the peak-aged and overaged states. At the OR1, The ORs between the  $\text{TiB}_2$  nanoparticles, interphase and the Al matrix are:  $[2\bar{1}\bar{1}0]_{\text{TiB}_2} // [1\bar{1}00]_{\text{IP}} // [101]_{\text{Al}}$ ,  $(01\bar{1}1)_{\text{TiB}_2} // (0004)_{\text{IP}}$   $3^\circ$  from  $(020)_{\text{Al}}$ ,  $(01\bar{1}0)_{\text{TiB}_2} // (11\bar{2}8)_{\text{IP}}$ ,  $(11\bar{2}4)_{\text{IP}} // (11\bar{1})_{\text{Al}}$ ,  $(\bar{1}\bar{1}20)_{\text{IP}}$   $3^\circ$  from  $(\bar{2}02)_{\text{Al}}$ . At the OR2, the ORs are:  $[2\bar{1}\bar{1}0]_{\text{TiB}_2} // [1\bar{1}00]_{\text{IP}} // [101]_{\text{Al}}$ ,  $(01\bar{1}0)_{\text{TiB}_2} // (11\bar{2}0)_{\text{IP}} // (11\bar{1})_{\text{Al}}$ ,  $(0001)_{\text{TiB}_2} // (0004)_{\text{IP}}$ ,  $(\bar{1}\bar{1}24)_{\text{IP}}$   $3^\circ$  from  $(\bar{2}02)_{\text{Al}}$ ,  $(11\bar{2}8)_{\text{IP}}$   $3^\circ$  from  $(020)_{\text{Al}}$ . These determined ORs agree with the predictions using the E2EM calculation.
- (3) At the peak-aged and overaged states, the mismatch of the Al/ $(\text{Zn}_{1.5}\text{Cu}_{0.5})\text{Mg}$  interphase/ $\text{TiB}_2$  multi-interfaces formed at the OR1 condition are generally very low (below 5 %) except the interphase/ $\text{TiB}_2$  interface  $(0008)_{\text{IP}} // (01\bar{1}1)_{\text{TiB}_2}$  planes. Comparatively, when formed at the OR2, the Al/interphase and interphase/ $\text{TiB}_2$  interfaces show very low (below 5 %) and intermediate mismatch values (in the range 5-25 %), respectively.
- (4) The energy barrier for the heterogeneous precipitations at the  $\text{TiB}_2/\text{Al}$  interface is considerably reduced compared to the homogeneous nucleation in the Al matrix away from such an interface. Highly-dense misfit dislocations at the  $\text{TiB}_2/\text{Al}$  interfaces are beneficial for the nucleation and effective growth of the interphase since they provide short-circuit diffusion paths for solute atoms and vacancies. The growth of the precipitates at the  $\text{TiB}_2/\text{Al}$  interfaces parallel to the close-packed  $\{111\}$  planes of the Al matrix is severely suppressed due to the ultra-low accommodation factor.
- (5) The precipitation process is not fully completed at the peak-aged state, which is featured with the transitional HGZ presenting at the growth front of the interphase. Compared with the FGZ, The HGZ contains misfit dislocations and slightly different interplanar spacing.

# Chapter 5 Simultaneously Increasing the Strength and Ductility of TiB<sub>2</sub> Nanoparticles Reinforced Al-Zn-Mg-Cu Matrix Composite via Precipitation-assisted Interface Strengthening

*In preparation for submission. Y. Ma, A. Addad, G. Ji, M. Zhang, W. Lefebvre, Z. Chen, V. Ji*

Strength and ductility are the two most important mechanical properties of a structural material. However, they are often mutually exclusive. In this study, an Al-Zn-Mg-Cu matrix composite reinforced with 6wt. % uniformly distributed TiB<sub>2</sub> nanoparticles (TiB<sub>2</sub>/Al-Zn-Mg-Cu nanocomposite) was designed and produced by the processing route combining casting, friction stir processing and hot extrusion. Through the peak-aging treatment, the high mismatch TiB<sub>2</sub>/Al interfaces with high coherency strains were transformed into the low mismatch Al/(Zn<sub>1.5</sub>Cu<sub>0.5</sub>)Mg interphase/TiB<sub>2</sub> multi-interfaces with very low coherency strains basically, by which the original TiB<sub>2</sub>/Al interfaces were greatly strengthened. Correspondingly, due to the combined effects of TiB<sub>2</sub>/dislocation interaction and precipitation assisted interface strengthening, the TiB<sub>2</sub>/Al-Zn-Mg-Cu nanocomposite presents a remarkable combination of strength (yield strength of 600 MPa) and ductility (uniform elongation of 12%), being higher than any Al or Al based materials ever reported.

## 5.1 Introduction

Strength and ductility are the two most important mechanical properties of a structural material. Unfortunately, for centuries engineers have been facing a dilemma

that they are often mutually exclusive, that is, a material may be strong or ductile, but rarely both at the same time [130]. In the past decades, accompanied by the rise of ultra-fine grained (UFG) and nanocrystalline (NC) materials, considerable attempts such as introducing nanoscale twin boundaries and generating bimodal or gradient nanograined structures have been made aiming to propose a roadmap of microstructure design for achieving both superior strength and plasticity [131-134]. It is well established that the strength of NC/UFG metals are significantly high due to the Hall-Petch relationship [135]. Simultaneously, the steady and progressive work-hardening mechanism caused by those designed gradient microstructures can lead to a high uniform elongation [131-134]. Despite the encouraging results, those approaches are short of commercially practical for industrial applications attributed to the insurmountable limitations: the scale limitation of the samples, the costly and tedious process to generate complex gradient microstructures and the instability of the involved metastable NC/UFG microstructures.

Introducing micron- (or submicron-) sized reinforcement particles (MRPs), such as SiC and B<sub>4</sub>C, into the Al alloys matrix provides an effective way to improve the tensile strength. However, the concurrently formed MRP/Al interfaces become the dominant defects in Al-based metal matrix composites (MMCs) [29]. During plastic deformation, the dislocations pile up at those weak interfaces and make them strong stress concentrative points [23, 24]. This further makes it appears hopeless for Al-based MMCs to have high elongation, and it has been taken for granted that they are super strong but inevitably low ductility.

Here we report a strategy for the design of Al-based nanocomposites with an exceptional combination of strength and ductility based on the concept of precipitation assisted interface strengthening (PAIS) mechanism. By conducting peak-aging heat treatment on the Al-Zn-Mg-Cu matrix composite reinforced with 6wt. % uniformly distributed TiB<sub>2</sub> nanoparticles (TiB<sub>2</sub>/Al-Zn-Mg-Cu nanocomposite), heterogeneous interface precipitate (interphase, abbr. IP) determined as (Zn<sub>1.5</sub>Cu<sub>0.5</sub>)Mg phase has

precipitated at the high mismatch semi-coherent  $\text{TiB}_2/\text{Al}$  interfaces. The formed  $\text{Al}/(\text{Zn}_{1.5}\text{Cu}_{0.5})\text{Mg}$  interphase/ $\text{TiB}_2$  multi-interfaces have low mismatch value, presenting much less coherency strains than at the original  $\text{TiB}_2/\text{Al}$  interface. As such, the  $\text{TiB}_2/\text{Al}$  interfaces are greatly strengthened. The tensile strength and uniform elongation of the as-processed  $\text{TiB}_2/\text{Al-Zn-Mg-Cu}$  nanocomposite are simultaneously enhanced via the combined effects of the  $\text{TiB}_2$ /dislocation interaction and precipitation assisted interface strengthening. It is worth noting that without NC/UFG structures involved, the  $\text{TiB}_2/\text{Al-Zn-Mg-Cu}$  composites fabricated by this strategy are very stable. Theoretically, our strategy is applicable to all of the nanosized reinforcement particles (NRPs) reinforced age-hardenable Al matrix composites, paving a cost-effective and scalable way for their large-scale industrial applications.

## 5.2 Experimental procedure

The  $\text{TiB}_2/\text{Al-Zn-Mg-Cu}$  Al composite sample was fabricated by an *in-situ* mixed salt method. First,  $\text{K}_2\text{TiF}_6$  and  $\text{KBF}_4$  reactive salts with high purity ( $>99.0\%$ ) were mixed and added into molten Al metal in a high-purity graphite crucible heated at  $900\text{ }^\circ\text{C}$  in an electrical resistance furnace. The melt was mechanically stirred at 600 revolutions per minute (rpm) for 15 min and was casted in a permanent mold to acquire the pre-synthesized master  $\text{TiB}_2$  reinforced pure Al composite. Zn, Mg and Al-Cu master alloy were subsequently added into the re-melted pre-synthesized master  $\text{TiB}_2/\text{Al}$  composite and homogenized for 10 min. Following this, the Al-Zn-Mg-Cu alloy reinforced with 6 wt.%  $\text{TiB}_2$  particles was fabricated by direct chill casting. The chemical composition of the matrix was Al-6.5Zn-2.3Mg-2.3Cu.

Plates with the dimension of  $200 \times 100 \times 16$  mm were cut from the cast ingot and annealed at  $470\text{ }^\circ\text{C}$  for 24 h. An optimized (4-pass) friction stir processing (FSP) process was carried out on the plates with a tool rotation rate of 600 rpm, a tool tilt angle of  $2.5^\circ$ , a traverse speed of 80 mm/min and a processing depth of 8 mm. More details can be found elsewhere [103]. Hot extrusion (extrusion ratio of 20:1) was carried

out on the samples cut from the nugget zone. Finally, the as-extruded sample was subjected to T6 heat treatment by solid solution at 477 °C for 70 min, quenched in water and aged at 120 °C for 24 h. The flow process chart of the TiB<sub>2</sub>/Al-Zn-Mg-Cu nanocomposite is given in Fig. 5.1. The quenched and aged samples were used for detailed characterization.

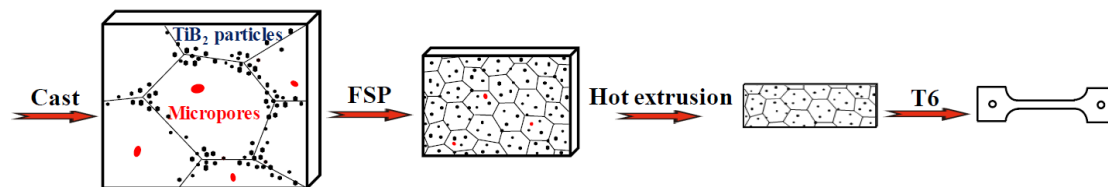


Fig. 5.1 The flow process chart of the TiB<sub>2</sub>/ Al-Zn-Mg-Cu composite.

The dog-bone tensile testing specimens were machined along the extrusion direction (ED) with gauge length of 2 mm × 3 mm × 10 mm. The tensile tests were carried out on a Zwick/Roell machine at a strain rate of 10<sup>-4</sup>/s at room temperature. Global microstructure at the micrometer scale was characterized by a JEOL JSM-7800F SEM instrument, equipped with a field emission gun (FEG), an energy dispersive spectrometry (EDS) system and an electron backscatter diffraction (EBSD) detector from Oxford instruments. Step size was set to 100 nm for EBSD acquisition.

Disk specimens of 3 mm in diameter were prepared by mechanical polishing and final ion milling by a GATAN precision ion polishing system, operated at - 150 °C using liquid nitrogen. A state-of-the-art FEI Titan Themis 300 microscope equipped with a probe aberration corrector, operated at 200 kV, was used to acquire (high-resolution) scanning transmission electron microscopy ((HR)STEM) images. Probe size was set to 0.1 nm with a convergence semi-angle of 22.5 mrad. Collection angle of the high-angle annular dark-field (HAADF) detector was in the range 80-150 mrad. Contrasts in an HAADF image is proportional to  $Z^{1.7-2}$ , meaning that the bright contrast indicates relatively heavy atomic composition [95]. In this case, the bright and dark contrasts can be considered as Zn (Cu)-rich and Mg-rich areas in the Al matrix, respectively. Particle/dislocation interaction was studied by annular dark-field (ADF)

image. Collection angle of the ADF detector was in the range 10-50 mrad. The equipped highly efficient (4 quadrant) EDS system was used for chemical analysis of possible precipitates formed at the  $\text{TiB}_2/\text{Al}$  interface. Interface characterization was carried out by tilting the Al matrix to the [101] orientation in terms of the well-documented preferential orientation relationship (OR) of the  $\text{TiB}_2/\text{Al}$  interfaces [84].

## 5.3 Results

### 5.3.1 Tensile properties

The engineering tensile stress-strain curves of  $\text{TiB}_2/\text{Al-Zn-Mg-Cu}$  nanocomposite and the commercial Al-Zn-Mg-Cu alloy reference material [2] are compared in Fig. 5.2a. The yield strength, ultimate strength and uniform elongation of the water-quenched  $\text{TiB}_2/\text{Al-Zn-Mg-Cu}$  nanocomposite is 250 MPa, 503 MPa and 25.1 % accordingly, which is higher than that of the unreinforced alloy (150 MPa, 370 MPa and 19 %). Analogously, compared to the unreinforced alloy (480 MPa, 560 MPa and 11.5%), the yield strength, ultimate strength and uniform elongation of the peak-aged  $\text{TiB}_2/\text{Al-Zn-Mg-Cu}$  nanocomposite is 600 MPa, 683 MPa and 12 % accordingly, presenting a remarkable combination of ductility and strength.

Fig. 5.2b summarizes the yield strength versus tensile ductility available from the literature for various Al materials, including: CG Al, Coml. Al, CS Al, NC/UFG Al, BG Al, AM Al, MRP/Al composite, CNT/Al composite and the present tensile results. It is apparent that some of the literature data have high strength but low ductility (located at the left-up corner), including NC/UFG Al and CNT/Al composite. Some of them show low strength but high ductility (located at the right-bottom corner), including CG Al, Coml. Al and CS Al. The rest show both low strength and ductility (located at the right-bottom corner), mainly including BG Al, AM Al, MRP/Al composite. These literature data approximately showing an inverse relationship between the strength and ductility. However, the current results from the peak-aged  $\text{TiB}_2/\text{Al-Zn-Mg-Cu}$  nanocomposites stand out from the trend, suggesting a superior combination of tensile

strength and ductility.

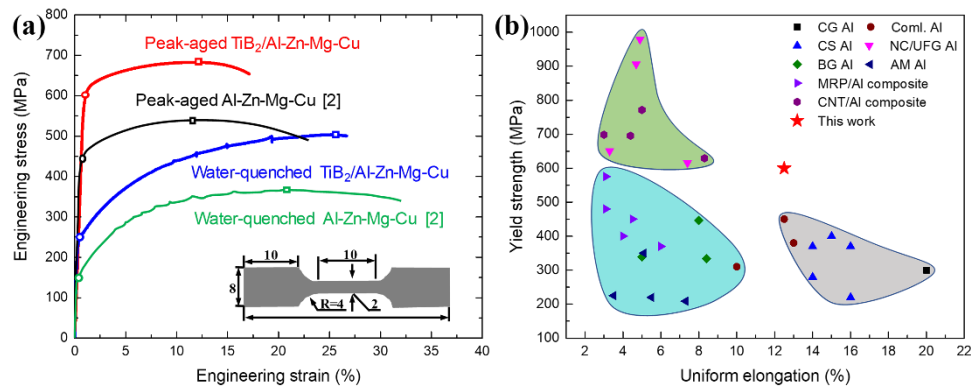


Fig. 5.2 (a) Tensile engineering stress-strain curves for water-quenched and peak-aged  $\text{TiB}_2/\text{Al-Zn-Mg-Cu}$  nanocomposite and commercial  $\text{Al-Zn-Mg-Cu}$  alloy [2]. The squares and circles mark the necking according to the Considère criterion and the start of yield strength of the samples. Inset shows the dimensions of the tensile samples with a thickness of 0.1 mm. R is the radius of the arc designated by the arrow. (b) A summary of yield stress versus uniform elongation for various Al materials, including coarse grain Al alloys (CG Al) [136], commercial Al alloys (Coml. Al) [2], cyclic strengthening processed Al alloys (CS Al) [2], NC/UFG Al alloys (NC/UFG Al) [2, 5], bimodal grain Al alloys (BG Al) [137, 138], additively manufactured Al alloys (AM Al) [139, 140], MRPs reinforced Al alloy matrix composite (MRP/Al composite) [7, 141], carbon nano-tube reinforced Al alloy matrix composite (CNT/Al composite) [142, 143] and  $\text{TiB}_2/\text{Al-Zn-Mg-Cu}$  nanocomposite (This work).

### 5.3.2 Microstructure

According to Fig. 5.3a and 5.3b,  $\text{TiB}_2$  particles are uniformly distributed in the Al alloy matrix. The majority of the  $\text{TiB}_2$  particles are 15-100 nm in size, with the average size measured to be 67 nm. Along and normal to ED, the average size of the equiaxed grains are 1.95  $\mu\text{m}$  (Fig. 5.3e) and 1.6  $\mu\text{m}$  (Fig. 5.3e), respectively. Consequently, the microstructure of the  $\text{TiB}_2/\text{Al-Zn-Mg-Cu}$  nanocomposite is generally uniform and isotropous owing to the effective FSP process.

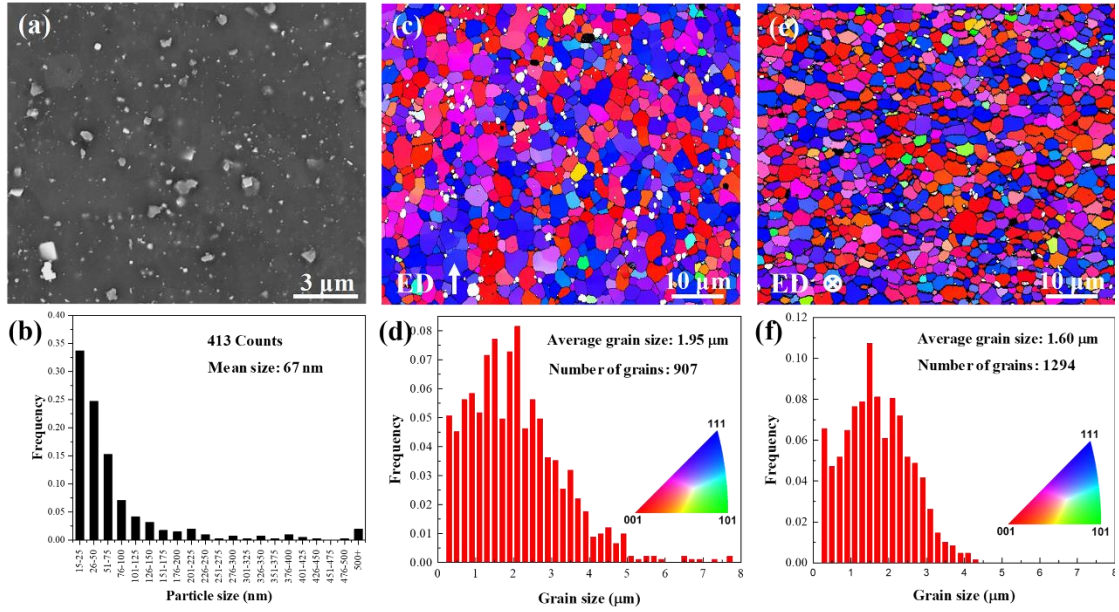


Fig. 5.3 (a) Typical SEM micrograph of the  $\text{TiB}_2/\text{Al-Zn-Mg-Cu}$  nanocomposite. (b) Size distribution of  $\text{TiB}_2$  particles based on SEM images. (c) Typical EBSD map of  $\text{TiB}_2/\text{Al-Zn-Mg-Cu}$  nanocomposite along ED. (d) Size distribution of matrix grains along ED based on the EBSD map in (c). (e) Typical EBSD map of  $\text{TiB}_2/\text{Al-Zn-Mg-Cu}$  nanocomposite normal to ED. (f) Size distribution of matrix grains normal to ED based on the EBSD map in (e). The color code representing the crystal orientation is included.

Similarly, most of the  $\text{TiB}_2$  nanoparticles are uniformly dispersed in the Al alloy matrix according to the TEM image shown in Fig. 5.4a. Consistent with the previous reports [108, 109], the  $\text{TiB}_2$  nanoparticles are faceted with basal  $\{0001\}$  prismatic  $\{01\bar{1}0\}$  and pyramidal  $\{01\bar{1}1\}$  facets (Fig. 5.4b). The  $\text{TiB}_2/\text{Al}$  interfaces are tightly bonded and free of oxide particles (Fig. 5.4b and 5.4c). According to Fig. 5.4d, the majority of  $\text{TiB}_2$  nanoparticles have the well-reported OR with the Al alloy matrix [84, 110]:

$$[2\bar{1}\bar{1}0]_{\text{TiB}_2} // [101]_{\text{Al}}, (0001)_{\text{TiB}_2} // (\bar{1}11)_{\text{Al}},$$

$$(01\bar{1}1)_{\text{TiB}_2} \ 3^\circ \text{ from } (020)_{\text{Al}}, (0\bar{1}12)_{\text{TiB}_2} \ 3^\circ \text{ from } (\bar{2}02)_{\text{Al}}$$

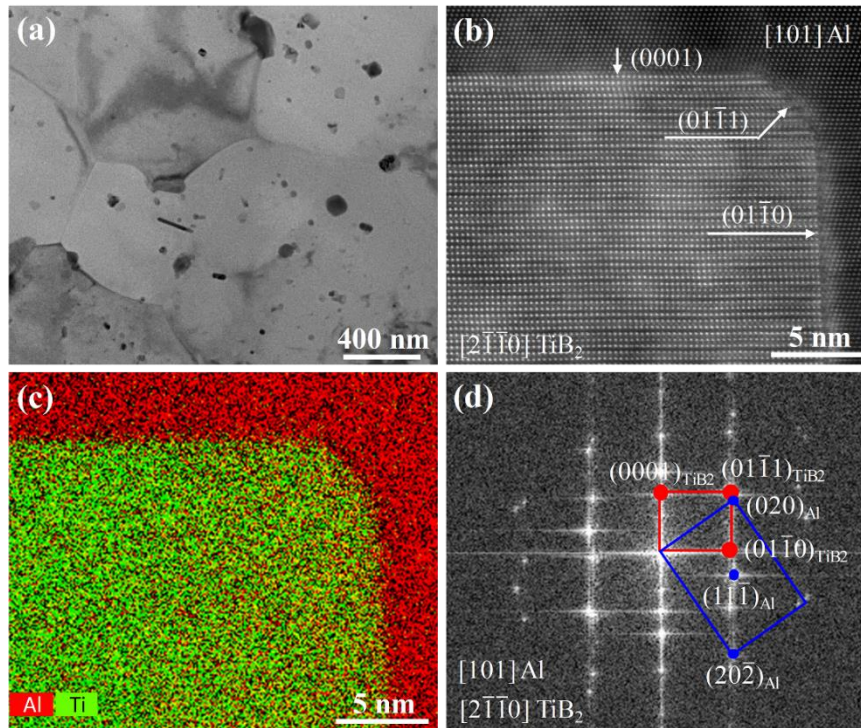


Fig. 5.4 (a) Typical bright-field TEM images of the *in-situ* TiB<sub>2</sub>/Al-Zn-Mg-Cu nanocomposite. (b) Typical HRSTEM-HAADF image of the TiB<sub>2</sub> nanoparticle with the surrounding Al matrix. (c) EDS elemental mapping of (a) showing Ti and Al distributions. (d) Corresponding FFT pattern of (b) showing the ORs between TiB<sub>2</sub> nanoparticles and the Al matrix.

Fig. 5.5a-c shows the HRSTEM-HAADF images of the TiB<sub>2</sub>/Al interfaces parallel to the basal, pyramidal and prismatic facets of TiB<sub>2</sub> nanoparticle, respectively. Periodically spaced misfit dislocations are found situated in the Al matrix close to all three types of TiB<sub>2</sub>/Al interfaces, as highlighted in Fig. 5.5d-f accordingly. For the interfaces parallel to the basal facets of TiB<sub>2</sub> nanoparticles, the projected interplanar distances give a mismatch of 5.87 %, which is in accordance with the measured misfit dislocation spacing 5.8 nm. When it comes to the interfaces parallel to the prismatic and pyramidal facets of TiB<sub>2</sub> nanoparticle, the projected interplanar distances give a much higher mismatch of 38.03 %, which also matches the measured misfit dislocation spacing of 0.95 nm.

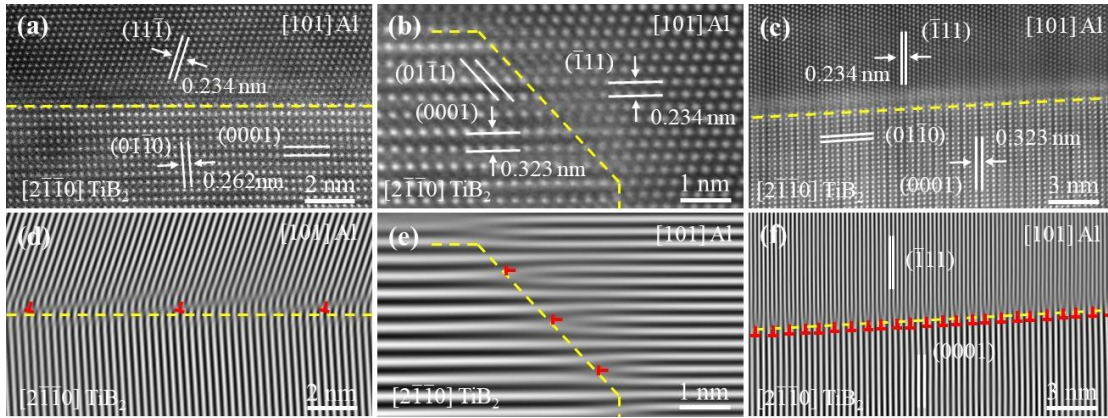


Fig. 5.5 (a-c) HRSTEM-HAADF images and (d-f) the inverse fast Fourier transform (FFT) patterns of TiB<sub>2</sub>/Al interfaces. The projection axis is [101]<sub>Al</sub>//[2 $\bar{1}\bar{1}$ 0]<sub>TiB<sub>2</sub></sub>.

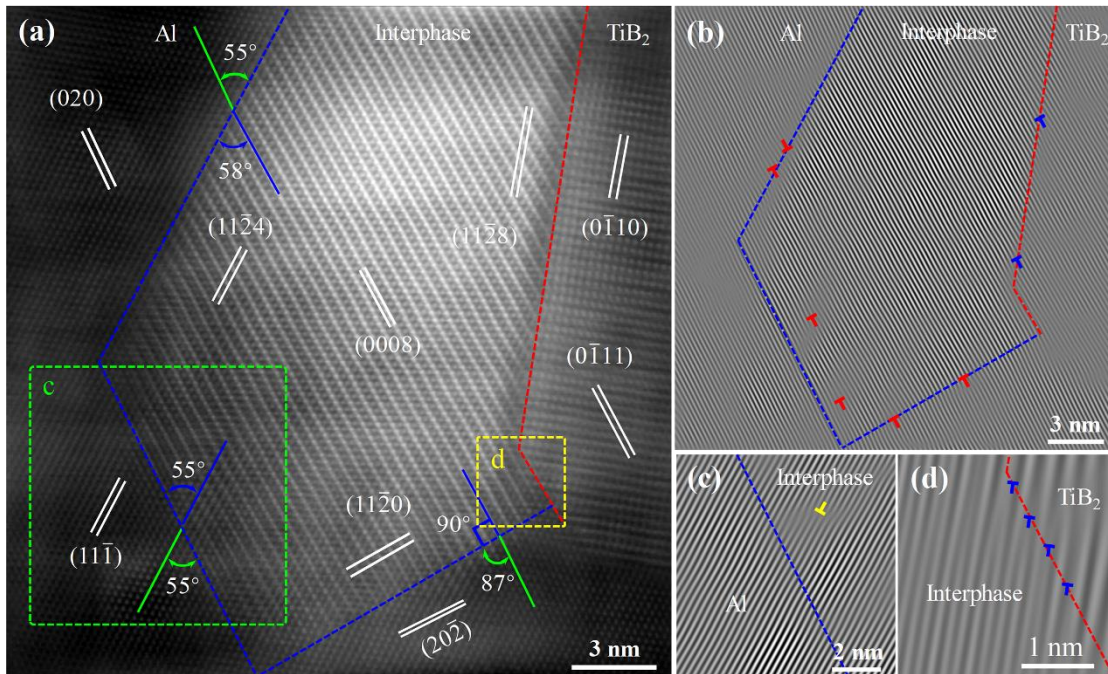


Fig. 5.6 (a) Typical HRSTEM-HAADF image of the Al/(Zn<sub>1.5</sub>Cu<sub>0.5</sub>)Mg interphase/TiB<sub>2</sub> multi-interfaces. (b-d) Corresponding inverse FFT pattern of (a) and zone c and d in (a) to better show the misfit dislocations at the Al/(Zn<sub>1.5</sub>Cu<sub>0.5</sub>)Mg interphase/TiB<sub>2</sub> multi-interfaces. The projection axis is [101]<sub>Al</sub>//[1 $\bar{1}$ 00]<sub>IP</sub>//[2 $\bar{1}\bar{1}$ 0]<sub>TiB<sub>2</sub></sub>.

Fig. 5.6 shows the atomic structure of the Al/(Zn<sub>1.5</sub>Cu<sub>0.5</sub>)Mg interphase/TiB<sub>2</sub> multi-interfaces. The interphase has crystallographic orientation relationships (ORs) with TiB<sub>2</sub> nanoparticles and Al matrix simultaneously. The mismatch of the three kinds of Al/interphase interfaces: (11 $\bar{1}$ )<sub>Al</sub>//(11 $\bar{2}$ 4)<sub>IP</sub>, (020)<sub>Al</sub>//(0008)<sub>IP</sub> and (11 $\bar{2}$ 0)<sub>IP</sub> planes are 0,

0.08% and 3.31%, accordingly. Meanwhile, the mismatch of the two kinds of interphase/TiB<sub>2</sub> interfaces: (11 $\bar{2}$ 8)<sub>IP</sub>//(01 $\bar{1}$ 0)<sub>TiB<sub>2</sub></sub> and (0008)<sub>IP</sub>//(01 $\bar{1}$ 1)<sub>TiB<sub>2</sub></sub> are 2.94% and 60.74%, respectively. The mismatch values of the Al/interphase/TiB<sub>2</sub> multi-interfaces accord with the observed misfit dislocation spacing well. More detail about the (Zn<sub>1.5</sub>Cu<sub>0.5</sub>)Mg interphase can be found in Section 4.3.

## 5.4 Discussion

### 5.4.1 Precipitation assisted interface strengthening

It has been well established that the misfit dislocations at phase interfaces create large coherency strains, which in turn can promote crack initiation under stress [23, 144, 145]. Correspondingly, reducing the mismatch of phase interfaces can be an effective way to strengthen the phase interfaces. At the solid-solution state, the mismatch of the TiB<sub>2</sub>/Al interfaces parallel to the prismatic and pyramidal facets of TiB<sub>2</sub> nanoparticles is 38.03% (Fig. 5.5). During the peak-aging treatment, the (Zn<sub>1.5</sub>Cu<sub>0.5</sub>)Mg interphase precipitated at the TiB<sub>2</sub>/Al interfaces parallel to those two facets of TiB<sub>2</sub> nanoparticles, and formed the Al/(Zn<sub>1.5</sub>Cu<sub>0.5</sub>)Mg interphase/TiB<sub>2</sub> multi-interfaces (Fig. 5.6). Accordingly, the mismatch of the multi-interfaces, i.e., the interfaces (11 $\bar{1}$ )<sub>Al</sub>//(11 $\bar{2}$ 4)<sub>IP</sub>, (020)<sub>Al</sub>//(0008)<sub>IP</sub>, (11 $\bar{2}$ 0)<sub>IP</sub>, (11 $\bar{2}$ 8)<sub>IP</sub>//(01 $\bar{1}$ 0)<sub>TiB<sub>2</sub></sub> and (0008)<sub>IP</sub>//(01 $\bar{1}$ 1)<sub>TiB<sub>2</sub></sub> are 0, 0.08%, 3.31%, 2.94% and 60.74%, respectively. Obviously, except the minor (0008)<sub>IP</sub>//(01 $\bar{1}$ 1)<sub>TiB<sub>2</sub></sub> interfaces, the original high-mismatch (38.03%) TiB<sub>2</sub>/Al interfaces have been transformed into low-mismatch (below 3.31%) Al/(Zn<sub>1.5</sub>Cu<sub>0.5</sub>)Mg interphase/TiB<sub>2</sub> multi-interfaces. The TiB<sub>2</sub>/Al interfaces are thus greatly strengthened by the heterogeneous interface precipitation, which is proposed as precipitation assisted interface strengthening. The schematic illustration indicating this TiB<sub>2</sub>/Al interface evolution during peak-aging treatment is given in Fig. 5.7.

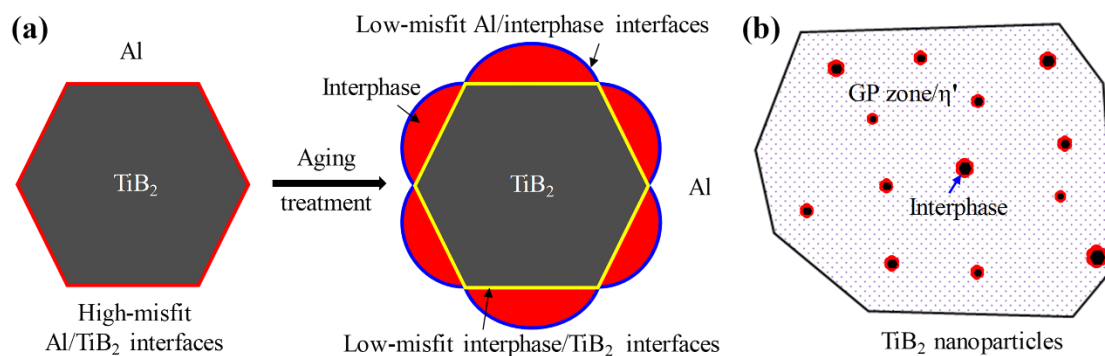


Fig. 5.7 Schematic illustration indicating the (a) TiB<sub>2</sub>/Al interface evolution during aging treatment and (b) overall intragranular precipitation in TiB<sub>2</sub>/Al-Zn-Mg-Cu nanocomposite.

#### 5.4.2 Mechanisms for high strength and ductility

There are mainly three strengthening mechanisms for the enhanced tensile strength in this study: grain refinement strengthening, load-bearing strengthening and Orowan strengthening. According to the Hall-Petch relationship, the smaller grain size the higher grain refinement strengthening [146]. The fine matrix grain size of below 2 μm (Fig. 5.3) of the TiB<sub>2</sub>/Al-Zn-Mg-Cu nanocomposite thus plays an important role on the strengthening. Strong interfacial bonding between the nanoparticles and the matrix is favorable for the effective load-bearing strengthening and in turn, the improved strength of the composite [147]. In this study, the strong bonding of the Al/(Zn<sub>1.5</sub>Cu<sub>0.5</sub>)Mg interphase/TiB<sub>2</sub> multi-interfaces (Fig. 5.6) proves the important contribution of this mechanism. Finally, the origin of the Orowan strengthening is due to the resistance of small hard particles against the motion of dislocations. The dislocation movement starts with passing by the nanosized obstacles by first bowing, followed by reconnecting, and finally forming a dislocation loop around the obstacles. This process leads to the improved strength [148]. The as-processed TiB<sub>2</sub>/Al-Zn-Mg-Cu nanocomposite is featured by the TiB<sub>2</sub> nanoparticles and a large amount of nanoprecipitates homogeneously distributed in the Al alloy matrix. Thus, the Orowan strengthening is highly effective in this case (Fig. 5.8).

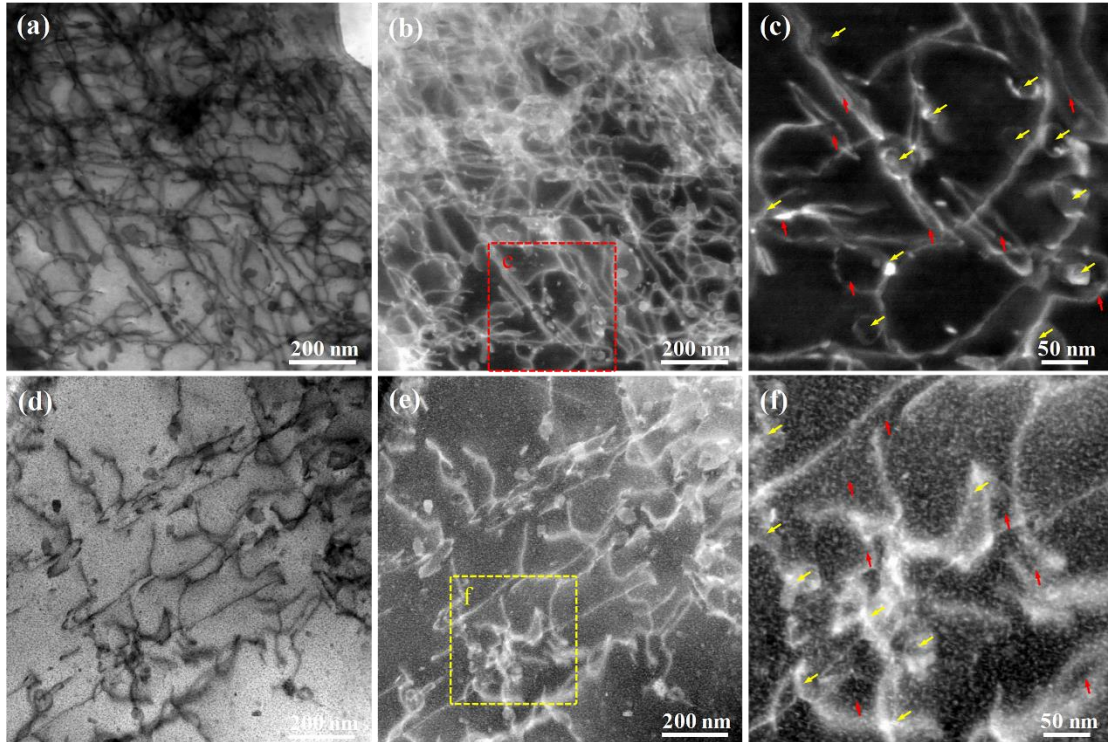


Fig. 5.8 (a) Bright-field and (b) dark-field STEM image of water-quenched  $\text{TiB}_2/\text{Al-Zn-Mg-Cu}$  nanocomposite at 1.5% strain. (c) Higher magnification image of zone c in (b). (d) Bright-field and (e) dark-field STEM image of peak-aged  $\text{TiB}_2/\text{Al-Zn-Mg-Cu}$  nanocomposite at 1.5% strain. (f) Higher magnification image of zone f in (b). The yellow and red arrows mark the  $\text{TiB}_2$  nanoparticles and dislocation loops generated by dislocation/ $\text{TiB}_2$  interaction, respectively.

During the plastic deformation of the  $\text{TiB}_2/\text{Al-Zn-Mg-Cu}$  nanocomposite, the uniformly distributed  $\text{TiB}_2$  nanoparticles can effectively block/store dislocations (Fig. 5.8). When the dislocations bypass those  $\text{TiB}_2$  nanoparticles, dislocation loops are generated and introduced into the Al matrix (Fig. 5.8c and 5.8f). These two effects lead to a high work-hardening rate that can delay localized deformation (necking) under tensile stress, which is essential for the good uniform elongation [23, 149, 150].

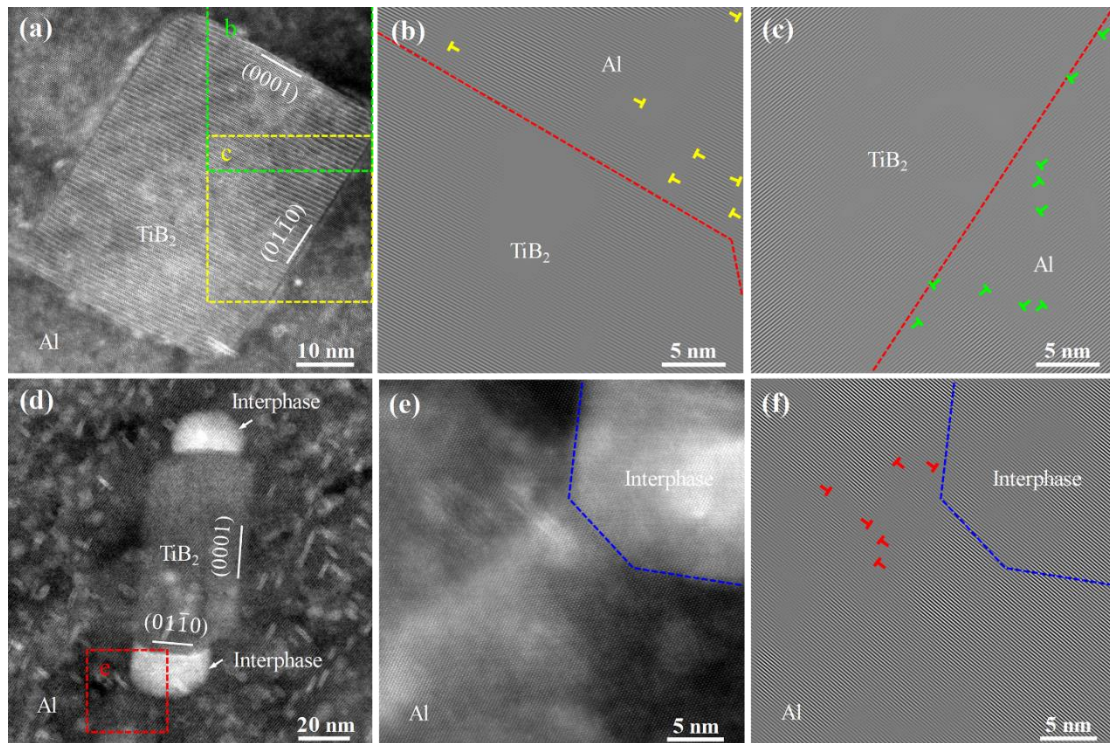


Fig. 5.9 (a) HRSTEM-HAADF image and (b) and (c) corresponding inverse FFT patterns of (a) of TiB<sub>2</sub> nanoparticle and the surrounding Al matrix at water-quenched state at 1.5% strain. (d) STEM-HAADF image, (e) STEM-HAADF image and (f) corresponding inverse FFT patterns of (e) of TiB<sub>2</sub> nanoparticle and the surrounding Al matrix at peak-aged state at 1.5% strain.

If the PAIS does not occur at the TiB<sub>2</sub>/Al interfaces, the high density of dislocations shall directly accumulate at the high-mismatch TiB<sub>2</sub>/Al interfaces (Fig. 5.9a-c). Along with the plastic deformation continue, an increasing number of dislocations shall be trapped and accumulate at the TiB<sub>2</sub>/Al interfaces. When the stress at the interfaces reaches the threshold that the interfaces can bear, the interfacial debonding occurs, and the localized deformation (necking) takes place subsequently [23, 24]. When it comes to the TiB<sub>2</sub>/Al interfaces with PAIS (i.e., the Al/(Zn<sub>1.5</sub>Cu<sub>0.5</sub>)Mg interphase/TiB<sub>2</sub> multi-interfaces), the high density of dislocations shall accumulate at the low-mismatch Al/interphase interfaces (Fig. 5.9 d-f) because they are not able to cut through the (Zn<sub>1.5</sub>Cu<sub>0.5</sub>)Mg interphase. Considering the interface strength of the low-mismatch Al/interphase interfaces is much higher than that of the high-mismatch TiB<sub>2</sub>/Al

interfaces, the threshold of the stress that the low- mismatch Al/interphase interfaces can bear should be much higher than that of the high- mismatch  $\text{TiB}_2/\text{Al}$  interfaces. That is to say, compared to the high- mismatch  $\text{TiB}_2/\text{Al}$  interfaces, the low- mismatch Al/interphase interfaces can block/store more dislocations and introduce a higher density of dislocations into the Al matrix before the interface debonding occurs. The Al/interphase interfaces thus can lead to a higher work-hardening rate and delay localized deformation for a larger plastic deformation. Consequently, the uniform deformation of the  $\text{TiB}_2/\text{Al-Zn-Mg-Cu}$  nanocomposite is greatly improved. The schematic illustration indicating this process is shown in Fig. 5.10.

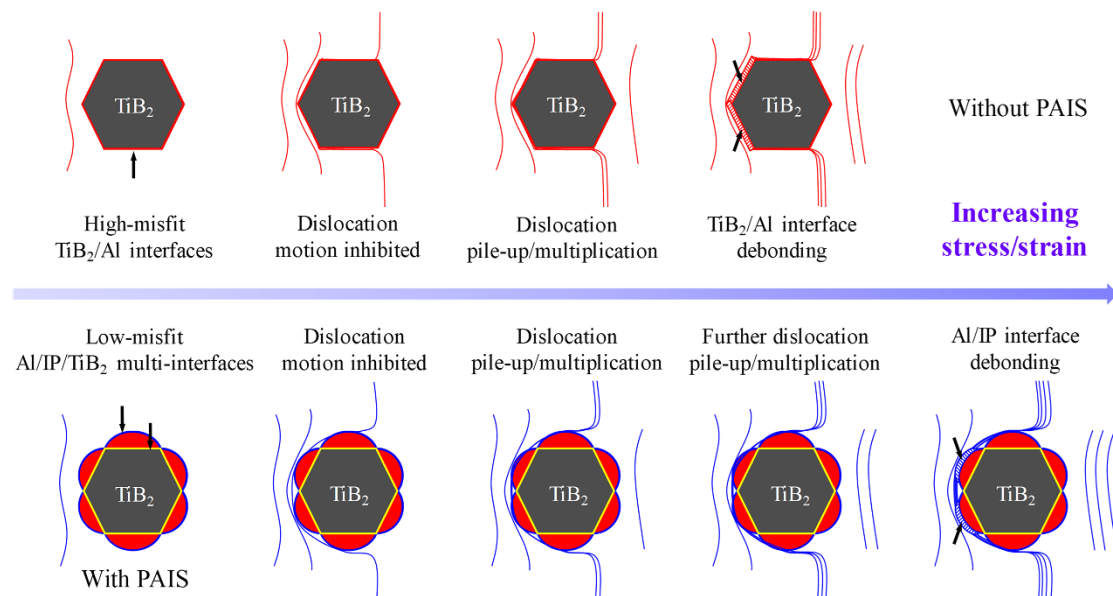


Fig. 5.10 Schematic illustration indicating the  $\text{TiB}_2$ /dislocation interaction with and without PAIS during plastic deformation.

## 5.5 Conclusion

In this work we have proposed a new strategy for the design of Al-based MMCs with simultaneously increased tensile strength and ductility based on the concept of precipitation-assisted interface strengthening mechanism. As a model material, we designed, produced and examined an Al-Zn-Mg-Cu alloy matrix composite reinforced with 6wt. % uniformly distributed  $\text{TiB}_2$  nanoparticles. During the peak-aging treatment,

the high-mismatch  $\text{TiB}_2/\text{Al}$  interfaces with high coherency strains at solid-solution state were transformed into low-mismatch  $\text{Al}/(\text{Zn}_{1.5}\text{Cu}_{0.5})\text{Mg}$  interphase/ $\text{TiB}_2$  multi-interfaces with very low coherency strains. As such, the original  $\text{TiB}_2/\text{Al}$  interfaces were greatly strengthened by the heterogeneous interfacial precipitation. The combined effects of  $\text{TiB}_2/\text{dislocation}$  interaction and the precipitation assisted interface strengthening have contributed to the simultaneously increased tensile strength (yield strength of 600 MPa) and ductility (uniform elongation of 12%) of the  $\text{TiB}_2/\text{Al-Zn-Mg-Cu}$  nanocomposite. Theoretically, our strategy is applicable to all of the NRPs reinforced age-hardenable Al matrix composites, paving a cost-effective and scalable way for their large-scale industrial applications.

# Chapter 6 Study of the Mechanisms of Nanoparticles Influencing Fatigue Crack Growth in TiB<sub>2</sub>/Al-Zn-Mg-Cu Composite

*Published. Y. Ma, J. Geng, Z. Chen, M. Wang, D. Chen, G. Ji, V. Ji, H. Wang. Engineering Fracture Mechanics. Vol. 207, 2019, 23-35*

To investigate the mechanisms of nanoparticles influencing the fatigue crack growth (FCG) of metal matrix composites, an *in-situ* TiB<sub>2</sub>/7050Al composite was systematically investigated. The nanoscale TiB<sub>2</sub> showed a morphology of particle bands coexisting with grain boundaries (GBs) along extrusion direction. The TiB<sub>2</sub>/7050Al composite presented a finer grain size compared to the 7050Al alloy. The TiB<sub>2</sub>/7050Al composite exhibited a lower, the similar and a higher FCG rate over the 7050Al alloy at the low, intermediate and high stress intensity factor ( $\Delta K$ ) range, accordingly. The microstructure and  $\Delta K$  correlated FCG mechanisms of TiB<sub>2</sub>/7050Al composite were discussed in detail. Inside grains, caused by the finer grain size and the increasing  $\Delta K$ , the TiB<sub>2</sub>/7050Al composite exhibited the similar FCG rate compared to 7050Al alloy at low  $\Delta K$  range, while showed a higher FCG rate at intermediate and high  $\Delta K$  range. At GBs, along with the increasing  $\Delta K$ , the TiB<sub>2</sub> bands induced fatigue crack deflection, fatigue crack trapping and microvoid coalescence led to the lower FCG rate of TiB<sub>2</sub>/7050Al composite at low and intermediate  $\Delta K$  range and the higher FCG rate at high  $\Delta K$  range, accordingly.

## 6.1 Introduction

The addition of reinforcements to matrix alloys leads to the increased modulus [151], wear resistance [152, 153] and fatigue crack initiation resistance [41, 154], that can also be accompanied by the enhanced yield strength [29, 155] and improved high

temperature property [156, 157] depending on the alloy, manufacturing methods and the subsequent processing treatments when compared to the alloy counterparts. These excellent properties make the particle reinforced metal matrix composites (MMCs) well suitable for the application in aerospace and automotive industries, where the dynamic cyclic loading is inevitably involved. Therefore, considering the great significance, the effects of reinforcements exerted on the fatigue crack growth (FCG) of MMCs have been discussed by numerous studies [25-27, 158-164].

Compared to unreinforced matrix alloys, the effect of micron-scale reinforcements on the FCG resistance of MMCs depends on the stress intensity factor ( $\Delta K$ ) range. The FCG resistance is improved at low  $\Delta K$  range but deteriorated at intermediate and high  $\Delta K$  range [25-27]. At low  $\Delta K$  range, the FCG resistance is improved owing to the roughness-induced crack closure [27, 165]. In detail, the FCG is impeded by the particles via promoting the crack deflection, which results in the enhanced fatigue fracture surface roughness and the resultant roughness-induced crack closure [26, 158, 159]. Meanwhile, the deteriorated FCG resistance at the intermediate and high  $\Delta K$  regions have been ascribed to the severely enhanced particle fracture or particle/matrix debonding in the cyclic plastic zone ahead of the fatigue crack tip, which is termed as monotonic fracture mode [25, 27, 159, 160]. In addition, lots of studies found that the particle size [141, 166-168] and particle distribution [160, 161, 169] also exert great influences on the FCG. The point of view is divided on the influences of the particle size exerted on the FCG of MMCs. Some of them indicated the FCG rate tended to decrease along with increased particle size [170], while the others proposed that increased particle size improved the FCG resistance [141]. On the other hand, Kumai *et al.* [161] proposed that the FCG resistance can be improved using inhomogeneous particle distribution.

In recent years, along with the development of *in-situ* processing technique, the *in-situ* particles reinforced MMCs have become increasingly attractive because of their superior microstructure compared to the *ex-situ* counterparts, such as the nanoscale

particle size, relatively round particle shape and cleaner particle/matrix interface [75, 83, 100, 171-175]. These different micrographic characteristics of the *in-situ* particles should exert different influences to the FCG of MMCs compared to the micron-scale reinforcements. Therefore, corresponding studies were carried out to investigate the FCG of *in-situ* MMCs. Some studies [176, 177] indicated the *in-situ* MMCs showed a slight higher FCG rate compared to the matrix alloy during the whole FCG process. Meanwhile, some studies [80] proposed nanoscale reinforcements have significant retardation on FCG if their sizes are smaller than 500 nm. Nevertheless, studies on the FCG of *in-situ* MMCs, especially the age hardening and extruded ones, are very limited. The corresponding mechanisms of FCG of *in-situ* MMCs still remained unclear.

To solve this problem, we conducted FCG experiments in an *in-situ* TiB<sub>2</sub>/7050Al composite. The 7050Al alloys have been widely used as structural materials in aeronautical and automobile industries due to their attractive comprehensive properties [1, 178]. Meanwhile, titanium diboride (TiB<sub>2</sub>) is well known as a ceramic material with relatively high strength and durability as characterized by the relatively high values of its melting point, hardness, strength to density ratio, and wear resistance [40, 179]. TiB<sub>2</sub> exhibits hexagonal symmetry with space group P6/mmm. The lattice parameters are as follows:  $a = b \neq c$ ,  $\alpha = \beta = 90^\circ$ ,  $\gamma = 120^\circ$ , 1 formula unit per cell, Ti at (0,0,0), B at (1/3,2/3,1/2) and (2/3,1/3,1/2) [72, 73]. In addition, the TiB<sub>2</sub>/7050Al composite can be fabricated by the *in-situ* mixed salt method conveniently and economically [41, 42]. Moreover, the high cycle fatigue behavior of *in-situ* TiB<sub>2</sub>/7050 composite and the unreinforced 7050Al alloy have been investigated in our previous studies [41]. The fatigue limit of the composite is 390 MPa, which is much higher than the unreinforced alloy (305MPa). Therefore, the *in-situ* TiB<sub>2</sub>/7050Al composite is an ideal material for this study. The present study aims to provide the basis for understanding the mechanisms of nanoscale reinforcements influencing the FCG of MMCs.

## 6.2 Experimental procedure

## 6.2.1 Materials processing and heat treatment

The *in-situ* 6wt.% TiB<sub>2</sub>/7050Al (Al-6.5Zn-2.3Mg-2.3Cu, in wt. %) ingot was fabricated by the salt-metal reaction method [41]. The as-cast ingot was homogenized at 470 °C for 24 h, and then was extruded at 420 °C with an extrusion ratio of 10:1. Afterwards, the composite was subjected to T6 treatment. The solution treatment was performed at 477 °C for 70 min, subsequently followed by water quenching. The peak-aging was performed at 120 °C for 24 h. As the reference sample, the 7050 Al alloy was extruded and heat treated using the same methods with the composite.

## 6.2.2 Sample preparation and fatigue crack growth testing

After T6 treatment, the extruded rods were cut by linear cutting to obtain plates, as is shown by the schematic diagram in Fig. 6.1a. Those plates were then machined into compact tension (CT) specimens for FCG testing according to the ASTM E647-2013a standard with a size of 45×43.2×6 (in mm) [92]. The detailed dimensions of the specimens are shown in Fig. 6.1b. After the mechanical processing, all of the specimens were subjected to mechanical polishing to minimize the effect of machining defects, such as surface damage or subsurface alternation. The notch and the pre-crack (~2 mm in length) were perpendicular to extrusion direction (ED).

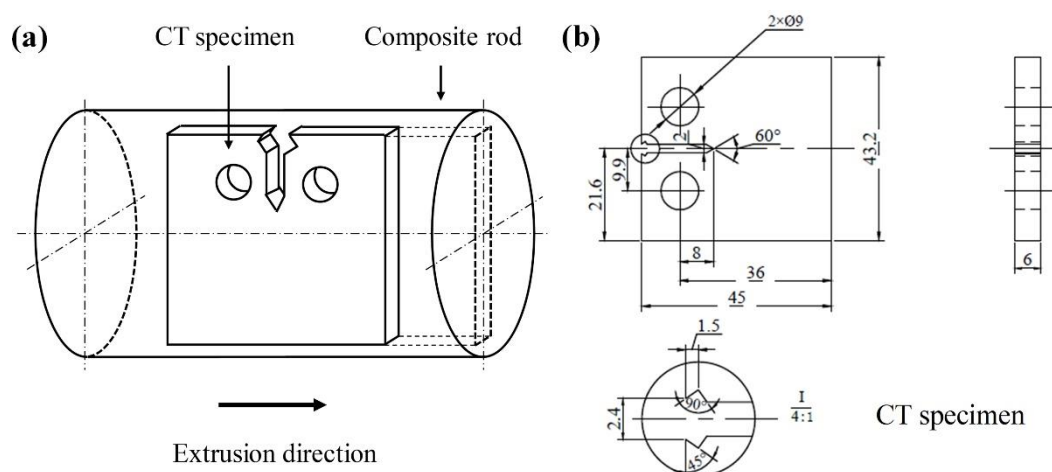


Fig. 6.1 (a) Schematic diagram and (b) dimensions of the CT specimens for the FCG rate testing.

The tensile tests were conducted on a zwick/Roell Z100 instrument at a strain rate of  $5.6 \times 10^{-4} \text{ s}^{-1}$  at room temperature. The tensile properties of the TiB<sub>2</sub>/7050Al composite and the unreinforced alloy at T6 state are presented in Table 6.1. The FCG testing was conducted on the MTS 809 servohydraulic testing machine at room temperature and laboratory air environment. A sinusoidal cyclic constant loading with a stress ratio ( $R = \sigma_{\min} / \sigma_{\max}$ ) of 0.1 and a frequency of 10 Hz were applied. The MTS computer system was employed to control and detect the FCG rates during the FCG testing. The crack growth was measured by the crack tip open displace (CTOD) method on the MTS 809 servo hydraulic testing machine. According to ASTM E647-13a [92], the test specimens were tested at a constant force ( $P$ ) range. So, as the crack length increasing,  $K$  was increasing during the test procedure. For the C(T) specimen,  $\Delta K$  is calculated as follows:

$$\Delta K = \frac{\Delta P}{B\sqrt{W}} \frac{2 + \alpha}{(1 - \alpha)^{\frac{3}{2}}} (0.886 + 4.64\alpha - 13.32\alpha^2 + 14.72\alpha^3 - 5.6\alpha^4)$$

where  $\alpha = a/W$ ,  $\Delta P = P_{\max} - P_{\min}$ ,  $a$  is the crack length,  $B$  and  $W$  are the dimensions of specimens.

Table 6.1 Tensile properties with standard deviations of 7050Al alloy and 6 wt.% TiB<sub>2</sub>/7050Al composite at T6 state.

| Material                           | Yield strength (MPa) | Ultimate strength (MPa) | Elongation (%) |
|------------------------------------|----------------------|-------------------------|----------------|
| 7050Al alloy                       | 665 ± 6.1            | 717 ± 3.2               | 11.2 ± 0.5     |
| TiB <sub>2</sub> /7050Al composite | 687 ± 16.5           | 735 ± 11.6              | 6.8 ± 0.4      |

### 6.2.3 Microstructure characterization

The microstructural morphology and fracture surface were observed by scanning electron microscopy (SEM, JSM-7800F) equipped with energy dispersive spectroscopy (EDS). Based on the equivalent area of the individual particle, the particle size meant the equivalent diameter of TiB<sub>2</sub> particle assuming its round morphology. The TiB<sub>2</sub> particle size distribution was derived by analyzing the SEM images using Image-Pro

Plus software. The total number of the analyzed  $\text{TiB}_2$  particles is 343. The bright field (BF) micrographs of the composite were characterized via transmission electron microscopy (TEM). A state-of-the-art FEI Titan Themis 300 TEM equipped with a high angle annular dark field (HAADF) detector and probe aberration corrector was used to further acquire the high-resolution scanning TEM (HRSTEM) image of the  $\text{TiB}_2/\text{Al}$  interface. The thin foils for TEM observation were prepared by twin jet-polishing, using a nitric/methanol solution (1:4 in volume) at  $-25\text{ }^\circ\text{C}$  followed by ion milling. Perpendicular to ED, the electron backscatter diffraction (EBSD) was conducted on NOVA NanoSEM 230 with a step size of  $0.2\text{ }\mu\text{m}$ . The obtained micrographs were analyzed using the Channel 5 software to achieve the grain size distributions and average grain sizes of both the alloy and the composite. The misorientation larger than  $15^\circ$  was defined as high angle grain boundaries (GBs), while that in  $2^\circ$ - $15^\circ$  was defined as low angle GBs.

## 6.3 Results

### 6.3.1 Microstructure

Fig. 6.2a shows the typical microstructure of the *in-situ*  $\text{TiB}_2/7050\text{Al}$  composite perpendicular to ED. Most of the  $\text{TiB}_2$  particles are agglomerated at GBs presenting a morphology of particle clusters. Surrounded by  $\text{TiB}_2$  clusters, secondary phases are observed, as marked by the blue arrows. The higher magnification image of the  $\text{TiB}_2$  clusters is given in Fig. 6.2b, which presents  $\text{TiB}_2$  particles with near-spherical shape. Fig. 6.2c shows the representative microstructure of the  $\text{TiB}_2/7050\text{Al}$  composite along ED.  $\text{TiB}_2$  particles are aligned along ED, presenting a morphology of  $\text{TiB}_2$  bands with the width range  $\sim 5$ - $15\text{ }\mu\text{m}$ . Only a few  $\text{TiB}_2$  particles are found in the interband zone, which is regarded as the  $\text{TiB}_2$  lean zone. Secondary phases (marked by blue arrows) are also found to be inclined to coexist with the  $\text{TiB}_2$  bands. A few secondary phases (marked by red arrows) are found located at the  $\text{TiB}_2$  lean zones. Notably, the secondary phases coexisting with  $\text{TiB}_2$  bands present much larger size than the ones located at

TiB<sub>2</sub> lean zones. The higher magnification image of TiB<sub>2</sub> bands is presented in Fig. 6.2d, showing a much higher density of TiB<sub>2</sub> particles.

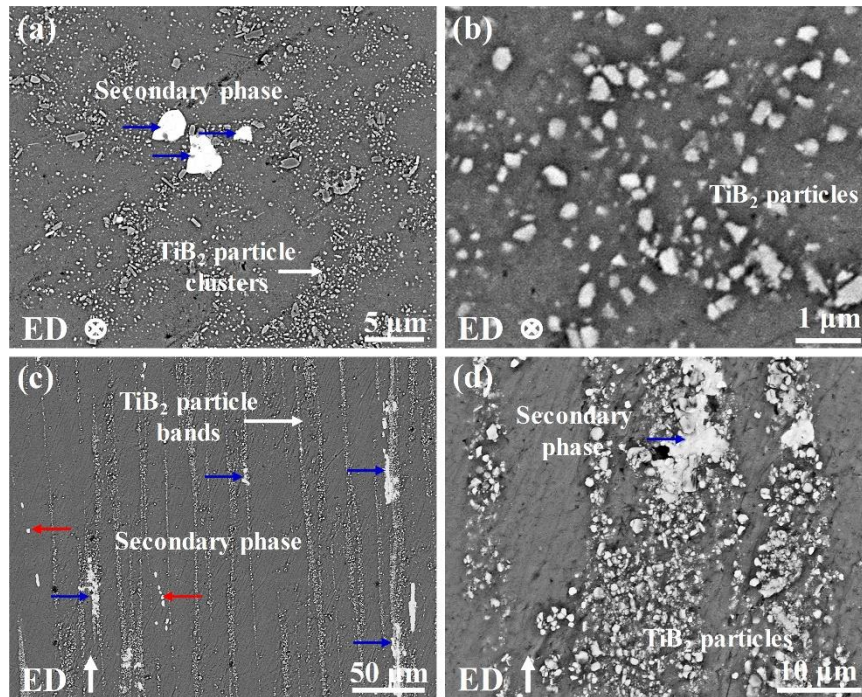


Fig. 6.2 Typical morphology of TiB<sub>2</sub>/7050Al composite. (a) Morphology perpendicular to ED; (b) higher magnification image of the TiB<sub>2</sub> clusters in (a); (c) morphology along ED; (d) higher magnification image of the TiB<sub>2</sub> bands in (c).

The typical BF image of TiB<sub>2</sub>/7050Al composite is shown in Fig. 6.3a. In accordance with the SEM results, the majority of the TiB<sub>2</sub> particles are agglomerated at GBs (marked by white dotted lines) as marked by red arrows. Only one TiB<sub>2</sub> particle (marked by yellow arrow) is observed inside grains. Fig. 6.3b illustrates the size distribution of TiB<sub>2</sub> particles in the TiB<sub>2</sub>/7050Al composite. The size of the TiB<sub>2</sub> particles ranges from 15 nm to 350 nm. The number of the particles decreases sharply with the increased particle size. Notably, the majority of the TiB<sub>2</sub> particles are 15-100 nm in size. The average size of the TiB<sub>2</sub> particles is measured to be 43 nm. According to the representative HRSTEM HAADF image (Fig. 6.3c) and the corresponding fast Fourier transform (FFT) pattern (Fig. 6.3d) of the TiB<sub>2</sub>/Al interface, the TiB<sub>2</sub> nanoparticle and Al matrix have clean and highly coherent interface with preferential orientation relations (ORs), i.e.  $[101]_{Al} // [2 \bar{1}\bar{1}0]_{TiB_2}$ ,  $(11 \bar{1})_{Al} // (0001)_{TiB_2}$  and

$(020)_{Al} // (0\bar{1}11)_{TiB_2}$  being determined, which are agree with the previously reported ORs between  $TiB_2$  particles and Al matrix [79, 80, 85].

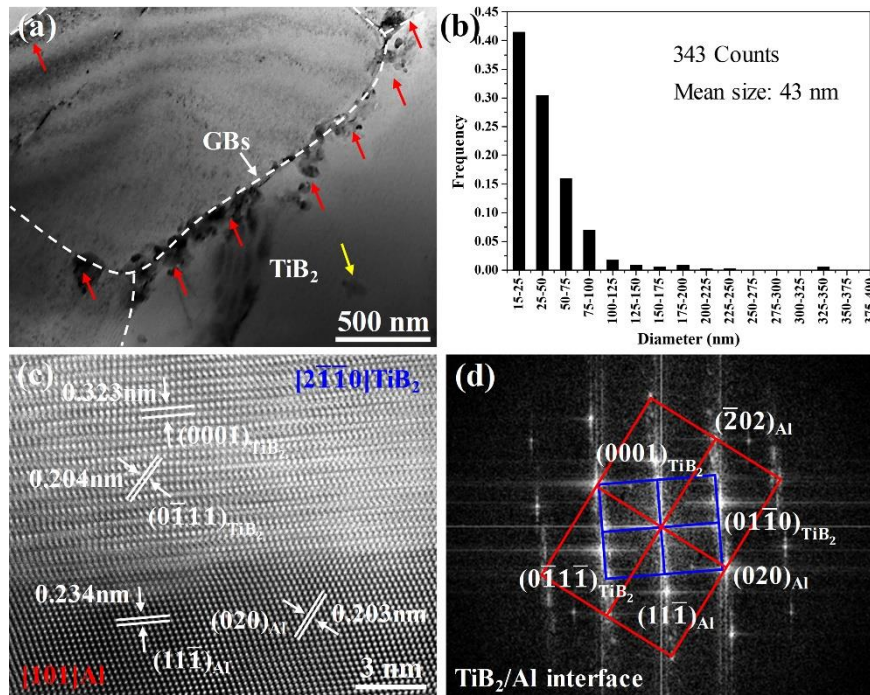


Fig. 6.3 (a) Typical BF image of  $TiB_2/7050Al$  composite; (b)  $TiB_2$  particle size distribution based on SEM images; (c) representative HRSTEM HAADF image of the  $TiB_2/Al$  interface acquired along  $[101]_{Al} // [2\bar{1}\bar{1}0]_{TiB_2}$  projection; (d) corresponding FFT pattern of the  $TiB_2/Al$  interface in (c) showing the relative orientation relations.

Fig. 6.4 presents the EDS analyses of the main constituent elements of Fig. 6.2a. According to the results of EDS mapping (Fig. 6.4a-e) and EDS spectrum (Fig. 6.4f), the secondary phase is enriched with Al, Cu and Mg with the content ratio of 2:1:1. Generally, the 7050 Al alloy include  $\eta$  phase ( $MgZn_2$ ), S phase ( $Al_2CuMg$ ) and T phase ( $Al_2Mg_3Zn_3$ ) [180]. Combining this with the element content ratio, we can reasonably infer that the secondary phase is  $Al_2CuMg$  phase. Generally, the amount and size of the S phases coexist with  $TiB_2$  bands are much larger than the ones located at  $TiB_2$  lean zones. Our previous study [181] has shown that the  $TiB_2$  particles aggregated around secondary phases can act as particle shells to reduce the effective contact area between Al matrix and secondary phases, which can hinder the dissolution of secondary phases in  $TiB_2/Al$  alloy composite. This phenomenon results in the different characteristics of

the S phases situated inside grains and coexisting with TiB<sub>2</sub> bands.

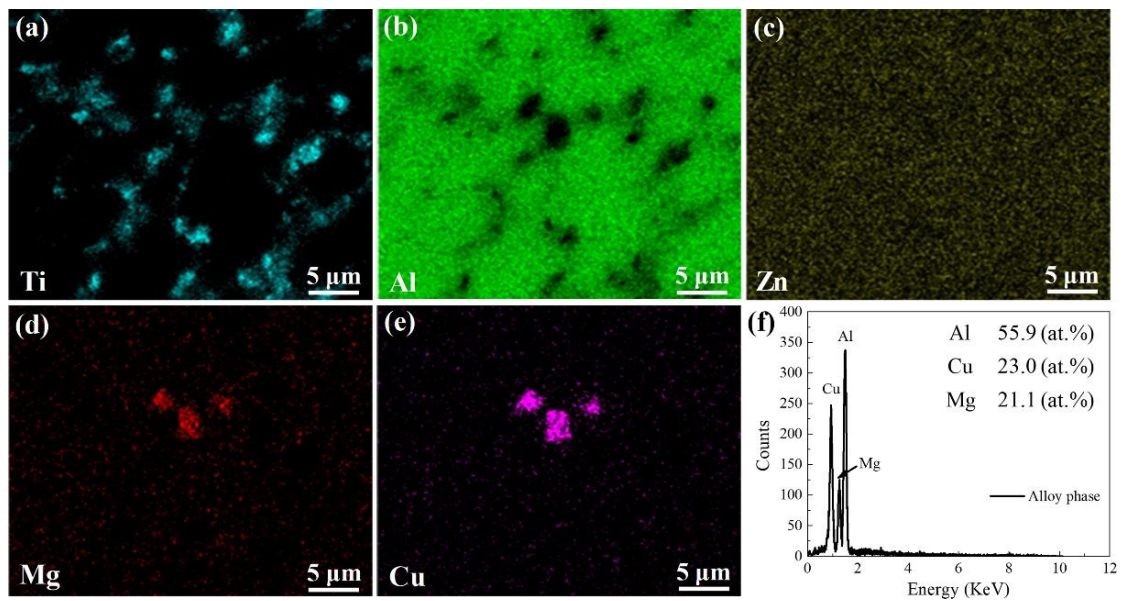


Fig. 6.4 (a)-(e) EDS mapping of the main constituent elements (Ti, Al, Zn, Mg and Cu) of Fig. 6.2a; (f) EDS spectrum of the secondary phase.

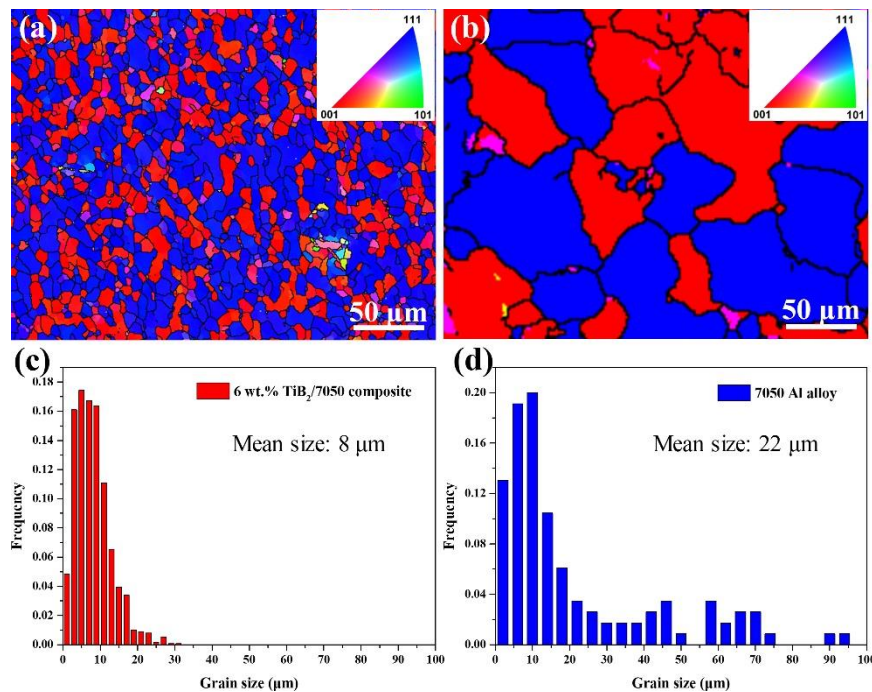


Fig. 6.5 EBSD maps of the cross-section of (a) TiB<sub>2</sub>/7050Al composite; (b) 7050Al alloy. The color code representing the crystal orientation is included. Grain size distributions of the cross-section of (c) TiB<sub>2</sub>/7050Al composite; (d) 7050Al alloy.

The EBSD analyses of TiB<sub>2</sub>/7050Al composite and 7050Al alloy are shown in Fig.

6.5. It is found that both the alloy and the composite have the similar fiber textures. However, the grain size exhibits significant difference. The grain size of the TiB<sub>2</sub>/7050Al composite ranges from 1 μm to 38 μm, including 2.6 % of them having a size larger than 20 μm. The average grain size of the TiB<sub>2</sub>/7050Al composite is measured to be 8 μm. For the 7050Al alloy, it has a wider grain size distribution that ranges from 3 μm to 95 μm, with 31.3 % of the grains have the size larger than 20 μm. The average grain size of the 7050Al alloy is 22 μm. Obviously, the average grain size of TiB<sub>2</sub>/7050Al composite is much finer than the 7050Al alloy.

### 6.3.2 Fatigue crack growth rate

The FCG rates ( $da/dN$ ) versus stress intensity factor range ( $\Delta K$ ) curves of the *in-situ* TiB<sub>2</sub>/7050Al composite and 7050Al alloy are shown in Fig. 6.6a. To better show the FCG behavior at low  $\Delta K$  range, the  $da/dN$  versus  $\Delta K$  curves and the corresponding exponential fit curves at Stage I are provided in Fig. 6.6b. The results including:

- Stage I (Low  $\Delta K$  range,  $6.5 < \Delta K < 9.5 \text{ MPa}\cdot\text{m}^{1/2}$ ): TiB<sub>2</sub>/7050Al composite presents a lower FCG rate than 7050Al alloy.
- Stage II (Intermediate  $\Delta K$  range,  $9.5 \text{ MPa}\cdot\text{m}^{1/2} \leq \Delta K \leq 21 \text{ MPa}\cdot\text{m}^{1/2}$ ): TiB<sub>2</sub>/7050Al composite shows the similar FCG rate to 7050Al alloy.
- Stage III (High  $\Delta K$  range,  $\Delta K > 21 \text{ MPa}\cdot\text{m}^{1/2}$ ): TiB<sub>2</sub>/7050Al composite exhibits a higher FCG rate than 7050Al alloy.

In addition, the  $da/dN$  versus  $\Delta K$  curves of both 7050Al alloy and TiB<sub>2</sub>/7050Al composite show linear dependences in the logarithmic coordinate system, which are accorded with the Paris law [182] expressed by:

$$\frac{da}{dN} = C\Delta K^m \quad (6.1)$$

where  $C$  and  $m$  are the constants of the materials.

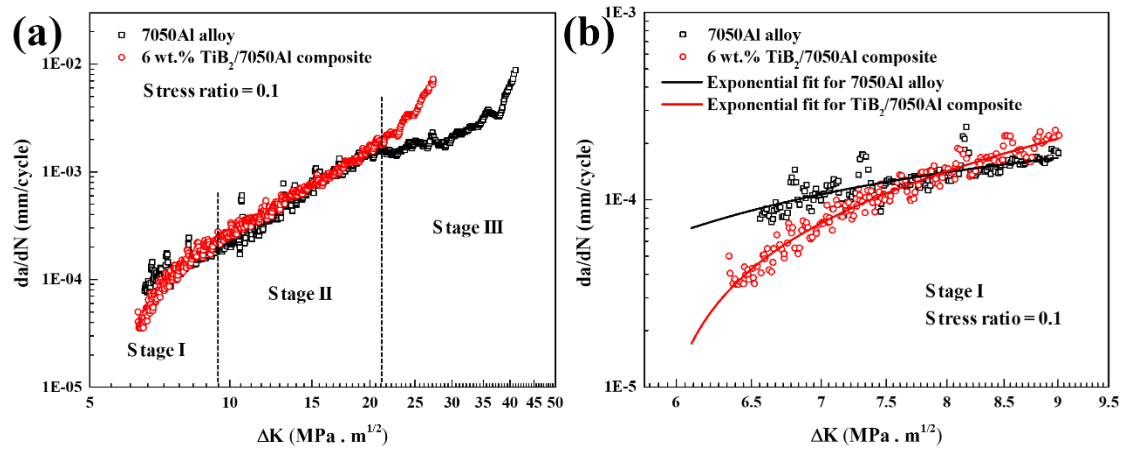


Fig. 6.6 (a) The overall  $da/dN$  versus  $\Delta K$  curves of the peak-aged  $TiB_2/7050Al$  composite and 7050Al alloy. (b) The  $da/dN$  versus  $\Delta K$  curves and the corresponding exponential fit curves of the peak-aged  $TiB_2/7050Al$  composite and 7050Al alloy at Stage I to better show the FCG behavior at low  $\Delta K$  range. The stress ratio is 0.1.

From Fig. 6.6, the parameters  $C$  and  $m$  of 7050Al alloy and  $TiB_2/7050Al$  composite at intermediate  $\Delta K$  range were determined by linear fitting as  $4.48 \times 10^{-7}$  and 2.71,  $5.57 \times 10^{-7}$  and 2.67, accordingly. Therefore, there is little difference in the values of parameters  $C$  and  $m$  between 7050Al alloy and  $TiB_2/7050Al$  composite.

### 6.3.3 Fractographic features of crack propagation

Fig. 6.7a shows the fractographic features of the FCG of 7050Al alloy at low  $\Delta K$  range. The surface is trans-granular and relatively featureless, with predominant cleavage river patterns being found. The fractographic feature of the FCG of  $TiB_2/7050Al$  composite at low  $\Delta K$  range is presented in Fig. 6.7b. Typical cleavage river patterns and protrusion zones (marked by red arrows) are observed. The distribution of the protrusion zones is in accordance with the distribution of  $TiB_2$  clusters. The higher magnification image of the cleavage river zones in Fig. 6.7b is shown in Fig. 6.7c, with no obvious striations being found. The higher magnification image of the protrusion zones in Fig. 6.7b is presented in Fig. 6.7d. Fractured S phase and several  $TiB_2$  particles are observed, as marked by white and yellow arrows, respectively.

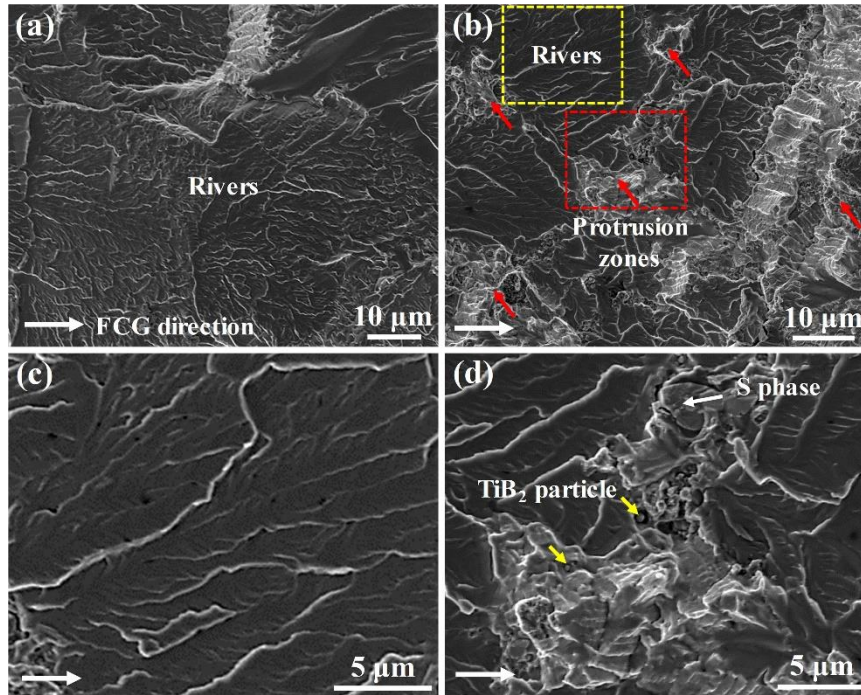


Fig. 6.7 Fractographic features of the FCG at low  $\Delta K$  range. (a) 7050Al alloy; (b)  $\text{TiB}_2/7050\text{Al}$  composite. Higher magnification image of (c) the river zones marked with yellow square in (b); (d) the protrusion zones marked with red square in (b).

Fig. 6.8a shows the fractographic features of the FCG of 7050Al alloy at intermediate  $\Delta K$  range, with predominant cleavage river patterns being found. The fractographic feature of the FCG of  $\text{TiB}_2/7050\text{Al}$  composite at intermediate  $\Delta K$  range is given in Fig. 6.8b. Typical cleavage river patterns and  $\text{TiB}_2$  cluster zones (marked by red arrows) are observed in the fractographic features. Fractured S phase are observed in  $\text{TiB}_2$  cluster zones. Still, no obvious striations are found (Fig. 6.8c). The higher magnification image of the  $\text{TiB}_2$  cluster zones in Fig. 6.8b is presented in Fig. 6.8d. A high density of  $\text{TiB}_2$  particles are found in the  $\text{TiB}_2$  cluster zones. Notably, no obvious tear ridges or deep dimples are observed around the  $\text{TiB}_2$  particles.

Fig. 6.9a shows the fractographic feature of the FCG of 7050Al alloy at high  $\Delta K$  range. The alternatively distributed cleavage river patterns and striations are found, with the striation spacing of  $\sim 0.86 \mu\text{m}$ . The fractographic features of the FCG of  $\text{TiB}_2/7050\text{Al}$  composite at high  $\Delta K$  range is presented in Fig. 6.9b. The fractographic features are composed by alternatively distributed striations and dimple zones, with the

width of the striations  $\sim 1.16 \mu\text{m}$ . Fig. 6.9c shows the higher magnification image of the S phase, which is fractured and surrounded by a high density of dimples. The higher magnification image of the dimple zones is given in Fig. 6.9d. A high density of tear ridges and interconnected deep dimples are found in the dimple zones.  $\text{TiB}_2$  particles are observed inside the dimple pockets, as marked by the yellow arrows.

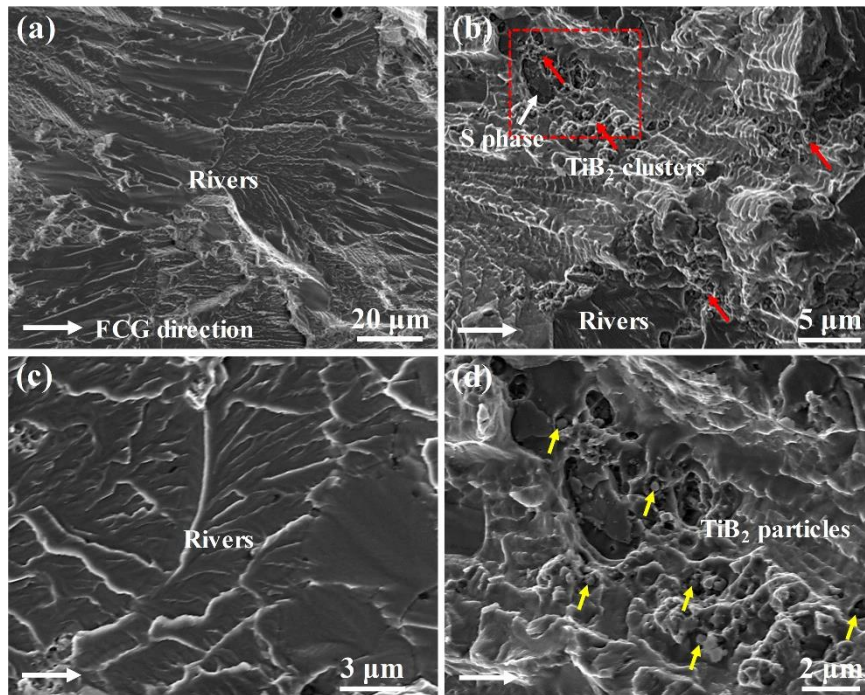


Fig. 6.8 (a) Fractographic features of the FCG at intermediate  $\Delta K$  range. (a) 7050Al alloy; (b)  $\text{TiB}_2/7050\text{Al}$  composite. Higher magnification image of (c) the river zones; (d) the  $\text{TiB}_2$  cluster zones marked with red square in (b).

## 6.4 Discussion

For the  $\text{TiB}_2/7050\text{Al}$  composite, the fatigue cracks should propagate through two distinct microstructures (Fig. 6.2c) under the cyclic stress: (1)  $\text{TiB}_2$  lean zones inside grains; (2)  $\text{TiB}_2$  bands coexisting with GBs. Therefore, the FCG behavior and the corresponding mechanisms in these two distinct zones are completely different, and we shall discuss them separately.

### 6.4.1 FCG inside grains

For the age-hardening Al alloys, when the fatigue crack propagates inside grains, the concept of reversed slip of dislocations within the cyclic plastic zone ahead of the crack tip must be considered. During the unloading part of the cycle, the back stress in the dislocations that formed during the loading process forces them to move in the opposite direction on the same slip plane. This reversed dislocation movement should continue until the back stress equals to the friction stress of the matrix [183]. Therefore, a part of the dislocations can leave the slip plane at the crack tip and consequently result in the reduction of crack advance.

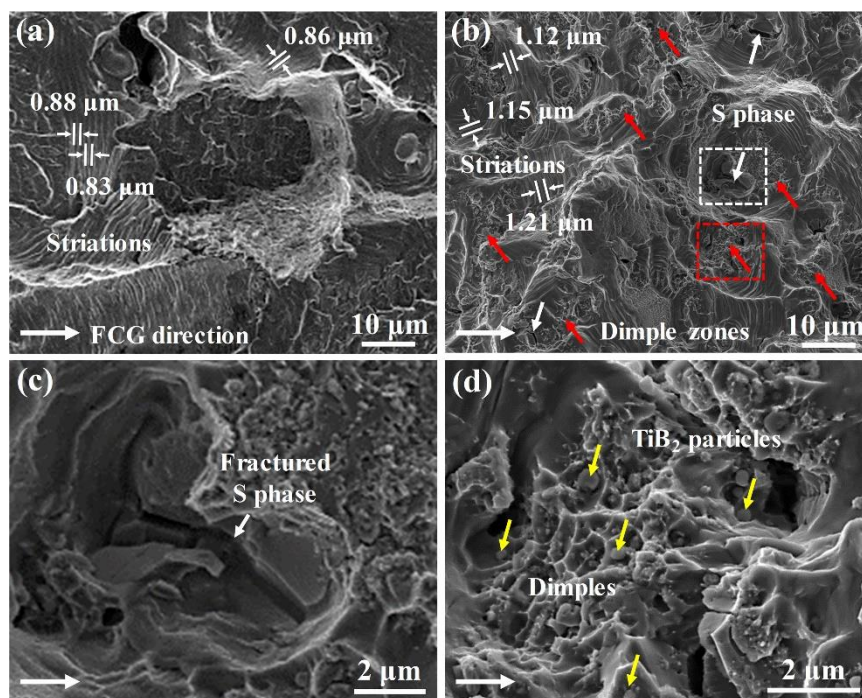


Fig. 6.9 (a) Fractographic features of the FCG at high  $\Delta K$  range. (a) 7050Al alloy; (b) TiB<sub>2</sub>/7050Al composite. Higher magnification image of (c) S phase marked with white square in (b); (d) dimple zones marked with red square in (b).

Based on this concept, Lindigkeit *et al.* [184] proposed that the reduced grain size leads to an increased FCG rate in age-hardening Al alloys. During the loading part of the cyclic stress, when the size of the cyclic plastic zone matches the grain size in the material with larger grains, the cyclic plastic zone in the material with smaller grain size can include more than one grain. Consequently, the advancing of the dislocations on the slip plane should be limited by the GBs in the material with smaller grains.

Accordingly, the dislocations should pile up on the GBs and lead to the generation of high local stress concentrations, which can induce the activation of the secondary slip systems [183, 184]. In this way, dislocations on the secondary slip plane should interact with the dislocations on the primary slip plane during the unloading process. The number of the dislocations moving backwards are decreased, which further lead to the larger FCG rate in the fine grain materials [184].

It has been well established that the size of the cyclic plastic zone ahead of the crack tip presents functional relation with  $\Delta K$  under plain stress conditions [185]:

$$\delta = \frac{1}{8\pi} \left( \frac{\Delta K}{\sigma_y} \right)^2 \quad (6.2)$$

where  $\delta$  is the size of the cyclic plastic zone ahead of the crack tip;  $\sigma_y$  is the yield strength of the material.

In the present study, the yield stress of the 7050Al alloy and TiB<sub>2</sub>/7050Al composite are 665 MPa and 684 MPa, respectively (Table 6.1). In stage I, the value of  $\Delta K$  is ~6.5-9.5 MPa.m<sup>1/2</sup> (Fig. 6.6). According to Eq. 6.2, the size ranges of the cyclic plastic zones of 7050Al alloy and TiB<sub>2</sub>/7050Al composite can be calculated to be ~3.8-8.1 μm and 3.6-7.7 μm, respectively. Meanwhile, the mean grain sizes of the 7050Al alloy and TiB<sub>2</sub>/7050Al composite are 22 μm and 8 μm (Fig. 6.5), respectively. Thus, the sizes of the cyclic plastic zone of both 7050Al alloy and TiB<sub>2</sub>/7050Al are smaller than their own grain size. Accordingly, the 7050Al alloy and TiB<sub>2</sub>/7050Al should have a similar FCG rate inside grains in at low  $\Delta K$  range.

In stage II, the value of  $\Delta K$  is ~9.5-21 MPa.m<sup>1/2</sup> (Fig. 6.6), and the size range of the cyclic plastic zone of TiB<sub>2</sub>/7050Al composite can be calculated to be ~7.7-37.5 μm. Obviously, the cyclic plastic zone of TiB<sub>2</sub>/7050Al composite can include more than one grain at intermediate  $\Delta K$  range. As for the 7050Al alloy, the cyclic plastic zone is smaller than the average grain size (22 μm) when  $\Delta K$  is smaller than 15.6 MPa.m<sup>1/2</sup>, while includes more than one grain when the value of  $\Delta K$  is ~15.6-21 MPa.m<sup>1/2</sup>. Hence, we should discuss them respectively. In the former case, the cyclic plastic zone of

TiB<sub>2</sub>/7050Al composite includes more than one grain while the cyclic plastic zone of 7050Al alloy includes only one grain. The FCG rate of the TiB<sub>2</sub>/7050Al composite is increased inside grains due to the reduced grain size. For the latter case, the cyclic plastic zone of the 7050Al alloy and TiB<sub>2</sub>/7050Al composite both include more than one grains. In this case, Lindigkeit et al. [184] proposed that compared to the material with larger grain size, still more grains are present within the cyclic plastic zone for the material exhibits finer grains. Consequently, the degree of the reversed slip of dislocations in the material with finer grains is always smaller than the material with larger grains [184]. Therefore, the FCG rate of the TiB<sub>2</sub>/7050Al composite is increased inside grains due to the reduced grain size at the latter part of the intermediate  $\Delta K$  range.

In stage III, the value of  $\Delta K$  is larger than 21 MPa.m<sup>1/2</sup>, and the size of the cyclic plastic zone of 7050Al alloy and TiB<sub>2</sub>/7050Al composite can be calculated to be larger than 39.7  $\mu\text{m}$  and 37.5  $\mu\text{m}$ , respectively. The cyclic plastic zone of the 7050Al alloy and TiB<sub>2</sub>/7050Al composite both include more than one grains, which is the same as the latter case of Stage II. Thus, the FCG rate of the TiB<sub>2</sub>/7050Al composite is increased inside grains due to the reduced grain size at high  $\Delta K$  range.

## **6.4.2 FCG at GBs**

### **6.4.2.1 Reduced FCG rate at low $\Delta K$ range**

For the 7050Al alloy, the preceding slip plane should discontinue when the crack approaches GBs, which leads to local crack arrest until a new crack is formed at slip steps in the nearest neighbor grain after an additional number of cycles [183]. As for TiB<sub>2</sub>/7050Al composite, the fatigue cracks have to propagate through the TiB<sub>2</sub> bands besides the GBs. Thus, the effects of the TiB<sub>2</sub> bands exerted on the FCG rate of TiB<sub>2</sub>/7050Al composite must be taken into consideration.

It is well established that the reinforcements with larger dimensions are more likely fracture under cyclic stress [25, 186, 187]. The larger dimensions facilitate a larger

degree of stress transfer from the matrix to the reinforcements. Meanwhile, the larger reinforcements are likely to contain larger inherent defects than the smaller ones, acting as potential stress concentrators in the ductile matrix [186, 187]. In fact, the probability of the fracture of reinforcements increase with the particle size, as described by the following equations [187]:

$$\begin{cases} P\{fr\} = 1 - \exp\left\{-\left(\frac{d}{\bar{d}}\right)^3 \cdot f(\sigma)\right\} \\ f(\sigma) = \left(\frac{\bar{d}}{d_N}\right)^3 \cdot \frac{\{\sigma_{\text{flow}}^{\text{matrix}} - \sigma_{\text{min}}^{\text{matrix}}\}^m}{\sigma_1^m} \end{cases} \quad (6.3)$$

where  $P\{fr\}$  is the probability of fracture;  $d$  is particle size;  $\bar{d}$  is the average particle size;  $f(\sigma)$  denotes a stress parameter;  $\sigma$  is the tensile stress acting on the particle;  $d_N$  is a normalization constant;  $\sigma_{\text{flow}}^{\text{matrix}}$  denotes the matrix flow stress;  $\sigma_{\text{min}}^{\text{matrix}}$  denotes the matrix stress corresponding to the minimum particle fracture stress;  $\sigma_1$  is a constant and  $m$  is the Weibull inhomogeneity factor. Therefore, the finer size of the reinforcement signifies the smaller probability of the fracture under the cyclic stress.

As for the TiB<sub>2</sub>/7050 composite, the size of the TiB<sub>2</sub> particles ranges from 15 nm to 350 nm, with the majority of them being 15-100 nm in size (Fig. 6.3b). Consequently, the TiB<sub>2</sub> particles are less likely to contain inherent defects than the micron-scale reinforcements. Meanwhile, the nanoscale size of the TiB<sub>2</sub> particles implies a severely reduced degree of stress can be transferred from the matrix to the them. The stress concentration also can be reduced by the near-spherical shape of the TiB<sub>2</sub> particles (Fig. 6.2b and Fig. 6.3a). Therefore, the TiB<sub>2</sub> particles are very unlikely fracture under the cyclic stress. This can be confirmed on the fractographic feature of TiB<sub>2</sub>/7050 composite in stage I (Fig. 6.7d), for no fractured TiB<sub>2</sub> particle is found. On the other hand, according to Fig. 6.3c, the TiB<sub>2</sub>/Al interface is clean and highly coherent, with preferential crystallographic ORs  $[101]_{\text{Al}}//[2\bar{1}\bar{1}0]_{\text{TiB}_2}$ ,  $(11\bar{1})_{\text{Al}}//(0001)_{\text{TiB}_2}$  and  $(020)_{\text{Al}}//(0\bar{1}11)_{\text{TiB}_2}$  being determined. These characteristics are in accordance with the previous reports and predicate a high-bonding TiB<sub>2</sub>/Al interface [79, 80, 85]. Consequently, the TiB<sub>2</sub> particles are also unlikely decohere from the matrix at low  $\Delta K$

range. In this way, the TiB<sub>2</sub> particles can lead to crack deflection promotion and the resultant enhancement of the fracture surface roughness. This should result in roughness-induced crack closure and the resulting improved FCG resistance of TiB<sub>2</sub>/7050 composite [26, 158, 159].

In accordance with this viewpoint, the TiB<sub>2</sub>/7050 composite shows a coarser fracture on the microstructural level compared to 7050Al alloy, which is caused by the occurrence of protrusion zones (Fig. 6.7b). The distribution of the protrusion zones is in accordance with the distribution of TiB<sub>2</sub> clusters, but only several TiB<sub>2</sub> particles are observed at the protrusion zones. This is a weighty evidence of the crack deflection at the TiB<sub>2</sub> bands. Consequently, the protrusion zones are the symbol of the fatigue crack deflection and the resultant roughness-induced crack closure. Furthermore, the inhomogeneous particle distribution can enhance the roughness-induced crack closure effect and thus improve the FCG resistance [161]. Hence, the inhomogeneous particle distribution in the TiB<sub>2</sub>/7050 composite can maximize the extrinsic crack shielding and roughness induced crack closure mechanisms, and thus further improve the FCG resistance. Notably, due to the large size and aspect ratio of the S phase (Fig. 6.2a and 6.2b), they are much more likely to fracture compared to TiB<sub>2</sub> particles. This can produce backward effects to the FCG resistance of TiB<sub>2</sub>/7050 composite to a certain extent.

The 7050Al alloy and TiB<sub>2</sub>/7050Al composite have the similar FCG rates inside grains at low  $\Delta K$  range. Meanwhile, the FCG resistance of TiB<sub>2</sub>/7050Al composite is improved at GBs by the crack deflection mechanism caused by the impediment of TiB<sub>2</sub> bands to the FCG. The combination of these two factors has resulted in the lower FCG rate of the TiB<sub>2</sub>/7050Al composite compared to 7050Al alloy at low  $\Delta K$  range. The schematic representation of the characteristics of the FCG path at low  $\Delta K$  range is shown in Fig. 6.10a-c.

#### **6.4.2.2 Reduced FCG rate at intermediate $\Delta K$ range**

In stage II, the value of  $\Delta K$  is higher than stage I. The  $\text{TiB}_2$  particles are still very unlikely fracture under the cyclic stress due to their nanoscale dimensions, which can be confirmed on the fractographic feature of  $\text{TiB}_2/7050$  composite in stage II (Fig. 6.8d), that no fractured  $\text{TiB}_2$  particle is observed. However, when the fatigue crack tip approaches the  $\text{TiB}_2$  bands, the incompatible strains between the plastically deforming matrix and the elastically deforming  $\text{TiB}_2$  particles eventually produce decohesion of the  $\text{TiB}_2/\text{Al}$  interface [25]. Meanwhile, the size range of the cyclic plastic zone of  $\text{TiB}_2/7050\text{Al}$  composite has been calculated to be 7.7-37.5  $\mu\text{m}$  at intermediate  $\Delta K$  range, which is much larger than the  $\text{TiB}_2$  particles. According to Shang and Ritchie [141], the fatigue crack trapping mechanism should be applied to the FCG process of the MMCs on the premise of these two conditions. The reinforcements interact with the front of the fatigue crack and impede crack advance in a way somewhat analogous to the hardening from dislocation particle interactions, such as dislocations bowing around obstacles or particle shearing [141]. Because the  $\text{TiB}_2$  particles are still very unlikely fracture at intermediate  $\Delta K$  range, the  $\text{TiB}_2$  particles shall impede crack advance by crack bowing. In accordance with this viewpoint,  $\text{TiB}_2$  cluster zones are observed in the fractographic features in stage II (Fig. 6.8b). A high density of  $\text{TiB}_2$  particles are found in the  $\text{TiB}_2$  cluster zones, with no obvious tear ridges or deep dimples being observed around the  $\text{TiB}_2$  particles (Fig. 6.8d). This phenomenon represents the fatigue crack trapping behavior between the fatigue crack and  $\text{TiB}_2$  particles.

The FCG rate of  $\text{TiB}_2/7050\text{Al}$  composite is increased inside grains due to the reduced grain size at intermediate  $\Delta K$  range. Meanwhile, the FCG resistance of  $\text{TiB}_2/7050\text{Al}$  composite is improved at GBs by the fatigue crack trapping mechanism. The combination of these two factors has resulted in the similar FCG rate between  $\text{TiB}_2/7050\text{Al}$  composite and 7050Al alloy at intermediate  $\Delta K$  range. The schematic representation of the characteristics of the FCG path at intermediate  $\Delta K$  range is shown in Fig. 6.10d-f.

#### **6.4.2.3 Increased FCG rate at high $\Delta K$ range**

The cyclic stress in the cyclic plastic zone of TiB<sub>2</sub>/7050Al composite is severely increased at high  $\Delta K$  range compared to stage I and II. During fatigue process, the effective plastic strain near the TiB<sub>2</sub>/Al interface must be released by interfacial debonding or particle fracture [25, 27]. Considering the nanoscale dimension of TiB<sub>2</sub> particles and the fact that no fractured TiB<sub>2</sub> particle is found on the fracture surface of TiB<sub>2</sub>/7050Al composite (Fig. 6.9d), the TiB<sub>2</sub> particles can avoid the occurrence of fracture even at high  $\Delta K$  range. In this way, the increased strain at the TiB<sub>2</sub>/Al interface has to be released by forming dimples. Moreover, because the particle cluster regions can develop a greater local area plastic strain [159, 188], the propensity for TiB<sub>2</sub>/Al interfacial debonding increases in TiB<sub>2</sub> bands. In addition, the large and fragile S phase coexisting with the TiB<sub>2</sub> bands shall fracture rapidly under the high cyclic stress, which also can accelerate the debonding of TiB<sub>2</sub> particles from the Al matrix. Thus, considering the size of the cyclic plastic zone (larger than 37.5  $\mu\text{m}$ ) is much larger than the width of TiB<sub>2</sub> bands (smaller than 15  $\mu\text{m}$ ), many TiB<sub>2</sub> particles shall decohere from the 7050Al matrix simultaneously when the cyclic plastic zone ahead of the fatigue crack tip approaches GBs. The crack should propagate by the conjunction of the microvoids that simultaneously generated during this process [189, 190], which dramatically increases the FCG rate of TiB<sub>2</sub>/7050Al composite at GBs [191, 192].

In accordance with this view, dimple zones are found on the fracture surface of TiB<sub>2</sub>/7050Al composite in stage III (Fig. 6.9b), with fractured S phase surrounded by dimples (Fig. 6.9c). According to the higher magnification image of the dimple zones (Fig. 6.9d), a high density of interconnected deep dimples is found. Meanwhile, TiB<sub>2</sub> particles are observed inside the dimple pockets. The tear ridges and dimples indicate the stress localization around them, which also suggest that these prematurely fractured S phase and de-bonded TiB<sub>2</sub> particles act as local crack initiation sites before the crack front encountering them.

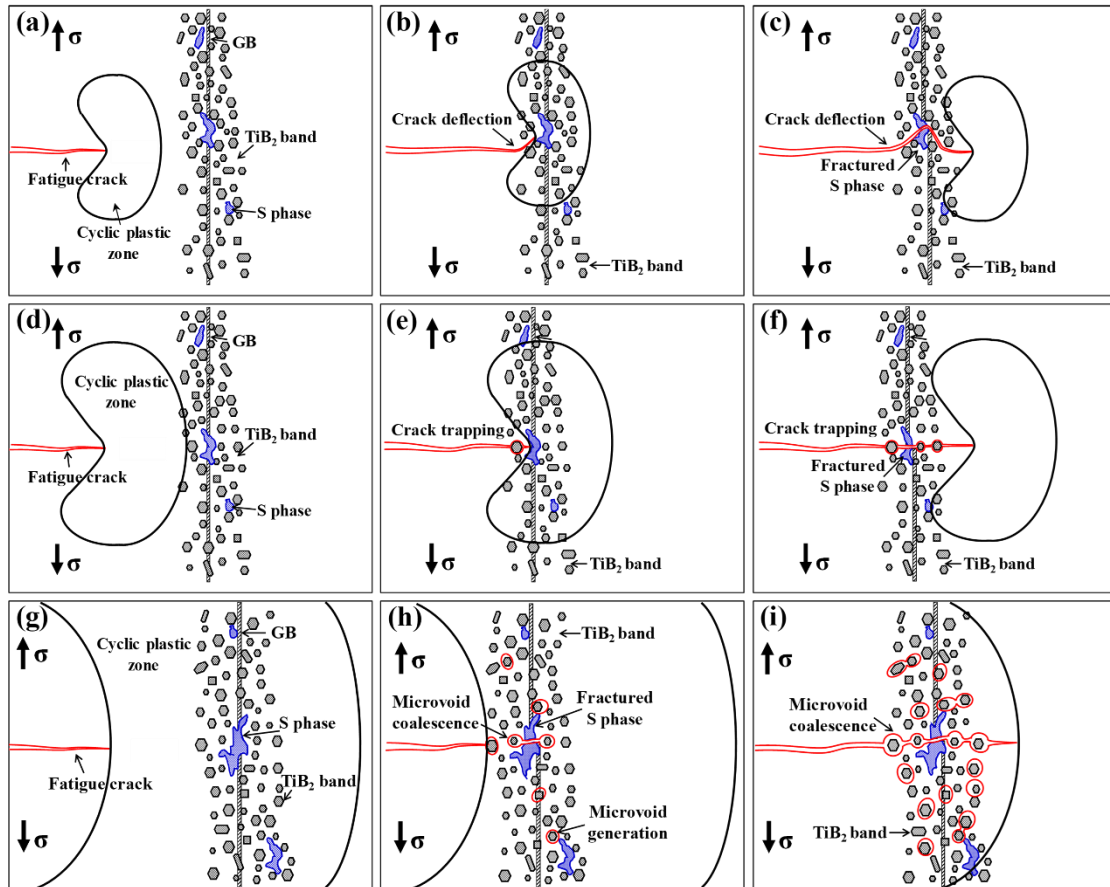


Fig. 6.10 Schematic representation of the characteristics of the FCG path of  $\text{TiB}_2/7050\text{Al}$  composite. (a-c) At low  $\Delta K$  range, showing the fatigue crack propagating inside grains, impeded by  $\text{TiB}_2$  band and passed through  $\text{TiB}_2$  band by crack deflection, accordingly; (d-f) at intermediate  $\Delta K$  range, showing the fatigue crack propagating inside grains, trapped by the  $\text{TiB}_2$  band and passed through  $\text{TiB}_2$  band via crack trapping, accordingly; (g-i) at high  $\Delta K$  range, presenting the fatigue crack propagating inside grains, connected with the microvoids generated inside  $\text{TiB}_2$  band and passed through the  $\text{TiB}_2$  band by microvoid coalescence, accordingly.

The FCG rate of  $\text{TiB}_2/7050\text{Al}$  composite is increased inside grains due to the reduced grain size at high  $\Delta K$  range. Meanwhile, the FCG rate of  $\text{TiB}_2/7050\text{Al}$  composite is increased at GBs via microvoid coalescence caused by the simultaneously decohesion of  $\text{TiB}_2$  particles in the cyclic plastic zones ahead of the fatigue crack tip. The combination of these two factors has resulted in the severely increased FCG rate of  $\text{TiB}_2/7050\text{Al}$  composite at high  $\Delta K$  range. The schematic representation of the

characteristics of the FCG path at the high  $\Delta K$  region is shown in Fig. 6.10g-i.

## 6.5 Conclusion

Based on the microstructure characterizations, the FCG behaviors and the corresponding mechanisms of the *in-situ* TiB<sub>2</sub>/7050Al composite are studied. The following conclusions are reached:

1. The TiB<sub>2</sub> presents a morphology of particle bands and clusters along and normal to ED, respectively. The TiB<sub>2</sub>/Al interface is clean and highly coherent, with crystal OR  $[101]_{\text{Al}}//[2\bar{1}\bar{1}0]_{\text{TiB}_2}$ ,  $(11\bar{1})_{\text{Al}}//(0001)_{\text{TiB}_2}$  being determined. The TiB<sub>2</sub>/7050Al composite exhibits a much finer grain size than the 7050Al alloy.
2. The TiB<sub>2</sub>/7050Al composite exhibits a lower, the similar and a higher FCG rate over the unreinforced 7050Al alloy at the low, intermediate and high  $\Delta K$  range, accordingly.
3. At low  $\Delta K$  range, the 7050Al alloy and TiB<sub>2</sub>/7050Al composite have a similar FCG rate inside grains. At GBs, the FCG resistance of TiB<sub>2</sub>/7050Al composite is improved via the crack deflection caused by TiB<sub>2</sub> bands. The combination of these two factors has resulted in the lower FCG rate of TiB<sub>2</sub>/7050Al composite in stage I.
4. At intermediate  $\Delta K$  range, the FCG rate of TiB<sub>2</sub>/7050Al composite is increased inside grains due to the reduced grain size. At GBs, the FCG resistance of TiB<sub>2</sub>/7050Al composite is improved by fatigue crack trapping. These combined two factors have led to the similar FCG rate between TiB<sub>2</sub>/7050Al composite and 7050Al alloy in stage II.
5. At high  $\Delta K$  range, the FCG rate of TiB<sub>2</sub>/7050Al composite is increased inside grains due to the reduced grain size. At GBs, the FCG rate of TiB<sub>2</sub>/7050Al composite is increased via microvoid coalescence caused by the simultaneously decohesion of TiB<sub>2</sub> particles in the cyclic plastic zones ahead of the fatigue crack

tip. These two factors have caused the severely increased FCG rate of TiB<sub>2</sub>/7050Al composite over 7050Al alloy in stage III.

# Chapter 7 Conclusion and Prospect

## 7.1 Conclusion

Along with the rapid development in aerospace and automobile industry, more severe demands, such as higher specific stiffness, specific strength and fatigue crack growth (FCG) resistance, have been raised. In parallel with the developments in nanotechnology, nanosized reinforcement particles (NRPs) have been introduced into the aluminum (Al) alloys aiming to provide an effective approach to meet the growing requirements in industrial applications. The introduced NRPs are expected to critically affect the interfacial precipitation and in turn, macroscopic mechanical properties of the Al-based metal matrix composites (MMCs), which raised most important fundamental problems remaining unresolved. In view of this, as the model material, an 6wt. %  $\text{TiB}_2$  nanoparticles reinforced Al-Zn-Mg-Cu alloy matrix composite ( $\text{TiB}_2/\text{Al-Zn-Mg-Cu}$  nanocomposite) has been designed, produced and investigated in order to provide a fundamental insight into the effects of NRPs on the interfacial precipitation, tensile properties and FCG resistance of Al-based MMCs. Scanning electron microscopy (SEM), electron backscatter diffraction (EBSD) and high-resolution scanning transmission electron microscopy (HRSTEM) were employed for the microstructure characterization. The corresponding material processing procedure, mechanical testing methods and characterization methods are given in Chapter 3.

Chapter 4 and Chapter 5 investigated the effects of uniformly distributed NRPs on the interface precipitation and tensile properties of Al-based MMCs. To reach this goal, an  $\text{TiB}_2/\text{Al-Zn-Mg-Cu}$  nanocomposite was successfully produced by *in-situ* casting, friction stir processing (FSP) and hot extrusion. This model material was used for atomic-scale HRSTEM characterization and room temperature tensile test. The obtained results indicate the significant effects of  $\text{TiB}_2$  nanoparticles on the interfacial

precipitation and in turn, the macroscopic mechanical properties of the TiB<sub>2</sub>/Al-Zn-Mg-Cu nanocomposite. Due to the effective FSP, the majority of TiB<sub>2</sub> nanoparticles are uniformly dispersed inside Al grains, featured with the basal {0001}, prismatic {01 $\bar{1}$ 0} and pyramidal {01 $\bar{1}$ 1} facets. At the solid-solution state, the well-documented orientation relationship (OR)1 ([2 $\bar{1}\bar{1}$ 0]<sub>TiB<sub>2</sub></sub>//[101]<sub>Al</sub>, (0001)<sub>TiB<sub>2</sub></sub>//( $\bar{1}$ 11)<sub>Al</sub>) and the new OR2 ([2 $\bar{1}\bar{1}$ 0]<sub>TiB<sub>2</sub></sub>//[101]<sub>Al</sub>, (01 $\bar{1}$ 0)<sub>TiB<sub>2</sub></sub>//(11 $\bar{1}$ )<sub>Al</sub>) between TiB<sub>2</sub> nanoparticles and Al matrix are determined. Notably, the majority of TiB<sub>2</sub> nanoparticles have OR1 with the Al matrix. The mismatch at the semi-coherent TiB<sub>2</sub>/Al interfaces parallel to the basal and prismatic/pyramidal facets of TiB<sub>2</sub> nanoparticles are 5.87 % and 38.03 %, respectively. At peak-aged and overaged states, interface precipitate (interphase, abbr. IP) identified as (Zn<sub>1.5</sub>Cu<sub>0.5</sub>)Mg was observed at certain TiB<sub>2</sub>/Al interfaces. The interfacial precipitation is closely related to the ORs between TiB<sub>2</sub> and Al matrix, while independent on the ageing conditions. At the OR1, the ORs between TiB<sub>2</sub> nanoparticle, (Zn<sub>1.5</sub>Cu<sub>0.5</sub>)Mg interphase and Al alloy matrix are: [2 $\bar{1}\bar{1}$ 0]<sub>TiB<sub>2</sub></sub>//[1 $\bar{1}$ 00]<sub>IP</sub>//[101]<sub>Al</sub>, (01 $\bar{1}$ 1)<sub>TiB<sub>2</sub></sub>//(0004)<sub>IP</sub> 3° from (020)<sub>Al</sub>, (01 $\bar{1}$ 0)<sub>TiB<sub>2</sub></sub>//(11 $\bar{2}$ 8)<sub>IP</sub>, (11 $\bar{2}$ 4)<sub>IP</sub>//(11 $\bar{1}$ )<sub>Al</sub>, ( $\bar{1}\bar{1}$ 20)<sub>IP</sub> 3° from ( $\bar{2}$ 02)<sub>Al</sub>. At the OR2, the ORs are: [2 $\bar{1}\bar{1}$ 0]<sub>TiB<sub>2</sub></sub>//[1 $\bar{1}$ 00]<sub>IP</sub>//[101]<sub>Al</sub>, (01 $\bar{1}$ 0)<sub>TiB<sub>2</sub></sub>//(11 $\bar{2}$ 0)<sub>IP</sub>//(11 $\bar{1}$ )<sub>Al</sub>, (0001)<sub>TiB<sub>2</sub></sub>//(0004)<sub>IP</sub>, ( $\bar{1}\bar{1}$ 24)<sub>IP</sub> 3° from ( $\bar{2}$ 02)<sub>Al</sub>, (11 $\bar{2}$ 8)<sub>IP</sub> 3° from (020)<sub>Al</sub>. The nucleation energy barrier for the heterogeneous precipitations at the TiB<sub>2</sub>/Al interface is considerably reduced compared to the homogeneous nucleation in the Al matrix away from such an interface. The highly-dense misfit dislocations at the TiB<sub>2</sub>/Al interfaces are beneficial for the nucleation and effective growth of the interphase since they provide short-circuit diffusion paths for solute atoms and vacancies. The growth of the precipitates at the TiB<sub>2</sub>/Al interfaces parallel to the close-packed {111} planes of the Al matrix is severely suppressed due to the ultra-low accommodation factor. The precipitation process is not fully completed at the peak-aged state, which is featured by the transitional half-grown zone (HGZ) presenting at the growth front of the interphase. Compared with the fully-grown zone (FGZ), the HGZ contains misfit dislocations and slightly different interplanar spacing. Through the peak-aging treatment, the high-

mismatch semi-coherent  $\text{TiB}_2/\text{Al}$  interfaces with high coherency strains were transformed into low-mismatch  $\text{Al}/\text{interphase}/\text{TiB}_2$  multi-interfaces with very low coherency strains. Thus, the  $\text{TiB}_2/\text{Al}$  interfaces are greatly strengthened by the heterogeneous interface precipitation, which is defined as precipitation assisted interface strengthening (PAIS). Correspondingly, due to the combined effects of  $\text{TiB}_2/\text{dislocation}$  interaction and PAIS, the  $\text{TiB}_2/\text{Al-Zn-Mg-Cu}$  nanocomposite presents a remarkable combination of strength (yield strength of 600 MPa) and ductility (uniform elongation of 12%), being higher than any Al or Al based materials ever reported.

Chapter 6 investigated the effects of NRPs on the FCG property of Al-based MMCs. Due to size limit of the nugget zone after FSP, the model material  $\text{TiB}_2/\text{Al-Zn-Mg-Cu}$  nanocomposite was produced by *in-situ* casting directly followed by hot extrusion and T6 heat treatment. The  $\text{TiB}_2/\text{Al-Zn-Mg-Cu}$  nanocomposite exhibits a much finer grain size than the unreinforced Al-Zn-Mg-Cu alloy. Due to the lack of FSP, the majority of  $\text{TiB}_2$  nanoparticles tend to aggregate along grain boundaries (GBs). The  $\text{TiB}_2/\text{Al-Zn-Mg-Cu}$  nanocomposite exhibits a lower, the similar and a higher FCG rate over the unreinforced Al-Zn-Mg-Cu alloy at the low, intermediate and high stress intensity factor ( $\Delta K$ ) range, accordingly. At low  $\Delta K$  range, the Al-Zn-Mg-Cu alloy and  $\text{TiB}_2/\text{Al-Zn-Mg-Cu}$  nanocomposite have a similar FCG rate inside grains. At GBs, the FCG resistance of the  $\text{TiB}_2/\text{Al-Zn-Mg-Cu}$  nanocomposite is improved via the crack deflection caused by  $\text{TiB}_2$  clusters. The combination of these two factors has resulted in the lower FCG rate of  $\text{TiB}_2/\text{Al-Zn-Mg-Cu}$  nanocomposite in stage I. At intermediate  $\Delta K$  range, the FCG rate of  $\text{TiB}_2/\text{Al-Zn-Mg-Cu}$  nanocomposite is increased inside grains due to the reduced grain size. At GBs, the FCG resistance of  $\text{TiB}_2/\text{Al-Zn-Mg-Cu}$  nanocomposite is improved by fatigue crack trapping. These combined two factors have led to the similar FCG rate between  $\text{TiB}_2/\text{Al-Zn-Mg-Cu}$  nanocomposite and Al-Zn-Mg-Cu alloy in stage II. At high  $\Delta K$  range, the FCG rate of  $\text{TiB}_2/\text{Al-Zn-Mg-Cu}$  nanocomposite is increased inside grains due to the reduced grain size. At GBs, the

FCG rate of TiB<sub>2</sub>/Al-Zn-Mg-Cu nanocomposite is increased via microvoid coalescence caused by the mass of decohesion of TiB<sub>2</sub> particles in the cyclic plastic zone ahead of the fatigue crack tip. These two factors have caused the severely increased FCG rate of TiB<sub>2</sub>/Al-Zn-Mg-Cu nanocomposite over Al-Zn-Mg-Cu alloy in stage III.

## **7.2 Remark**

### **7.2.1 Effects of TiB<sub>2</sub> nanoparticles on interfacial precipitation**

It has been well established that the micron- (or submicron-)sized reinforcement particle (MRP)/Al interfaces can greatly affect the interfacial precipitation and mechanical properties of the Al-based MMCs. Considering the TiB<sub>2</sub>/Al interface characteristics are different from the MRP/Al ones, the TiB<sub>2</sub>/Al interfaces shall have different effects on the interfacial precipitation and mechanical properties of the Al-based MMCs. The MRP/Al interface is incoherent, which is analogous to the high-angle GBs. Besides, oxide particles and thermoelastic stress induced dislocations (TSIDs) are also observed at the MRP/Al interfaces at solid-solution state. These interface characteristics can lead to the vacancy or solutes depletion and thus the formation of precipitate free zones (PFZs) and coarse precipitate zones (CPZs) in the surrounding matrix of MRPs. On the contrary, our atomic-scale characterization clearly demonstrated that the TiB<sub>2</sub>/Al interfaces are semi-coherent and free of oxides or TSIDs at solid-solution state. Therefore, no CPZs or PFZs can form in the surrounding matrix of TiB<sub>2</sub> nanoparticles due to the lack of TSIDs and vacancy/solute depletion. In addition, the clean, flat and semi-coherent TiB<sub>2</sub>/Al interfaces are ideal heterogeneous precipitation sites. Meanwhile, considering the TiB<sub>2</sub> nanoparticles have ORs with Al matrix, the interphase thus simultaneously has ORs with the TiB<sub>2</sub> nanoparticles and Al matrix. Because the MRPs have no ORs with Al matrix, this phenomenon is incapable at MRP/Al interfaces.

### **7.2.2 Effects of TiB<sub>2</sub> nanoparticles on tensile properties**

As is well-known, although MRPs reinforced MMCs possess high strength, it appears hopeless for them to have high ductility due to the weak MRP/matrix interfaces, not to mention the CPZs and PFZs formation during the aging treatment can further reduce their tensile properties. When it comes to TiB<sub>2</sub>/Al-Zn-Mg-Cu nanocomposite, the high-misfit TiB<sub>2</sub>/Al interfaces are transformed into low-misfit Al/(Zn<sub>1.5</sub>Cu<sub>0.5</sub>)Mg interphase/TiB<sub>2</sub> multi-interfaces in this thesis. It has been well established that the misfit dislocations at the phase interfaces create large coherency strains, which in turn can promote crack initiation underload. Therefore, the significantly reduced misfit of the Al/(Zn<sub>1.5</sub>Cu<sub>0.5</sub>)Mg/TiB<sub>2</sub> multi-interfaces greatly strengthened the original high-misfit TiB<sub>2</sub>/Al interfaces. Accordingly, the TiB<sub>2</sub>/Al-Zn-Mg-Cu nanocomposite presents a remarkable combination of strength and ductility in this thesis.

### **7.2.3 Effects of TiB<sub>2</sub> nanoparticles on FCG**

MRPs reinforced Al-based MMCs show a high FCG rate at intermediate  $\Delta K$  range ascribed to the severe MRPs fracture or MRP/Al interface debonding in the cyclic plastic zone ahead of the fatigue crack tip. For the TiB<sub>2</sub>/Al-Zn-Mg-Cu nanocomposite in this thesis, TiB<sub>2</sub> nanoparticles are unlikely to fracture because of their nanoscale size. Besides, the strength of the Al/(Zn<sub>1.5</sub>Cu<sub>0.5</sub>)Mg interphase/TiB<sub>2</sub> multi-interfaces is much higher than the incoherent MRP/Al interfaces. Consequently, the TiB<sub>2</sub>/Al-Zn-Mg-Cu nanocomposite presents a much lower FCG rate at intermediate  $\Delta K$  range.

### **7.2.4 General remark**

Strength and ductility are the two most important mechanical properties of a structural material. However, for centuries engineers have been facing a dilemma that they are often mutually exclusive, that is, a material may be strong or ductile, but rarely both at the same time. Introducing MRPs into the Al alloys matrix provides an effective way to improve the tensile strength. Unfortunately, the concurrently formed MRP/Al interfaces become the dominant defects in MMCs. During plastic deformation, the dislocations pile up at those weak interfaces and make them strong stress concentrative

points. This makes it appear hopeless for MMCs to have high ductility and it has been taken for granted that they are super strong but inevitably low ductility.

In the present thesis, the Al-Zn-Mg-Cu matrix composite reinforced with 6wt. % uniformly distributed TiB<sub>2</sub> nanoparticles, was successfully produced by the processing route combining casting, friction stir processing, hot extrusion and systematically examined at the solid-solution and peak-aged state. Our results demonstrate that the TiB<sub>2</sub> nanoparticles have a significant impact on the interfacial precipitation. The misfit dislocations at the TiB<sub>2</sub>/Al interfaces have promoted the heterogeneous precipitation at the TiB<sub>2</sub>/Al interfaces, and the interface precipitate was determined as (Zn<sub>1.5</sub>Cu<sub>0.5</sub>)Mg phase. It is also found that the misfit values of the Al/(Zn<sub>1.5</sub>Cu<sub>0.5</sub>)Mg interphase/TiB<sub>2</sub> multi-interfaces are greatly reduced compared to the original TiB<sub>2</sub>/Al interfaces, i.e., the TiB<sub>2</sub>/Al interfaces are greatly strengthened by the heterogeneous interface precipitation. Correspondingly, the result of tensile tests demonstrates that the TiB<sub>2</sub>/Al-Zn-Mg-Cu nanocomposite presents a remarkable combination of strength (yield strength of 600 MPa) and ductility (uniform elongation of 12%), being higher than any Al or Al based materials ever reported. Consequently, here we report this new strategy for the design of NRPs reinforced Al-based MMCs with an exceptional combination of strength and ductility based on the concept of precipitation assisted interface strengthening mechanism. Moreover, the FCG resistance of the TiB<sub>2</sub>/Al-Zn-Mg-Cu nanocomposite also can be improved. Theoretically, our strategy is applicable to all of the NRPs reinforced age-hardenable Al alloys matrix composites, paving a cost-effective and scalable way for their large-scale industrial applications.

### **7.3 Prospect of future work**

This thesis has revealed the effects of TiB<sub>2</sub> nanoparticles on the interfacial precipitation, tensile properties and FCG resistance of the TiB<sub>2</sub>/Al-Zn-Mg-Cu nanocomposite. The future work based on this study can be carried out in the following ways:

1. We have conducted detailed investigations on the effects of TiB<sub>2</sub> nanoparticles on interfacial precipitation at peak-aged and overaged states. However, the interfacial precipitation at underaged state remains unclear. Therefore, we shall conduct the *in-situ* HRSTEM experiments to study the early stage interface precipitation reactions in order to thoroughly reveal the whole interfacial precipitation process.
2. By investigating the already deformed samples, we have confirmed the interphase/dislocation interaction. Nevertheless, the specific interaction process is still unclear. Thus, we shall conduct an *in-situ* tensile testing experiment in order to acquire the direct and solid evidences to further reveal the specific interaction process between the (Zn<sub>1.5</sub>Cu<sub>0.5</sub>)Mg interphase and dislocations.
3. In this thesis, we have studied the effects of non-uniformly distributed TiB<sub>2</sub> nanoparticles on the FCG property of TiB<sub>2</sub>/Al-Zn-Mg-Cu nanocomposite. Subsequently, we shall conduct the investigation on the influences of uniformly distributed TiB<sub>2</sub> nanoparticles on the FCG properties of TiB<sub>2</sub>/Al-Zn-Mg-Cu nanocomposite.
4. Theoretically, the effects of TiB<sub>2</sub> nanoparticles on the interfacial precipitation and mechanical properties of TiB<sub>2</sub>/Al-Zn-Mg-Cu nanocomposite are applicable to all of the NRPs reinforced age-hardenable Al alloys matrix composites. Hence, in order to prove this theory, we shall conduct corresponding investigations on 2xxx series Al alloys (i.e., Al-Cu(-Mg) alloys) and 6xxx series Al alloys (i.e., Al-Mg-Si alloys) matrix composites reinforced with uniformly distributed TiB<sub>2</sub> nanoparticles.

# References

- [1] Williams JC, Starke Jr EA. Progress in structural materials for aerospace systems I. *Acta Materialia*. 2003;51(19):5775-99.
- [2] Liddicoat PV, Liao X-Z, Zhao Y, Zhu Y, Murashkin MY, Lavernia EJ, et al. Nanostructural hierarchy increases the strength of aluminium alloys. *Nature communications*. 2010;1:63.
- [3] Sun W, Zhu Y, Marceau R, Wang L, Zhang Q, Gao X, et al. Precipitation strengthening of aluminum alloys by room-temperature cyclic plasticity. *Science*. 2019;363(6430):972-5.
- [4] Ardell A. Precipitation hardening. *Metallurgical Transactions A*. 1985;16(12):2131-65.
- [5] Zhao Y-H, Liao X-Z, Cheng S, Ma E, Zhu YT. Simultaneously increasing the ductility and strength of nanostructured alloys. *Advanced Materials*. 2006;18(17):2280-3.
- [6] Cao F, Zheng J, Jiang Y, Chen B, Wang Y, Hu T. Experimental and DFT characterization of  $\eta'$  nano-phase and its interfaces in Al-Zn-Mg-Cu alloys. *Acta Materialia*. 2018.
- [7] McDanel DL. Analysis of stress-strain, fracture, and ductility behavior of aluminum matrix composites containing discontinuous silicon carbide reinforcement. *Metallurgical transactions A*. 1985;16(6):1105-15.
- [8] Chawla N, Ganesh V, Wunsch B. Three-dimensional (3D) microstructure visualization and finite element modeling of the mechanical behavior of SiC particle reinforced aluminum composites. *Scripta Materialia*. 2004;51(2):161-5.
- [9] Kai W, Yang J-M, Harrigan Jr W. Mechanical behavior of B<sub>4</sub>C particulate-reinforced 7091 aluminum composite. *Scripta metallurgica*. 1989;23(8):1277-80.
- [10] Chawla N, Andres C, Davis L, Jones J, Allison J. The interactive role of inclusions and SiC reinforcement on the high-cycle fatigue resistance of particle reinforced metal matrix composites. *Metallurgical and Materials Transactions A*. 2000;31(13):951-7.
- [11] Chawla N, Jones J, Andres C, Allison J. Effect of SiC volume fraction and particle size on the fatigue resistance of a 2080 Al/SiC p composite. *Metallurgical and Materials Transactions A*. 1998;29(11):2843-54.

- [12] Vogelsang M, Arsenault R, Fisher R. An in situ HVEM study of dislocation generation at Al/SiC interfaces in metal matrix composites. *Metallurgical Transactions A*. 1986;17(3):379-89.
- [13] Christman T, Suresh S. Microstructural development in an aluminum alloy-SiC whisker composite. *Acta Metallurgica*. 1988;36(7):1691-704.
- [14] Dutta I, Bourell D. Influence of dislocation density and distribution on the aging behavior of 6061 AlSiCw composites. *Acta Metallurgica et Materialia*. 1990;38(11):2041-9.
- [15] Starink M, Wang P, Sinclair I, Gregson P. Microstructure and strengthening of Al-Li-Cu-Mg alloys and mmcs: I. Analysis and modelling of microstructural changes. *Acta materialia*. 1999;47(14):3841-53.
- [16] Nieh T, Karlak R. Aging characteristics of B<sub>4</sub>C-reinforced 6061-aluminum. *Scripta metallurgica*. 1984;18(1):25-8.
- [17] Papazian JM. Effects of SiC whiskers and particles on precipitation in aluminum matrix composites. *Metallurgical Transactions A*. 1988;19(12):2945-53.
- [18] Wu C, Ma K, Zhang D, Wu J, Xiong S, Luo G, et al. Precipitation phenomena in Al-Zn-Mg alloy matrix composites reinforced with B<sub>4</sub>C particles. *Scientific reports*. 2017;7(1):9589.
- [19] Hong S, Gray III G. Microstructure and microchemistry of an Al-Zn-Mg-Cu alloy matrix-20 vol.% SiC composite. *Acta metallurgica et materialia*. 1992;40(12):3299-315.
- [20] Starink M, Gregson P. S' and δ' phase precipitation in SiCp reinforced Al-1.2 wt.% Cu-1wt.%Mg-xLi alloys. *Materials Science and Engineering: A*. 1996;211(1-2):54-65.
- [21] Hu H, Lavernia E, Harrigan W, Kajuch J, Nutt S. Microstructural investigation on B<sub>4</sub>C/Al-7093 composite. *Materials Science and Engineering: A*. 2001;297(1-2):94-104.
- [22] Strangwood M, Hipsley C, Lewandowski J. Segregation to SiC/Al interfaces in Al based metal matrix composites. *Scripta Metallurgica et Materialia*. 1990;24(8):1483-7.
- [23] Ashby M. Work hardening of dispersion-hardened crystals. *Philosophical Magazine*. 1966;14(132):1157-78.
- [24] Arzt E, Dehm G, Gumbsch P, Kraft O, Weiss D. Interface controlled plasticity in metals: dispersion hardening and thin film deformation. *Progress in Materials Science*. 2001;46(3):283-307.

- [25] Kumai S, King JE, Knott JF. Short and long fatigue crack growth in a SiC reinforced aluminium alloy. *Fatigue & Fracture of Engineering Materials & Structures*. 1990;13(5):511-24.
- [26] Levin M, Karlsson B. Influence of SiC particle distribution and prestraining on fatigue crack growth rates in aluminium AA 6061–SiC composite material. *Materials Science and Technology*. 1991;7(7):596-607.
- [27] Shang JK, Yu W, Ritchie R. Role of silicon carbide particles in fatigue crack growth in SiC-particulate-reinforced aluminum alloy composites. *Materials Science and Engineering: A*. 1988;102(2):181-92.
- [28] Tjong SC, Ma Z. Microstructural and mechanical characteristics of in situ metal matrix composites. *Materials Science and Engineering: R: Reports*. 2000;29(3):49-113.
- [29] Chen L-Y, Xu J-Q, Choi H, Pozuelo M, Ma X, Bhowmick S, et al. Processing and properties of magnesium containing a dense uniform dispersion of nanoparticles. *Nature*. 2015;528(7583):539-43.
- [30] Kim C, Lee J, Plichta M. Plastic relaxation of thermoelastic stress in aluminum/ceramic composites. *Metallurgical Transactions A*. 1990;21(2):673-82.
- [31] Ashby M, Johnson L. On the generation of dislocations at misfitting particles in a ductile matrix. *Philosophical Magazine*. 1969;20(167):1009-22.
- [32] Johnson W, Lee J. A dislocation model for the plastic relaxation of the transformation strain energy of a misfitting spherical particle. *Acta Metallurgica*. 1983; 31(7):1033-45.
- [33] Starink M, Wang P, Sinclair I, Gregson P. Microstructure and strengthening of Al–Li–Cu–Mg alloys and MMCs: II. Modelling of yield strength. *Acta materialia*. 1999;47(14):3855-68.
- [34] Papazian J, Adler P. Tensile properties of short fiber-reinforced SiC/AI composites: Part I. effects of matrix precipitates. *Metallurgical transactions A*. 1990;21(1):401-10.
- [35] Nutt S, Carpenter R. Non-equilibrium phase distribution in an Al-SiC composite. *Materials Science and Engineering*. 1985;75(1-2):169-77.
- [36] Jiang L, Wen H, Yang H, Hu T, Topping T, Zhang D, et al. Influence of length-scales on spatial distribution and interfacial characteristics of B<sub>4</sub>C in a nanostructured Al matrix. *Acta Materialia*. 2015;89:327-43.
- [37] Porter DA, Easterling KE, Sherif M. *Phase Transformations in Metals and Alloys*, (Revised Reprint): CRC press; 2009.
- [38] Christian JW. *The theory of transformations in metals and alloys*: Newnes; 2002.

- [39] Jiang L, Ma K, Yang H, Li M, Lavernia EJ, Schoenung JM. The microstructural design of trimodal aluminum composites. *JOM*. 2014;66(6):898-908.
- [40] Munro RG. Material properties of titanium diboride. *Journal of Research of the National Institute of Standards and Technology*. 2000;105(5):709.
- [41] Ma Y, Chen Z, Wang M, Chen D, Ma N, Wang H. High cycle fatigue behavior of the in-situ TiB<sub>2</sub>/7050 composite. *Materials Science and Engineering: A*. 2015;640:350-6.
- [42] Chen Z, Sun G, Wu Y, Mathon M, Borbely A, Chen D, et al. Multi-scale study of microstructure evolution in hot extruded nano-sized TiB<sub>2</sub> particle reinforced aluminum composites. *Materials & Design*. 2017;116:577-90.
- [43] Liu J, Chen Z, Zhang F, Ji G, Wang M, Ma Y, et al. Simultaneously increasing strength and ductility of nanoparticles reinforced Al composites via accumulative orthogonal extrusion process. *Materials Research Letters*. 2018;6(8):406-12.
- [44] Reingold N, Park J, Rice J. *Materials research chronology, 1917-1957*. Library of congress Washington DC science and technology DIV; 1962.
- [45] Starke Jr EA, Staley JT. Application of modern aluminum alloys to aircraft. *Progress in aerospace sciences*. 1996;32(2-3):131-72.
- [46] Weber LJ. Aluminum alloy. Google Patents; 1933.
- [47] Yoshida H. Alloy Development for Transportation in Sumitomo Light Metal. 往友軽金属技報. 2010;51(1):112-20.
- [48] Liu J, Kulak M. A new paradigm in the design of aluminum alloys for aerospace applications. *Materials Science Forum: Trans Tech Publ*; 2000. p. 127-42.
- [49] Immarigeon J, Holt R, Koul A, Zhao L, Wallace W, Beddoes J. Lightweight materials for aircraft applications. *Materials characterization*. 1995;35(1):41-67.
- [50] Starke E, Staley J. Application of modern aluminum alloys to aircraft. *Progress in Aerospace Sciences*. 1996;32(2-3):131-72.
- [51] Li Y-Y, Kovarik L, Phillips PJ, Hsu Y-F, Wang W-H, Mills MJ. High-resolution characterization of the precipitation behavior of an Al–Zn–Mg–Cu alloy. *Philosophical Magazine Letters*. 2012;92(4):166-78.
- [52] Deschamps A, Livet F, Brechet Y. Influence of predeformation on ageing in an Al–Zn–Mg alloy—I. Microstructure evolution and mechanical properties. *Acta Materialia*. 1998;47(1):281-92.

- [53] Sha G, Wang Y, Liao X, Duan Z, Ringer S, Langdon T. Influence of equal-channel angular pressing on precipitation in an Al–Zn–Mg–Cu alloy. *Acta Materialia*. 2009; 57(10):3123-32.
- [54] Su J-Q, Nelson T, Mishra R, Mahoney M. Microstructural investigation of friction stir welded 7050-T651 aluminium. *Acta materialia*. 2003;51(3):713-29.
- [55] Sha G, Cerezo A. Early-stage precipitation in Al–Zn–Mg–Cu alloy (7050). *Acta Materialia*. 2004;52(15):4503-16.
- [56] Deschamps A, Bley F, Livet F, Fabregue D, David L. In-situ small-angle X-ray scattering study of dynamic precipitation in an Al-Zn-Mg-Cu alloy. *Philosophical Magazine*. 2003;83(6):677-92.
- [57] Deschamps A, Fribourg G, Bréchet Y, Chemin J, Hutchinson C. In situ evaluation of dynamic precipitation during plastic straining of an Al–Zn–Mg–Cu alloy. *Acta materialia*. 2012;60(5):1905-16.
- [58] Deschamps A, Brechet Y. Influence of predeformation and ageing of an Al–Zn–Mg alloy—II. Modeling of precipitation kinetics and yield stress. *Acta Materialia*. 1998; 47(1):293-305.
- [59] Thackery P. The nature and morphology of precipitate in aluminum-zink-magnesium alloys. *J Inst Metals*. 1968;96(8):228-35.
- [60] Shewmon P. *Diffusion in solids*: Springer; 2016.
- [61] Hu T, Ma K, Topping T, Schoenung J, Lavernia E. Precipitation phenomena in an ultrafine-grained Al alloy. *Acta Materialia*. 2013;61(6):2163-78.
- [62] Allen RM, Vander Sande JB. The oriented growth of precipitates on dislocations in Al-Zn-Mg—part I. Experimental observations. *Acta Metallurgica*. 1980;28(9):1185-95.
- [63] Ma K, Hu T, Yang H, Topping T, Yousefiani A, Lavernia EJ, et al. Coupling of dislocations and precipitates: impact on the mechanical behavior of ultrafine grained Al–Zn–Mg alloys. *Acta Materialia*. 2016;103:153-64.
- [64] Embury J, Nicholson R. The nucleation of precipitates: the system Al-Zn-Mg. *Acta Metallurgica*. 1965;13(4):403-17.
- [65] Unwin P, Lorimer G, Nicholson R. The origin of the grain boundary precipitate free zone. *Acta Metallurgica*. 1969;17(11):1363-77.
- [66] Cottrell AH, Bilby B. Dislocation theory of yielding and strain ageing of iron. *Proceedings of the Physical Society Section A*. 1949;62(1):49.

- [67] Harper S. Precipitation of carbon and nitrogen in cold-worked alpha-iron. *Physical review*. 1951;83(4):709.
- [68] Ham FS. Stress-assisted precipitation on dislocations. *Journal of Applied Physics*. 1959;30(6):915-26.
- [69] Legros M, Dehm G, Arzt E, Balk TJ. Observation of giant diffusivity along dislocation cores. *Science*. 2008;319(5870):1646-9.
- [70] Park JK, Ardell A. Precipitation at grain boundaries in the commercial alloy Al 7075. *Acta Metallurgica*. 1986;34(12):2399-409.
- [71] Westwood A. Materials for advanced studies and devices. *Metallurgical Transactions A*. 1988;19(4):749-58.
- [72] Higashi I, Takahashi Y, Atoda T. Crystal growth of borides and carbides of transition metals from molten aluminum solutions. *Journal of Crystal Growth*. 1976; 33(2):207-11.
- [73] Lönnberg B. Thermal expansion studies on the group IV–VII transition metal diborides. *Journal of the Less Common Metals*. 1988;141(1):145-56.
- [74] Fan Z, Wang Y, Zhang Y, Qin T, Zhou X, Thompson G, et al. Grain refining mechanism in the Al/Al–Ti–B system. *Acta Materialia*. 2015;84:292-304.
- [75] Ma Z, Li J, Li S, Ning X, Lu Y, Bi J. Property-microstructure correlation in in situ formed Al<sub>2</sub>O<sub>3</sub>, TiB<sub>2</sub> and Al<sub>3</sub>Ti mixture-reinforced aluminium composites. *Journal of materials science*. 1996;31(3):741-7.
- [76] Ma Z, Li J, Lu Y, Ning X, Bi J. In situ Al<sub>2</sub>O<sub>3</sub>-TiB<sub>2</sub>/Al-Cu composite fabricated by reaction pressing of TiO<sub>2</sub>-Al-B-CuO system. *Journal of materials science & technology*. 1996;12(1):25-8.
- [77] Ma Z, Li J, Luo M, Ning X, Lu Y, Bi J, et al. In-situ formed Al<sub>2</sub>O<sub>3</sub> and TiB<sub>2</sub> particulates mixture-reinforced aluminum composite. *Scripta metallurgica et materialia*. 1994;31(5):635-9.
- [78] Ma Z, Tjong S. In Situ ceramic particle-reinforced aluminum matrix composites fabricated by reaction pressing in the TiO<sub>2</sub> (Ti)-Al-B (B<sub>2</sub>O<sub>3</sub>) systems. *Metallurgical and Materials Transactions A*. 1997;28(9):1931-42.
- [79] Tang Y, Chen Z, Borbely A, Ji G, Zhong S, Schryvers D, et al. Quantitative study of particle size distribution in an in-situ grown Al–TiB<sub>2</sub> composite by synchrotron X-ray diffraction and electron microscopy. *Materials Characterization*. 2015;102:131-6.

- [80] Geng J, Liu G, Wang F, Hong T, Dai J, Wang M, et al. Microstructural correlated damage mechanisms of the high-cycle fatigued in-situ TiB<sub>2</sub>/Al-Cu-Mg composite. *Materials & Design*. 2017;135:423-38.
- [81] Ma Y, Geng J, Chen Z, Wang M, Chen D, Ji G, et al. Experimental study of the mechanisms of nanoparticle influencing the fatigue crack growth in an in-situ TiB<sub>2</sub>/Al-Zn-Mg-Cu composite. *Engineering Fracture Mechanics*. 2019;207:23-35.
- [82] Mitra R, Chiou W, Weertman J, Fine M, Aikin R. Relaxation mechanisms at the interfaces in XD™ Al/TiCp metal matrix composites. *Scripta metallurgica et materialia*. 1991;25(12):2689-94.
- [83] Mitra R, Chiou W, Fine M, Weertman J. Interfaces in as-extruded XD Al/TiC and Al/TiB<sub>2</sub> metal matrix composites. *Journal of materials research*. 1993;8(9):2380-92.
- [84] Schaffer PL, Miller DN, Dahle AK. Crystallography of engulfed and pushed TiB<sub>2</sub> particles in aluminium. *Scripta Materialia*. 2007;57(12):1129-32.
- [85] Li X, Ji G, Chen Z, Addad A, Wu Y, Wang H, et al. Selective laser melting of nano-TiB<sub>2</sub> decorated AlSi10Mg alloy with high fracture strength and ductility. *Acta Materialia*. 2017;129:183-93.
- [86] Kellie J, Wood J. Reaction processing in the metals industry. *Materials world*. 1995;3(1):10-2.
- [87] Sterling CJ. Effects of friction stir processing on the microstructure and mechanical properties of fusion Welded 304L Stainless Steel. 2004.
- [88] Saeid T, Abdollah-Zadeh A, Assadi H, Ghaini FM. Effect of friction stir welding speed on the microstructure and mechanical properties of a duplex stainless steel. *Materials Science and Engineering: A*. 2008;496(1-2):262-8.
- [89] Mishra RS, Ma Z, Charit I. Friction stir processing: a novel technique for fabrication of surface composite. *Materials Science and Engineering: A*. 2003;341(1-2):307-10.
- [90] Ma Z. Friction stir processing technology: a review. *Metallurgical and materials Transactions A*. 2008;39(3):642-58.
- [91] Mishra RS, Ma Z. Friction stir welding and processing. *Materials science and engineering: R: reports*. 2005;50(1-2):1-78.
- [92] International A. Standard test method for measurement of fatigue crack growth rates: ASTM International; 2011.
- [93] Stokes D. Principles and practice of variable pressure/environmental scanning electron microscopy (VP-ESEM): John Wiley & Sons; 2008.

- [94] Hurley P, Humphreys F. The application of EBSD to the study of substructural development in a cold rolled single-phase aluminium alloy. *Acta Materialia*. 2003;51(4): 1087-102.
- [95] Jesson D, Pennycook S. Incoherent imaging of crystals using thermally scattered electrons. *Proc R Soc Lond A*. 1995;449(1936):273-93.
- [96] Williams DB, Carter CB. The transmission electron microscope. *Transmission electron microscopy*: Springer; 1996. p. 3-17.
- [97] Ryum N. The influence of a precipitate-free zone on the mechanical properties of an Al-Mg-Zn alloy. *Acta Metallurgica*. 1968;16(3):327-32.
- [98] Murakami M, Kawano O, Murakami Y. The formation and reversion of guinier-preston zones in an aluminium-6.7 at.% zinc alloy and the effects of small concentrations of magnesium and silver. *Acta Metallurgica*. 1969;17(1):29-40.
- [99] Luo Z. Crystallography of SiC/MgAl<sub>2</sub>O<sub>4</sub>/Al interfaces in a pre-oxidized SiC reinforced SiC/Al composite. *Acta materialia*. 2006;54(1):47-58.
- [100] Kostka A, Lelatko J, Gigla M, Morawiec H, Janas A. TEM study of the interface in ceramic-reinforced aluminum-based composites. *Materials chemistry and physics*. 2003;81(2):323-5.
- [101] Ardell A. On the coarsening of grain boundary precipitates. *Acta Metallurgica*. 1972;20(4):601-9.
- [102] Unwin P, Nicholson R. The nucleation and initial stages of growth of grain boundary precipitates in Al-Zn-Mg and Al-Mg alloys. *Acta metallurgica*. 1969;17(11): 1379-93.
- [103] Ju X, Zhang F, Chen Z, Ji G, Wang M, Wu Y, et al. Microstructure of multi-pass friction-stir-processed Al-Zn-Mg-Cu Alloys reinforced by nano-Sized TiB<sub>2</sub> particles and the effect of T6 heat treatment. *Metals*. 2017;7(12):530.
- [104] Stadelmann P. JEMS JAVA electron microscopy software. [http://cimewww epfl ch/people/stadelmann/jemsWebSite/jems.html](http://cimewww.epfl.ch/people/stadelmann/jemsWebSite/jems.html). 2004.
- [105] Barthel J. Dr. Probe: A software for high-resolution STEM image simulation. *Ultramicroscopy*. 2018;193:1-11.
- [106] Momma K, Izumi F. VESTA 3 for three-dimensional visualization of crystal, volumetric and morphology data. *Journal of applied crystallography*. 2011;44(6):1272-6.
- [107] Ma S, Zhang P, Ji G, Chen Z, Sun G, Zhong S, et al. Microstructure and mechanical properties of friction stir processed Al-Mg-Si alloys dispersion-

strengthened by nanosized TiB<sub>2</sub> particles. *Journal of Alloys and Compounds*. 2014;616:128-36.

[108] Wulff G. On the question of speed of growth and dissolution of crystal surfaces. *Z Kristallogr*. 1901;34(5/6):449.

[109] Abdel-Hamid A, Hamar-Thibault S, Hamar R. Crystal morphology of the compound TiB<sub>2</sub>. *Journal of crystal growth*. 1985;71(3):744-50.

[110] Schumacher P, McKay B. TEM investigation of heterogeneous nucleation mechanisms in Al–Si alloys. *Journal of Non-Crystalline Solids*. 2003;317(1-2):123-8.

[111] Ellner M, Predel B. Neutron-diffraction analysis of ternary laves phases of the MgCu<sub>2</sub> type. *Journal of Solid State Chemistry*. 1979;30(2):209-21.

[112] Blavette D, Cadel E, Fraczkiewicz A, Menand A. Three-dimensional atomic-scale imaging of impurity segregation to line defects. *Science*. 1999;286(5448):2317-9.

[113] Thompson K, Flaitz PL, Ronsheim P, Larson DJ, Kelly TF. Imaging of arsenic Cottrell atmospheres around silicon defects by three-dimensional atom probe tomography. *Science*. 2007;317(5843):1370-4.

[114] Seitz F. On the generation of vacancies by moving dislocations. *Advances in Physics*. 1952;1(1):43-90.

[115] Sha G, Cerezo A. Kinetic Monte Carlo simulation of clustering in an Al–Zn–Mg–Cu alloy (7050). *Acta materialia*. 2005;53(4):907-17.

[116] Larché F, Cahn JW. Overview no. 41 the interactions of composition and stress in crystalline solids. *Acta metallurgica*. 1985;33(3):331-57.

[117] Huang J, Meyer M, Pontikis V. Is pipe diffusion in metals vacancy controlled? A molecular dynamics study of an edge dislocation in copper. *Physical review letters*. 1989;63(6):628.

[118] Rabier J, Puls M. Atomistic calculations of point-defect interaction and migration energies in the core of an edge dislocation in NaCl. *Philosophical Magazine A*. 1989;59(3):533-46.

[119] Eckert J, Holzer J, Johnson W. Thermal stability and grain growth behavior of mechanically alloyed nanocrystalline Fe-Cu alloys. *Journal of applied physics*. 1993;73(1):131-41.

[120] Wang Z, Shiflet G. Growth of  $\delta'$  on dislocations in a dilute Al-Li alloy. *Metallurgical and Materials Transactions A*. 1998;29(8):2073-85.

- [121] Ma K, Wen H, Hu T, Topping TD, Isheim D, Seidman DN, et al. Mechanical behavior and strengthening mechanisms in ultrafine grain precipitation-strengthened aluminum alloy. *Acta Materialia*. 2014;62:141-55.
- [122] Berg L, Gjønnnes J, Hansen V, Li X, Knutson-Wedel M, Waterloo G, et al. GP-zones in Al–Zn–Mg alloys and their role in artificial aging. *Acta materialia*. 2001; 49(17):3443-51.
- [123] Li X, Hansen V, Gjønnnes J, Wallenberg L. HREM study and structure modeling of the  $\eta'$  phase, the hardening precipitates in commercial Al–Zn–Mg alloys. *Acta materialia*. 1999;47(9):2651-9.
- [124] Martin JW, Martin JW, Doherty RD, Cantor B. *Stability of microstructure in metallic systems*: Cambridge University Press; 1997.
- [125] Zhang M-X, Kelly P, Easton M, Taylor J. Crystallographic study of grain refinement in aluminum alloys using the edge-to-edge matching model. *Acta Materialia*. 2005;53(5):1427-38.
- [126] Kelly P, Ren H-P, Qiu D, Zhang M-X. Identifying close-packed planes in complex crystal structures. *Acta Materialia*. 2010;58(8):3091-5.
- [127] Liu Z, Qiu D, Wang F, Taylor JA, Zhang M. The grain refining mechanism of cast zinc through silver inoculation. *Acta Materialia*. 2014;79:315-26.
- [128] Zhang W-Z, Purdy G. O-lattice analyses of interfacial misfit. I. General considerations. *Philosophical Magazine A*. 1993;68(2):279-90.
- [129] Zhang W-Z, Weatherly G. A comparative study of the theory of the O-lattice and the phenomenological theory of martensite crystallography to phase transformations. *Acta materialia*. 1998;46(6):1837-47.
- [130] Valiev R. Materials science: nanomaterial advantage. *Nature*. 2002;419(6910): 887.
- [131] Lu K, Lu L, Suresh S. Strengthening materials by engineering coherent internal boundaries at the nanoscale. *science*. 2009;324(5925):349-52.
- [132] Liu G, Zhang G, Jiang F, Ding X, Sun Y, Sun J, et al. Nanostructured high-strength molybdenum alloys with unprecedented tensile ductility. *Nature materials*. 2013;12(4):344-50.
- [133] Wang Y, Chen M, Zhou F, Ma E. High tensile ductility in a nanostructured metal. *Nature*. 2002;419(6910):912-5.
- [134] Lu K. Making strong nanomaterials ductile with gradients. *Science*. 2014; 345(6203):1455-6.

- [135] Jia D, Wang Y, Ramesh K, Ma E, Zhu Y, Valiev R. Deformation behavior and plastic instabilities of ultrafine-grained titanium. *Applied Physics Letters*. 2001;79(5): 611-3.
- [136] Zhao Y, Liao X, Jin Z, Valiev R, Zhu YT. Microstructures and mechanical properties of ultrafine grained 7075 Al alloy processed by ECAP and their evolutions during annealing. *Acta Materialia*. 2004;52(15):4589-99.
- [137] Tellkamp V, Lavernia E, Melmed A. Mechanical behavior and microstructure of a thermally stable bulk nanostructured Al alloy. *Metallurgical and Materials Transactions A*. 2001;32(9):2335-43.
- [138] Zha M, Li Y, Mathiesen RH, Bjørge R, Roven HJ. Microstructure evolution and mechanical behavior of a binary Al–7Mg alloy processed by equal-channel angular pressing. *Acta Materialia*. 2015;84:42-54.
- [139] Kempen K, Thijs L, Van Humbeeck J, Kruth J-P. Mechanical properties of AlSi10Mg produced by selective laser melting. *Physics Procedia*. 2012;39:439-46.
- [140] Martin JH, Yahata BD, Hundley JM, Mayer JA, Schaedler TA, Pollock TM. 3d printing of high-strength aluminium alloys. *Nature*. 2017;549(7672):365-9.
- [141] Shang JK, Ritchie R. On the particle-size dependence of fatigue-crack propagation thresholds in SiC-particulate-reinforced aluminum-alloy composites: role of crack closure and crack trapping. *Acta metallurgica*. 1989;37(8):2267-78.
- [142] Wei H, Li Z, Xiong D-B, Tan Z, Fan G, Qin Z, et al. Towards strong and stiff carbon nanotube-reinforced high-strength aluminum alloy composites through a microlaminated architecture design. *Scripta Materialia*. 2014;75:30-3.
- [143] Xu R, Tan Z, Fan G, Ji G, Xiong D-B, Guo Q, et al. High-strength CNT/Al-Zn-Mg-Cu composites with improved ductility achieved by flake powder metallurgy via elemental alloying. *Composites Part A: Applied Science and Manufacturing*. 2018;111: 1-11.
- [144] Viswanathan U, Dey G, Asundi M. Precipitation hardening in 350 grade maraging steel. *Metallurgical Transactions A*. 1993;24(11):2429-42.
- [145] Jiang S, Wang H, Wu Y, Liu X, Chen H, Yao M, et al. Ultrastrong steel via minimal lattice misfit and high-density nanoprecipitation. *Nature*. 2017;544(7651): 460-4.
- [146] Petch N. The Cleavage Strength of Polycrystals. *J of the Iron and Steel Inst*. 1953; 174:25-8.

- [147] Kim C-S, Sohn I, Nezafati M, Ferguson J, Schultz BF, Bajestani-Gohari Z, et al. Prediction models for the yield strength of particle-reinforced unimodal pure magnesium (Mg) metal matrix nanocomposites (MMNCs). *Journal of Materials Science*. 2013;48(12):4191-204.
- [148] Zhang Z, Chen D. Consideration of Orowan strengthening effect in particulate-reinforced metal matrix nanocomposites: a model for predicting their yield strength. *Scripta Materialia*. 2006;54(7):1321-6.
- [149] Ashby M. The deformation of plastically non-homogeneous materials. *Philosophical Magazine*. 1970;21(170):399-424.
- [150] Brown L. Precipitation and dispersion hardening. *Strength of metals and alloys*: Elsevier; 1980. p. 1551-71.
- [151] Nair S, Tien J, Bates R. SiC-reinforced aluminium metal matrix composites. *International Metals Reviews*. 1985;30(1):275-90.
- [152] Venkataraman B, Sundararajan G. The sliding wear behaviour of Al-SiC particulate composites—I. Macrobehaviour. *Acta Materialia*. 1996;44(2):451-60.
- [153] Venkataraman B, Sundararajan G. The sliding wear behaviour of Al-SiC particulate composites—II. The characterization of subsurface deformation and correlation with wear behaviour. *Acta Materialia*. 1996;44(2):461-73.
- [154] Rohatgi P, Alaraj S, Thakkar R, Daoud A. Variation in fatigue properties of cast A359-SiC composites under total strain controlled conditions: effects of porosity and inclusions. *Composites Part A: Applied Science and Manufacturing*. 2007;38(8):1829-41.
- [155] Nardone V, Prewo K. On the strength of discontinuous silicon carbide reinforced aluminum composites. *Scripta Metallurgica*. 1986;20(1):43-8.
- [156] Huang M, Li X, Yi H, Ma N, Wang H. Effect of in situ TiB<sub>2</sub> particle reinforcement on the creep resistance of hypoeutectic Al–12Si alloy. *Journal of alloys and compounds*. 2005;389(1-2):275-80.
- [157] Yi H, Ma N, Li X, Zhang Y, Wang H. High-temperature mechanics properties of in situ TiB<sub>2</sub>p reinforced Al–Si alloy composites. *Materials Science and Engineering: A*. 2006;419(1-2):12-7.
- [158] Healy J, Beevers C. A study of fatigue crack growth in a particulate-reinforced Al-Si alloy at 23 and 220° C. *Materials Science and Engineering: A*. 1991;142(2):183-92.

- [159] Sugimura Y, Suresh S. Effects of SiC content on fatigue crack growth in. *Metallurgical Transactions A*. 1992;23(8):2231-42.
- [160] Kumai S, Yoshida K, Higo Y, Nunomura S. Effects of the particle distribution on fatigue crack growth in particulate SiC/6061 aluminium alloy composites. *International journal of fatigue*. 1992;14(2):105-12.
- [161] Kumai S, Hu J, Higo Y, Nunomura S. Effects of dendrite cell size and particle distribution on the near-threshold fatigue crack growth behaviour of cast Al-SiCp composites. *Acta materialia*. 1996;44(6):2249-57.
- [162] Ritchie RO. Mechanisms of fatigue-crack propagation in ductile and brittle solids. *International Journal of Fracture*. 1999;100(1):55-83.
- [163] Davidson DL. Small and large fatigue cracks in aluminum alloys. *Acta Metallurgica*. 1988;36(8):2275-82.
- [164] Peters P, Xia Z, Hemptenmacher J, Assler H. Influence of interfacial stress transfer on fatigue crack growth in SiC-fibre reinforced titanium alloys. *Composites Part A: Applied Science and Manufacturing*. 2001;32(3-4):561-7.
- [165] Davidson DL. The effect of particulate SiC on fatigue crack growth in a cast-extruded aluminum alloy composite. *Metallurgical Transactions A*. 1991;22(1):97-112.
- [166] Davidson D. Fracture characteristics of Al-4 pct Mg mechanically alloyed with SiC. *Metallurgical Transactions A*. 1987;18(12):2115-28.
- [167] Chen Z, Tokaji K. Effects of particle size on fatigue crack initiation and small crack growth in SiC particulate-reinforced aluminium alloy composites. *Materials Letters*. 2004;58(17-18):2314-21.
- [168] Brechet Y, Embury J, Tao S, Luo L. Damage initiation in metal matrix composites. *Acta Metallurgica et Materialia*. 1991;39(8):1781-6.
- [169] Ayyar A, Chawla N. Microstructure-based modeling of crack growth in particle reinforced composites. *Composites Science and technology*. 2006;66(13):1980-94.
- [170] Chen Z, Tokaji K, Minagi A. Particle size dependence of fatigue crack propagation in SiC particulate-reinforced aluminium alloy composites. *Journal of materials science*. 2001;36(20):4893-902.
- [171] Lu L, Lai M, Chen F. Al-4 wt% Cu composite reinforced with in-situ TiB<sub>2</sub> particles. *Acta Materialia*. 1997;45(10):4297-309.
- [172] Lakshmi S, Lu L, Gupta M. In situ preparation of TiB<sub>2</sub> reinforced Al based composites. *Journal of materials processing technology*. 1998;73(1-3):160-6.

- [173] Mandal A, Chakraborty M, Murty B. Ageing behaviour of A356 alloy reinforced with in-situ formed TiB<sub>2</sub> particles. *Materials Science and Engineering: A*. 2008;489(1-2):220-6.
- [174] Chen F, Chen Z, Mao F, Wang T, Cao Z. TiB<sub>2</sub> reinforced aluminum based in situ composites fabricated by stir casting. *Materials Science and Engineering: A*. 2015;625:357-68.
- [175] Gao Q, Wu S, Shulin L, Duan X, An P. Preparation of in-situ 5 vol% TiB<sub>2</sub> particulate reinforced Al-4.5 Cu alloy matrix composites assisted by improved mechanical stirring process. *Materials & Design*. 2016;94:79-86.
- [176] Wang F, Xu J, Li J, Li X, Wang H. Fatigue crack initiation and propagation in A356 alloy reinforced with in situ TiB<sub>2</sub> particles. *Materials & Design*. 2012;33:236-41.
- [177] Wang F, Meng X, Ma N, Xu J, Li X, Wang H. The relationship between TiB<sub>2</sub> volume fraction and fatigue crack growth behavior in the in situ TiB<sub>2</sub>/A356 composites. *Journal of Materials Science*. 2012;47(7):3361-6.
- [178] Marlaud T, Deschamps A, Bley F, Lefebvre W, Baroux B. Evolution of precipitate microstructures during the retrogression and re-ageing heat treatment of an Al-Zn-Mg-Cu alloy. *Acta materialia*. 2010;58(14):4814-26.
- [179] Pastor H, Matkovich V. Boron and refractory borides. Springer-Verlag, New York, 1977) p. 1977;457.
- [180] Mondolfo LF. Aluminum alloys: structure and properties: Elsevier; 2013.
- [181] Geng J, Hong T, Ma Y, Wang M, Chen D, Ma N, et al. The solution treatment of in-situ sub-micron TiB<sub>2</sub>/2024 Al composite. *Materials & Design*. 2016;98:186-93.
- [182] Paris P, Erdogan F. A critical analysis of crack propagation laws. *Journal of basic engineering*. 1963;85(4):528-33.
- [183] Hornbogen E, Zum Gahr K-H. Microstructure and fatigue crack growth in a  $\gamma$ -Fe-Ni-Al alloy. *Acta Metallurgica*. 1976;24(6):581-92.
- [184] Lindigkeit J, Terlinde G, Gysler A, Lütjering G. The effect of grain size on the fatigue crack propagation behavior of age-hardened alloys in inert and corrosive environment. *Acta Metallurgica*. 1979;27(11):1717-26.
- [185] Knott JF. Fundamentals of fracture mechanics: Gruppo Italiano Frattura; 1973.
- [186] Srivatsan T. The low-cycle fatigue behaviour of an aluminium-alloy-ceramic-particle composite. *International journal of fatigue*. 1992;14(3):173-82.
- [187] Wallin K, Saario T, Törrönen K. Fracture of brittle particles in a ductile matrix. *International journal of fracture*. 1986;32(3):201-9.

- [188] Hunt Jr W, Brockenbrough J, Magnusen P. An Al-Si-Mg composite model system: microstructural effects on deformation and damage evolution. *Scripta metallurgica et materialia*. 1991;25(1):15-20.
- [189] Beachem C, Yoder G. Elastic-plastic fracture by homogeneous microvoid coalescence tearing along alternating shear planes. *Metallurgical Transactions*. 1973; 4(4):1145-53.
- [190] Li H, Ebrahimi F. Ductile-to-Brittle Transition in Nanocrystalline Metals. *Advanced Materials*. 2005;17(16):1969-72.
- [191] Ritchie R, Knott J. Mechanisms of fatigue crack growth in low alloy steel. *Acta Metallurgica*. 1973;21(5):639-48.
- [192] Ritchie RO, Horn R. Further considerations on the inconsistency in toughness evaluation of AISI 4340 steel austenitized at increasing temperatures. *Metallurgical Transactions A*. 1978;9(3):331-41.

# Index of Abbreviations

| Abbreviation | Meaning                           |
|--------------|-----------------------------------|
| ADF          | Annular dark-field                |
| AM           | Additively manufactured           |
| BG           | Bimodal grain                     |
| Coml.        | Commercial                        |
| CG           | Coarse grain                      |
| CNT          | Carbon nano-tube                  |
| CPZ          | Coarse precipitate zone           |
| CS           | Cyclic strengthening processed    |
| CT           | Compact tension                   |
| CTOD         | Crack tip open displace           |
| EBSD         | Electron backscatter diffraction  |
| ED           | Extrusion direction               |
| EDS          | Energy dispersive spectrometer    |
| EELS         | Electron energy loss spectroscopy |
| EFTEM        | Energy filtered TEM               |
| ESD          | Extra super duralumin             |
| FCG          | Fatigue crack growth              |
| FFT          | Fast Fourier transform            |
| FGZ          | Fully-grown zone                  |
| FSP          | Friction stir processing          |
| GB           | Grain boundary                    |
| GP           | Guinier-Preston                   |

|                  |   |
|------------------|---|
| HAADF            | High-angle annular dark-field                             |
| HGZ              | Half-grown zone   |
| HRSTEM           | High-resolution scanning transmission electron microscopy |
| IP               | Interface precipitate                                     |
| MMC              | Metal matrix composite                                    |
| MRP              | Micron- (or submicron-)sized reinforcement particle       |
| NC               | Nanocrystalline   |
| NRP              | Nanosized reinforcement particle                          |
| OR               | Orientation relationship                                  |
| PAIS             | Precipitation assisted interface strengthening            |
| PFZ              | Precipitate free zone                                     |
| RP               | Reinforcement particle                                    |
| rpm              | Revolutions per minute                                    |
| SCC              | Stress corrosion cracking                                 |
| SEM              | Scanning electron microscopy                              |
| SLM              | Selective laser melting                                   |
| SSS              | Supersaturated solid solution                             |
| TEM              | Transmission electron microscopy                          |
| TSID             | Thermoelastic stress induced dislocation                  |
| UFG              | Ultra-fine grain  |
| VLS              | Vapor-liquid-solid  |
| XD <sup>TM</sup> | Exothermic dispersion                                     |
| XLPA             | X-ray line profile analysis                               |
| 2DC              | Two-dimensional compound                                  |
| $\Delta K$       | Stress intensity factor                                   |

# Acknowledgements

First and foremost, I sincerely gratitude to my supervisors Prof. Vincent Ji and Dr. Gang Ji, for their continual guidance, inspiration and support over the years. They have instilled in me a sense of what it means to do real science, and they will always remain a role model for me.

I would like to thank all the jury members for taking time out of their schedules to achieve my doctoral dissertation defense, and special gratitude to Dr. Jean-François Silvain and Dr. Rajashekhara Shabadi to review my dissertation and provide the suggestions and comments.

I would also like to thank Dr. Ahmed Addad, Dr. Zhe Chen, Prof. Ming-Xing Zhang, Dr. Williams Lefebvre and Prof. Johan Verbeeck for their great help in my research.

Thanks to the members of my research group. I am honored to have had the opportunity to work with such a brilliant group of researchers. They shared their experiences with me and offered help in my daily life, especially to Dr. Chengyi Dan, Dr. Run Xu, Dr. Peng Yao, Dr. Romain Candela, Dr. Devadas Bhat Panemangalore, Dr. Gabriel Bouobda, Dr. Sabrina Macaluso, Dr. Linwei LI and Dr. Bin Wang.

I gratefully acknowledge the financial support of China Scholarship Council (Grant No. 201606230212), Conseil Regional du Nord-Pas de Calais and the European Regional Development Fund (ERDF), Microscopie Electronique et Sonde Atomique (METSA) and Enabling Science and Technology through European Electron Microscopy (ESTEEM2).

Finally, I am forever grateful to my friends and family. Thanks to my parents, my brother and my friends for their constant love and support. Particularly, I owe most gratitude to Lu for inspiring me to be a better person, and for sticking by me no matter what through our transcontinental and trans-Atlantic separation.

# Résumé en Français

## Chapitre 1 Introduction générale

Suite au développement rapide de l'industrie aérospatiale et automobile, des exigences plus sévères, telles qu'une rigidité plus élevée, une haute résistance mécanique et une bonne résistance contre la fissuration en fatigue (FCG), ont été formulées. Parallèlement aux développements des nanotechnologies, des particules de renforts nanométriques (NRPs) ont été introduites dans les alliages d'aluminium (Al) afin de répondre aux exigences croissantes des applications industrielles. On s'attend à ce que les NPR introduites auront un effet positif sur les précipitations interfaciales et, par conséquent, sur les propriétés mécaniques macroscopiques des composites à base d'aluminium, ce qui a soulevé des problèmes fondamentaux importants qui restent à résoudre.

Dans cette optique, la présente thèse vise à fournir un aperçu fondamental des effets des NRPs sur les précipitations interfaciales, les propriétés mécaniques des composites à base d'aluminium. Pour atteindre ces objectifs, un matériau composite à matrice d'alliage d'aluminium Al-Zn-Mg-Cu renforcé à 6 % en poids de nanoparticules de  $\text{TiB}_2$  (nanocomposite  $\text{TiB}_2/\text{Al-Zn-Mg-Cu}$ ) a été conçu, produit et étudié afin d'étudier les effets des NRPs sur la précipitation interfaciale, les propriétés en traction et la résistance de FCG des composites à base Al.

## Chapitre 2 Etude bibliographique

Le chapitre 2 résume l'histoire du développement des composites à matrice d'aluminium et les réactions de précipitation des alliages d'Al-Zn-Mg(-Cu). Les informations essentielles sur la phase de renforcement de  $\text{TiB}_2$ , les composites  $\text{TiB}_2/\text{Al}$  et les caractéristiques interfaciales  $\text{TiB}_2/\text{Al}$  ont été synthétisées.

## Chapitre 3 Méthodologie de la recherche

### 3.1 Traitement des matériaux

Les lingots des nanocomposites  $\text{TiB}_2/\text{Al-Zn-Mg-Cu}$  ont été fabriqués par coulée réactionnelle au sel mixte. Par la suite, pour les études sur les effets des nanoparticules

de  $\text{TiB}_2$  sur la précipitation interfaciale et sur les propriétés de traction, les lingots ont été soumis à un traitement par friction (FSP) suivi par une extrusion à chaud. Pour les études des effets des nanoparticules de  $\text{TiB}_2$  sur la propriété de FCG du nanocomposite  $\text{TiB}_2/\text{Al-Zn-Mg-Cu}$ , les lingots ont été directement soumis à une extrusion à chaud afin de répondre aux exigences dimensionnelles des échantillons C(T) en raison de la taille limitée de la zone pépite après FSP.

Ensuite, des traitements thermiques, tel que le traitement à solution solide (477 °C/70 min + trempé à l'eau), le traitement thermique T6 (477 °C/70 min + trempé à l'eau + 120 °C/24h) et le traitement thermique T76 (477 °C/70 min + trempé à l'eau + 120 °C/5h + 160 °C/18h) ont été réalisés sur les échantillons non extrudés.

### **3.2 Méthodes d'essais mécaniques**

Les échantillons en état de solution solide et en état de vieillissement maximal (T6) ont été utilisés pour les essais de traction. L'essai de traction a été effectué sur un appareil Zwick/Roell Z100 à température ambiante. Les échantillons en état T76 ont été utilisés pour les tests de FCG. Les essais de FCG ont été effectués sur la machine d'essai servohydraulique MTS 809 en température ambiante et sous l'air du laboratoire.

### **3.3 Méthodes de caractérisation**

La microscopie électronique à balayage (SEM), la diffraction de rétrodiffusion des électrons (EBSD) et la microscopie électronique en transmission à haute résolution (HRSTEM) ont été utilisées pour la caractérisation de la microstructure des échantillons en solution solide, en phase de vieillissement maximal (T6) et en phase survieillée (T74).

## **Chapitre 4 Étude à l'échelle atomique des précipitations interfaciales dans le nanocomposite $\text{TiB}_2/\text{Al-Zn-Mg-Cu}$**

### **4.1 Résultats**

#### **4.1.1 Structure de l'interface $\text{TiB}_2/\text{Al}$ à l'état trempé**

En raison de l'efficacité du FSP, la majorité des nanoparticules de  $\text{TiB}_2$  sont uniformément dispersées à l'intérieur des grains fins équiaxes d'Al (Fig. 4.1a). En état solide, l'interface  $\text{TiB}_2/\text{Al}$  est étroitement liée et exempte de particules d'oxyde, sans dislocations thermoélastiques apparentes induites par contrainte thermoélastique (TSIDs) observée dans la matrice environnante (Fig. 4.1b). Les nanoparticules de  $\text{TiB}_2$

présentent les facettes basales  $\{0001\}$ , prismatique  $\{01\bar{1}0\}$  et pyramidale  $\{01\bar{1}1\}$  (Fig. 4.1b et c).

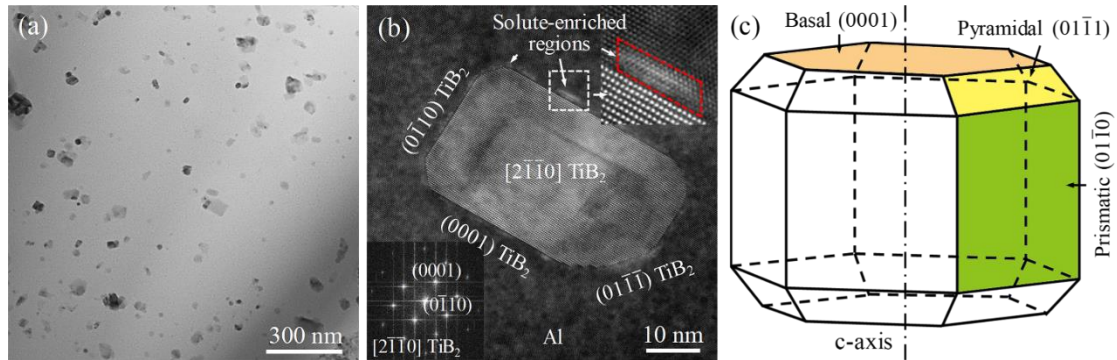


Fig. 4.1 (a) Image TEM à champ clair montrant la distribution des nanoparticules de  $\text{TiB}_2$  dans les grains de la matrice Al-Zn-Mg-Cu en état trempé, (b) Image STEM-HAADF montrant une interface  $\text{TiB}_2/\text{Al}$  typique et (c) dessin schématique illustrant la forme à facettes des nanoparticules de  $\text{TiB}_2$ . La clichée de diffraction électronique en (b) en bas à gauche et l'image en haut à droite mettent en évidence le motif FFT correspondant des interfaces de nanoparticules de  $\text{TiB}_2$  et de Cottrell situées à l'interface  $\text{TiB}_2/\text{Al}$ .

Les relations d'orientation bien documentée (OR)1 :  $[2\bar{1}\bar{1}0]_{\text{TiB}_2}/[101]_{\text{Al}}$ ,  $(0001)_{\text{TiB}_2}/(\bar{1}11)_{\text{Al}}$  et le nouveau OR2 :  $[2\bar{1}\bar{1}0]_{\text{TiB}_2}/[101]_{\text{Al}}$ ,  $(01\bar{1}0)_{\text{TiB}_2}/(11\bar{1})_{\text{Al}}$  entre les nanoparticules de  $\text{TiB}_2$  et la matrice d'Al sont déterminées (Fig. 4.2). Notamment, la majorité des nanoparticules de  $\text{TiB}_2$  ont des OR1 avec la matrice d'Al. Les dislocations d'inadaptation périodiquement espacées présentent aux interfaces  $\text{TiB}_2/\text{Al}$ . La cohérence de l'interface  $\text{TiB}_2/\text{Al}$  est acquise. A la condition d'OR1, l'inadéquation de l'interface  $\text{TiB}_2/\text{Al}$  parallèle à la facette basale  $\{0001\}$ , prismatique  $\{01\bar{1}0\}$  et pyramidale  $\{01\bar{1}1\}$  est respectivement de 5.87 %, 38.03 % et 38.03 %. A la condition d'OR2, l'inadéquation de l'interface  $\text{TiB}_2/\text{Al}$  parallèle à la facette basale  $\{0001\}$ , prismatique  $\{01\bar{1}0\}$  et pyramidale  $\{01\bar{1}1\}$  est de 11.97 %, 11.97 % et 22.90 %, respectivement.

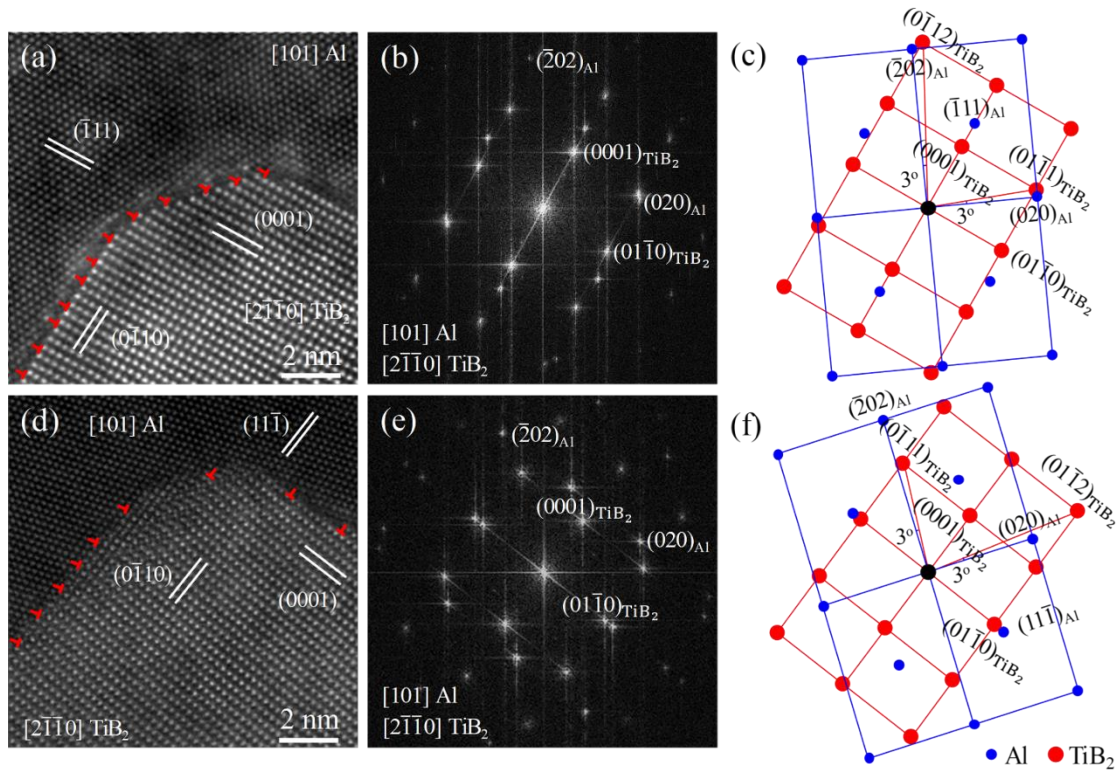


Fig. 4.2 (a) et (d) Images HRSTEM-HAADF montrant les structures d'interface  $\text{TiB}_2/\text{Al}$  aux conditions d'OR1 et OR2, respectivement, (b) et (e) les modèles FFT correspondants de (a) et (d), et (c) et (f) les modèles simulés correspondants d'indexation, respectivement. La direction de projection est  $[2\bar{1}\bar{1}0]_{\text{TiB}_2}/[101]_{\text{Al}}$ .

#### 4.1.2 Les structures de l'interface $\text{TiB}_2/\text{Al}$ à l'état de vieillissement/OR1

À l'état de vieillissement/OR1, une densité élevée de nano-précipités distribuées de manière homogène est observée dans la matrice d'aluminium en dehors des interfaces  $\text{TiB}_2/\text{Al}$  (Fig. 4.3a), y compris les zones de GP en forme de plaques (Fig. 4.3b) et la phase allongée  $\eta'$  (Fig. 4.3c). Les deux zones de GP et la phase  $\eta'$  sont totalement cohérentes avec la matrice d'Al. La précipitation dans la matrice de l'alliage d'Al loin des nanoparticules de  $\text{TiB}_2$  est la même que celle des alliages Al-Zn-Mg-Cu non renforcés. Selon la Fig. 4.3d, aucune CPZ ou PFZ perceptible n'a été trouvée à proximité de nanoparticules de  $\text{TiB}_2$ . Les précipités d'interface (interphase, abréviation IP) couvrant les facettes prismatiques  $\{01\bar{1}0\}$  et pyramidales  $\{01\bar{1}1\}$  des nanoparticules de  $\text{TiB}_2$  sont visibles. Les angles de contact entre les interphases et le substrat  $\text{TiB}_2$  sont mesurés à  $60^\circ$ . L'interphase est identifiée comme étant la phase  $(\text{Zn}_{1.5}\text{Cu}_{0.5})\text{Mg}$ .

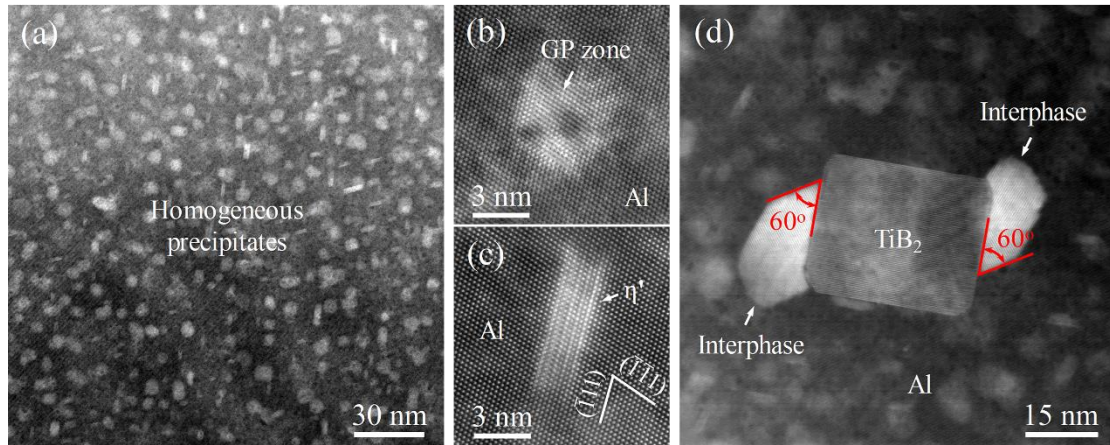


Fig. 4.3 (a) Images STEM-HAADF montrant les précipités homogènes dans la matrice loin de l'interface à l'état de vieillissement. Les images HRSTEM-HAADF mettent en évidence (b) la zone GP en forme de plaque et (c) la phase  $\eta'$  allongée en (a). (d) Images STEM-HAADF montrant des précipités hétérogènes aux interfaces  $\text{TiB}_2/\text{Al}$ . La direction de projection est  $[101]_{\text{Al}}$ .

Le OR entre l'interphase et la matrice Al d'OR3 :  $[1\bar{1}00]_{\text{IP}}//[101]_{\text{Al}}$ ,  $(11\bar{2}4)_{\text{IP}}//(11\bar{1})_{\text{Al}}$ ,  $(\bar{1}\bar{1}20)_{\text{IP}}$   $3^\circ$  de  $(\bar{2}02)_{\text{Al}}$ ,  $(0008)_{\text{IP}}$   $3^\circ$  de  $(020)_{\text{Al}}$  et le OR entre  $\text{TiB}_2$  et l'interphase d'OR4 :  $[2\bar{1}\bar{1}0]_{\text{TiB}_2}//[1\bar{1}00]_{\text{IP}}$ ,  $(01\bar{1}1)_{\text{TiB}_2}//(0008)_{\text{IP}}$ ,  $(01\bar{1}0)_{\text{TiB}_2}//(11\bar{2}8)_{\text{IP}}$  sont révélés (Fig. 4.4).

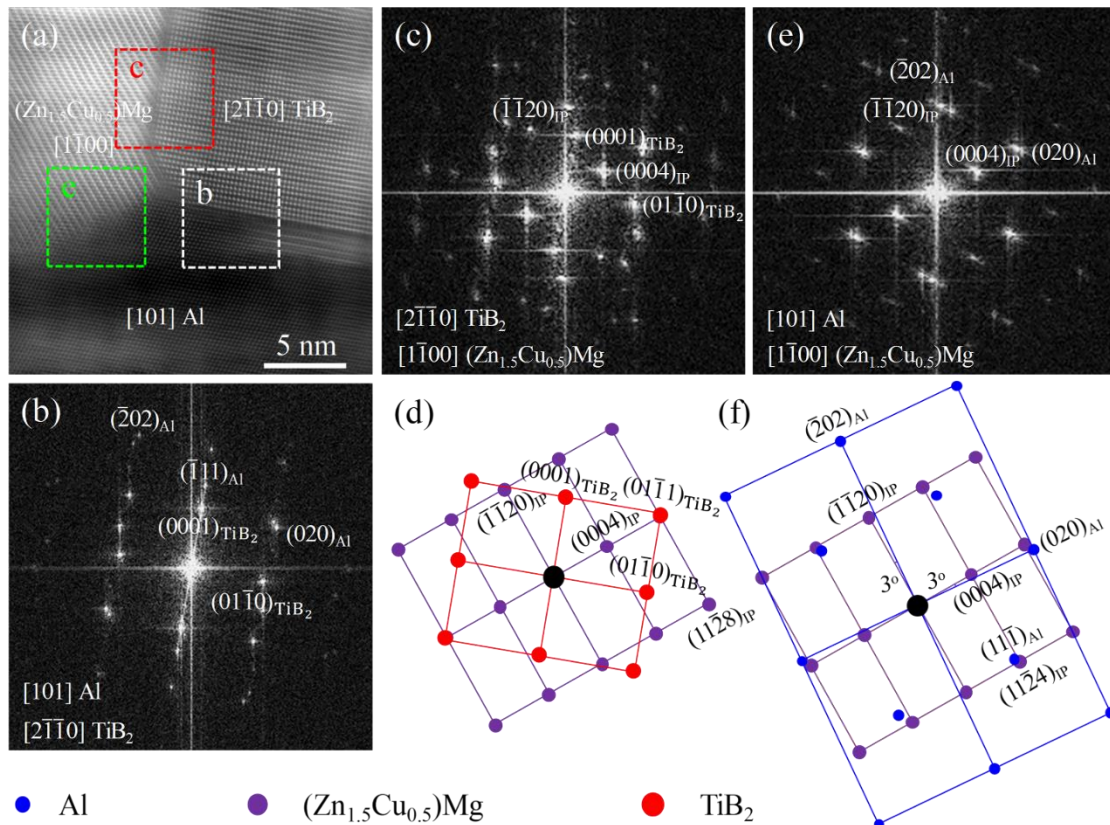


Fig. 4.4 (a) Image HRSTEM-HAADF montrant les multi-interfaces Al/IP/TiB<sub>2</sub> au niveau de l'OR1 ; (b), (c) et (e) motifs FFT correspondants des zones de boîtes à savoir b, c et e donnés dans (a) montrant les ORs mutuelles entre la nanoparticule TiB<sub>2</sub>, l'interphase et la matrice d'Al ; (d) et (f) motifs simulés correspondant respectivement aux (c) et (e). La direction de projection est  $[2\bar{1}\bar{1}0]_{\text{TiB}_2} // [1\bar{1}00]_{\text{IP}} // [101]_{\text{Al}}$ .

La structure atomique des interfaces multiples Al/(Zn<sub>1.5</sub>Cu<sub>0.5</sub>)Mg interphase/TiB<sub>2</sub> est caractérisée. Selon la Fig. 4.5, l'interphase croît sur la base des plans (0008)<sub>IP</sub> dans la direction de croissance  $\langle 0001 \rangle_{\text{IP}}$ . Elle comprend une zone en demi-granulés (HGZ) sur le front de croissance et une zone en pleine croissance (FGZ) à côté de celle-ci. Les interfaces Al/interphase sont composées de (020)<sub>Al</sub>//(0008)<sub>IPHGZ</sub>, (11 $\bar{1}$ )<sub>Al</sub>//(11 $\bar{2}$ 4)<sub>IPFGZ/HGZ</sub>, and ( $\bar{2}$ 02)<sub>Al</sub>  $3^\circ$  de ( $\bar{1}\bar{1}$ 20)<sub>IPFGZ/HGZ</sub> planes, et leur interface n'est pas adaptée à 0 %, 0.08 % et 3.31 %, respectivement. Selon la Fig. 4.6, les interfaces interphase/TiB<sub>2</sub> sont composées de (11 $\bar{2}$ 8)<sub>IPFGZ</sub>//(01 $\bar{1}$ 0)<sub>TiB2</sub> et (0008)<sub>IPFGZ</sub>//(01 $\bar{1}$ 1)<sub>TiB2</sub> planes, et leur inadadaptation d'interface est donc de 2.94 % et de 60.74 %, respectivement.

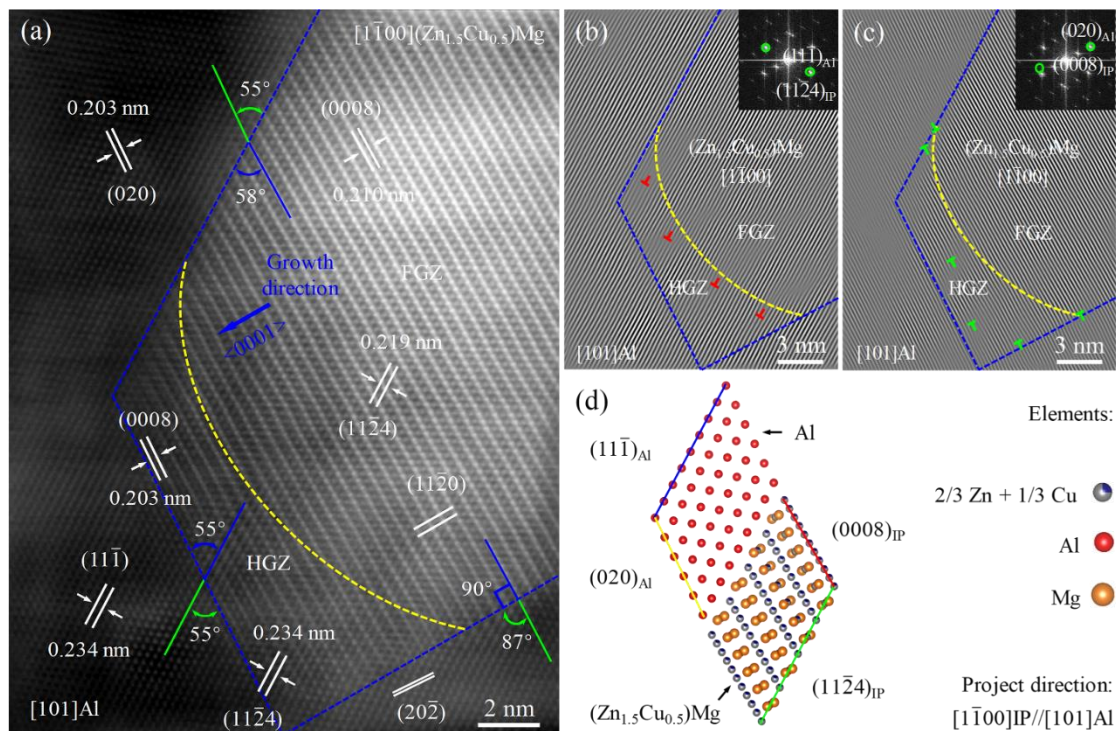


Fig. 4.5 (a) Image HRSTEM-HAADF montrant la structure atomique des interfaces Al/IP au niveau de l'OR1. (b) et (c) des motifs FFT inverses de (a) utilisant de différentes paires de réflexions sélectionnées dans des motifs FFT correspondants et (d) un modèle de structure atomique simulé montrant l'interface Al/IP (11 $\bar{1}$ )<sub>Al</sub>//(11 $\bar{2}$ 4)<sub>IP</sub>. La direction de projection est  $[1\bar{1}00]_{\text{IP}} // [101]_{\text{Al}}$ .

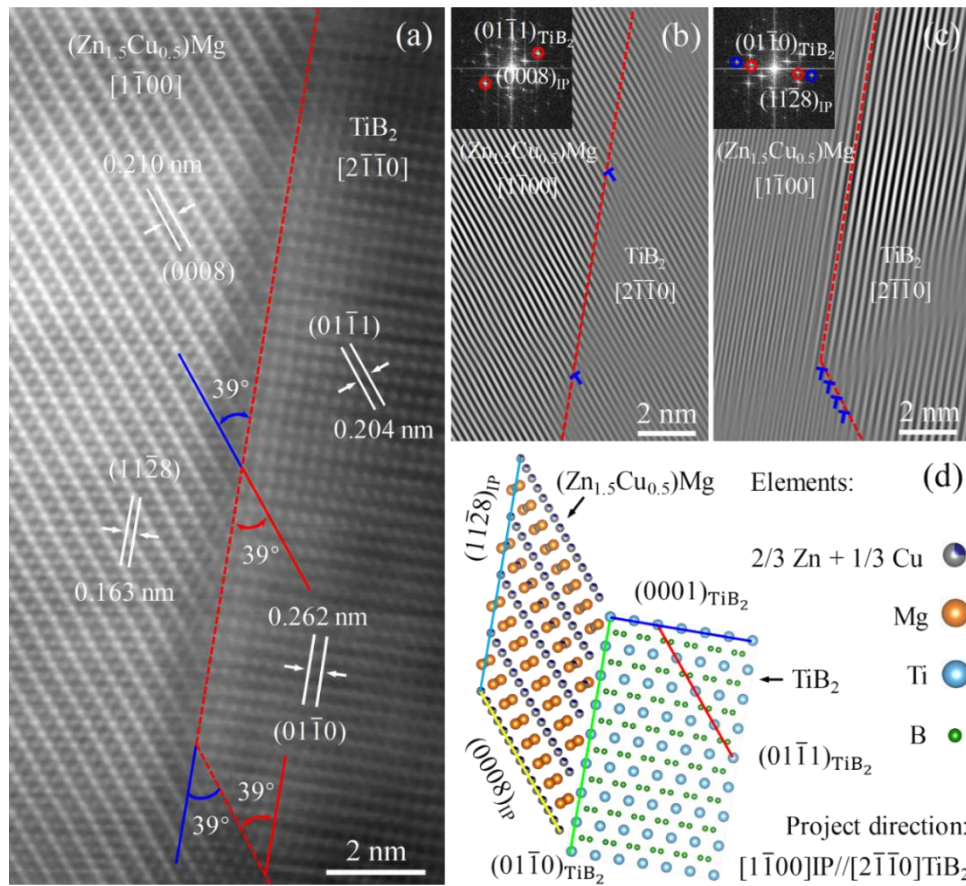


Fig. 4.6 (a) Image HRSTEM-HAADF montrant la structure atomique des interfaces IP/ $\text{TiB}_2$  au niveau OR1. (b) et (c) motifs FFT inverses de (a) l'utilisation de différentes paires de réflexions sélectionnées dans des motifs FFT correspondants dans des inlays et (d) modèle de structure atomique simulé montrant l'interface IP/ $\text{TiB}_2$   $(11\bar{2}8)_{\text{IP}} // (01\bar{1}0)_{\text{TiB}_2}$ . La direction de projection est  $[2\bar{1}\bar{1}0]_{\text{TiB}_2} // [1\bar{1}00]_{\text{IP}}$ .

#### 4.1.3 Les structures d'interface $\text{TiB}_2/\text{Al}$ à l'état sur vieillissement/OR2

A l'état sur vieillissement/OR2, les précipités très denses de type  $\eta$  se répartissent uniformément dans la matrice à l'écart des nanoparticules de  $\text{TiB}_2$  (Fig. 4.7a). La phase  $\eta$  est semi-cohérente avec la matrice en alliage d'aluminium (Fig. 4.7b et c). La précipitation dans la matrice de l'alliage d'Al loin des nanoparticules de  $\text{TiB}_2$  est également la même que celle des alliages Al-Zn-Mg-Cu non renforcés. Selon la Fig. 4.7d, aucune CPZ ou PFZ évidente n'est encore observée dans la matrice environnante des nanoparticules  $\text{TiB}_2$ . Les interphases précipitées aux facettes basales  $\{0001\}$  des nanoparticules de  $\text{TiB}_2$  sont visibles. Les angles de contact entre les interphases et le substrat  $\text{TiB}_2$  sont mesurés à  $60^\circ$ . L'interphase est également identifiée comme étant la phase  $(\text{Zn}_{1.5}\text{Cu}_{0.5})\text{Mg}$ .

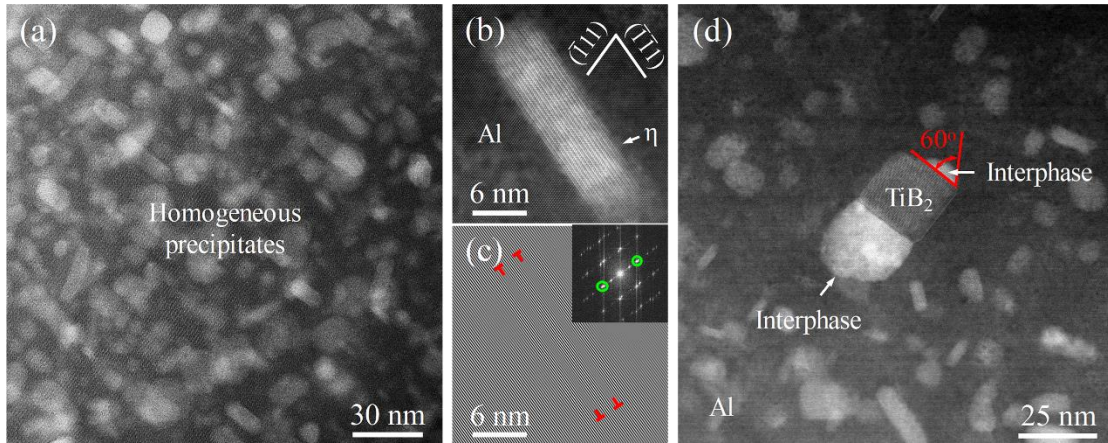


Fig. 4.7 (a) Images STEM-HAADF montrant les précipités homogènes dans la matrice loin de l'interface à l'état sur vieillissement. (b) Image HRSTEM-HAADF mettant en évidence la phase présente sur l'image (a) et (c) de la phase FFT inverse correspondante de (b) montrant les dislocations d'inadaptation aux interfaces Al/η. (d) Image STEM-HAADF montrant les précipités hétérogènes aux interfaces TiB<sub>2</sub>/Al à l'état sur vieillissement. La direction de projection est [101]<sub>Al</sub>.

L'OR entre l'interphase et la matrice d'Al OR5:  $[1\bar{1}00]_{IP} // [101]_{Al}$ ,  $(11\bar{2}0)_{IP} // (11\bar{1})_{Al}$ ,  $(\bar{1}\bar{1}24)_{IP}$  3° de  $(\bar{2}02)_{Al}$ ,  $(11\bar{2}8)_{IP}$  3° de  $(020)_{Al}$  et l'OR entre TiB<sub>2</sub> et l'interphase OR6:  $[2\bar{1}\bar{1}0]_{TiB_2} // [1\bar{1}00]_{IP}$ ,  $(0001)_{TiB_2} // (0008)_{IP}$ ,  $(01\bar{1}0)_{TiB_2} // (11\bar{2}0)_{IP}$  sont révélées (Fig. 4.8).

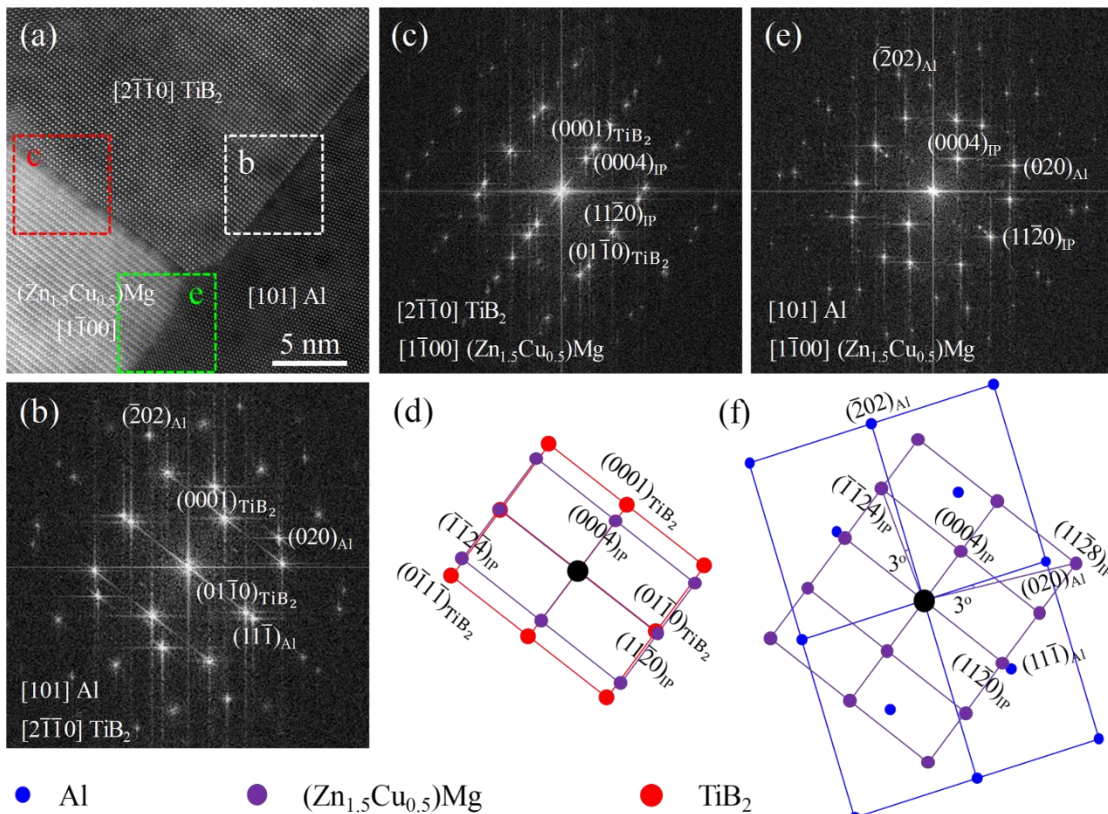


Fig. 4.8 (a) Image HRSTEM-HAADF montrant les multi-interfaces Al/IP/TiB<sub>2</sub> au niveau de l'OR2. (b), (c) et (e) des motifs FFT correspondants de zones de boîtes à savoir b, c et e donnés en (a) montrant les ORs mutuelles entre la nanoparticule TiB<sub>2</sub>, l'interphase et la matrice d'Al ; (d) et (f) des motifs simulés correspondant respectivement à (c) et (e). La direction de projection est  $[2\bar{1}\bar{1}0]_{\text{TiB}_2} // [1\bar{1}00]_{\text{IP}} // [101]_{\text{Al}}$ .

La structure atomique des interfaces multiples Al/(Zn<sub>1.5</sub>Cu<sub>0.5</sub>)Mg interphase/TiB<sub>2</sub> est caractérisée. Selon la Fig.4.9, l'interphase croît également sur la base des plans  $(0008)_{\text{IP}}$  dans la direction de croissance  $\langle 0001 \rangle_{\text{IP}}$ . L'interphase est complètement développée et aucune HGZ n'a été observée. Les interfaces Al/interphase sont composées d'une interface en forme d'arc dans le front de croissance et  $(\bar{1}11)_{\text{Al}} // (11\bar{2}0)_{\text{IP}}$  plans, et leur interface inadaptée est de 9.40 % et 20.10 %, respectivement. D'après la Fig. 4.10, l'interface entre l'interphase et TiB<sub>2</sub> est  $(11\bar{2}0)_{\text{IP}} // (01\bar{1}0)_{\text{TiB}_2}$  plans, et l'interface est inadaptée à 2.34 %.

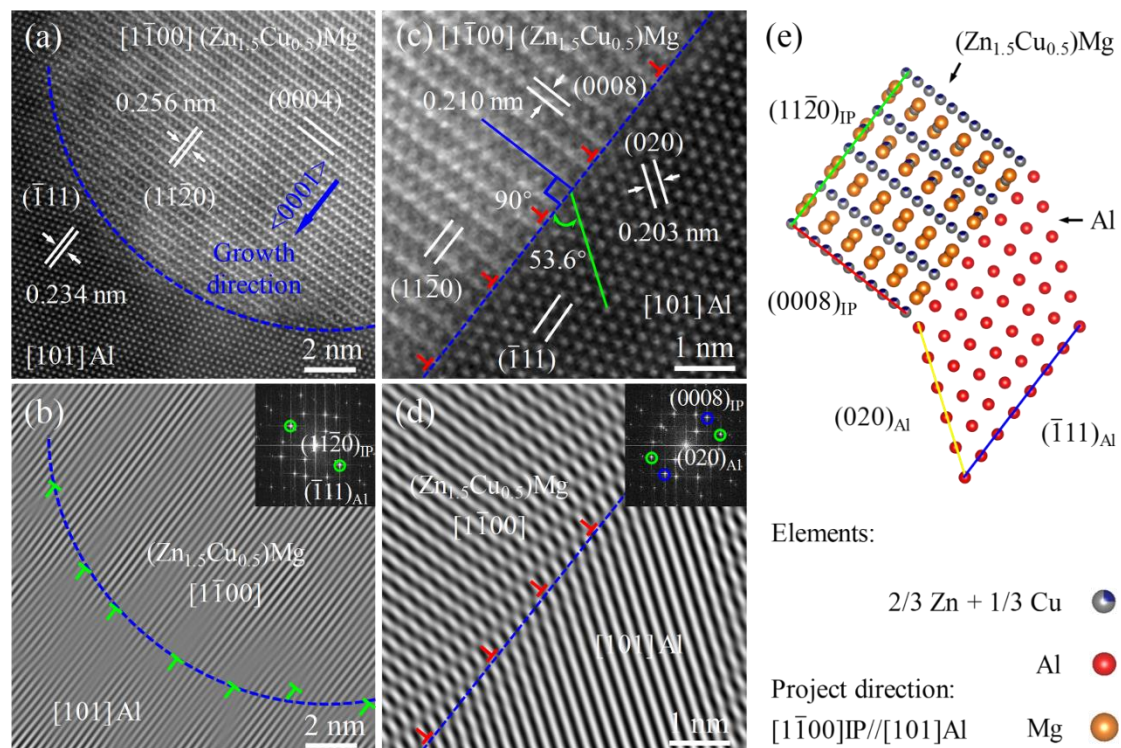


Fig. 4.9 Images HRSTEM-HAADF montrant la structure atomique des interfaces Al/IP au niveau de l'OR2 : (a) l'interface en forme d'arc au front de croissance de l'interphase et (c) l'interface  $(\bar{1}11)_{\text{Al}} // (11\bar{2}0)_{\text{IP}}$ . (b) et (d) des motifs FFT inverses de (a) et (c) en utilisant différentes paires de réflexions sélectionnées dans des motifs FFT correspondants, et (e) des modèles de structure atomique simulés montrant l'interface Al/IP  $(\bar{1}11)_{\text{Al}} // (11\bar{2}0)_{\text{IP}}$ .

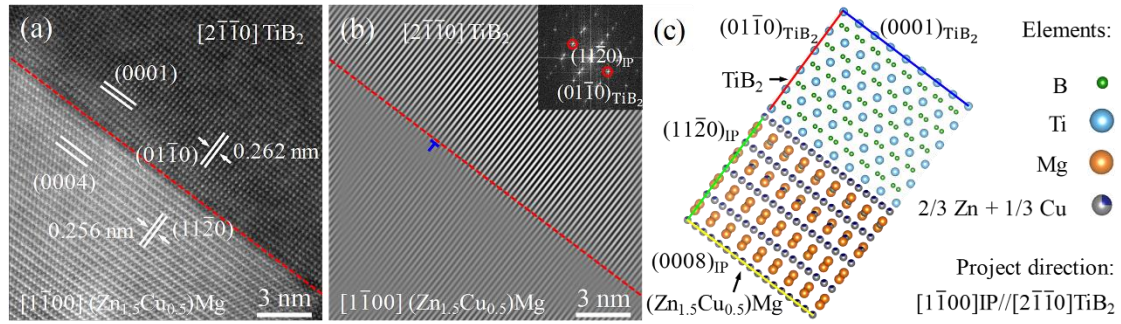


Fig. 4.10 (a) Image HRSTEM-HAADF montrant la structure atomique de l'interface IP/TiB<sub>2</sub> au niveau de l'OR2. (b) motif FFT inverse de (a) utilisant de paires de réflexions sélectionnées dans le motif FFT correspondant en médaillon et (c) modèle de structure atomique simulé montrant l'interface IP/TiB<sub>2</sub> (0001)<sub>TiB<sub>2</sub></sub>//(0008)<sub>IP</sub>. La direction de projection est [2 $\bar{1}\bar{1}$ 0]<sub>TiB<sub>2</sub></sub>// [1 $\bar{1}$ 00]<sub>IP</sub>.

## 4.2 Discussion

En résumé, ces résultats indiquent que les interfaces TiB<sub>2</sub>/Al sont les sites favorables aux réactions de précipitation. L'interphase est identifiée comme étant la phase (Zn<sub>1.5</sub>Cu<sub>0.5</sub>)Mg à l'état de vieillissement ou sur vieillissement. Les ORs de l'interphase ne sont liés qu'aux ORs initiaux OR1 et OR2 entre la nanoparticule TiB<sub>2</sub> et la matrice d'Al à l'état solide, alors qu'aucune corrélation avec les traitements de vieillissement (pic- ou sur vieillissement) n'est mise en évidence. La principale différence est que la HGZ n'existe qu'au front de croissance de l'interphase à l'état de vieillissement. Comparativement, dans la matrice de l'alliage d'aluminium en dehors de l'interface, la séquence de précipitations observée correspond aux résultats bien documentés dans l'alliage Al-Zn-Mg-Cu non renforcé. Les mécanismes sous-jacents correspondants des réactions de précipitation à l'interface sont examinés en détail ci-dessous.

### 4.2.1 Barrière énergétique de nucléation réduite pour la précipitation interphase

La relation entre  $\Delta G_{hom}^*$  et  $\Delta G_{het}^*$  peut être exprimée par  $\Delta G_{het}^*/\Delta G_{hom}^* = \frac{1}{4}(2 - 3\cos\theta + \cos\theta^3) = f(\theta)$ . L'angle de contact entre l'interphase et le substrat TiB<sub>2</sub> est mesuré à 60°. Ainsi,  $f(\theta)$  est calculé de 0.156. Évidemment, la barrière énergétique pour les précipitations hétérogènes à l'interface TiB<sub>2</sub>/Al est considérablement réduite par rapport à la nucléation homogène dans la matrice d'Al en dehors de l'interface.

### 4.2.2 Taux de croissance accéléré des précipitations interphases

Comme proposé par les études précédentes, la distorsion du réseau près des noyaux de dislocations diminue effectivement l'énergie d'activation pour la diffusion des atomes solutés. Les noyaux de dislocation peuvent agir comme des voies de diffusion rapide pour les atomes solutés permettant la croissance rapide des précipités et favorisant la précipitation des précipités à l'échelle nanométrique. Dans ce cas, les dislocations inadaptées se présentant à l'interface semi-cohérente  $\text{TiB}_2/\text{Al}$  ont contribué à l'accélération de la croissance de l'interphase.

#### **4.2.3 Interfaces $\text{TiB}_2/\text{Al}$ préférentielles pour la suppression de la précipitation interphase**

Le processus de précipitation dépend uniquement des ORs de l'interface  $\text{TiB}_2/\text{Al}$ . A l'OR1, l'interphase est formée préférentiellement aux facettes prismatiques  $\{01\bar{1}0\}$  et pyramidales  $\{01\bar{1}1\}$  de la nanoparticule  $\text{TiB}_2$ , tandis que, à l'OR2, elle est formée aux facettes basales  $\{0001\}$ . La caractéristique commune est que la suppression des précipitations interphasiques aux interfaces  $\text{TiB}_2/\text{Al}$  est parallèle aux plans  $\{111\}$  de la matrice d'Al. Ceci est causé par la formation d'une interface cohérente et dense entre le germe de l'interphase hcp et la matrice fcc d'Al qui se forme pendant la phase de nucléation. La croissance au niveau de l'interface cohérente entre la germe et l'interface est très difficile en raison de facteurs d'accommodation très faibles et de la faible mobilité.

#### **4.2.4 Cinétique des ORs cristallographiques entre les nanoparticules de $\text{TiB}_2$ , l'interphase et la matrice Al**

Lorsque ces trois cristaux ont les ORs observés, les interfaces Al/IP et IP/ $\text{TiB}_2$  peuvent être suffisamment compatibles pour acquérir la barrière de nucléation la plus basse.

#### **4.2.5 Influence des conditions de vieillissement**

Il est bien connu que la précipitation dans les alliages Al-Zn-Mg(-Cu) implique la formation de précipités ayant une composition différente de celle de la matrice, ce qui nécessite une diffusion à longue distance. Il s'agit d'un processus de transformation de phase continu et long, caractérisé par des mouvements atomiques activés thermiquement. Ainsi, une zone HGZ transitoire métastable devrait toujours exister sur le front de la croissance tant que le processus de transformation de phase n'est pas

complètement achevé à l'état de vieillissement. A l'état sur vieillissement, le coefficient de diffusion des atomes solutés est significativement augmenté car il augmente exponentiellement avec la température. Il en résulte l'interphase stable finale sans la HGZ.

## Chapitre 5 Effets des précipitations interfaciales sur les propriétés de traction du nanocomposite $\text{TiB}_2/\text{Al-Zn-Mg-Cu}$

### 5.1 Résultats

Les nanocomposites  $\text{TiB}_2/\text{Al-Zn-Mg-Cu}$  présente une remarquable combinaison de résistance (limite élastique de 600 MPa) et de ductilité (allongement uniforme de 12 %), ce qui est supérieur à tous les matériaux à base d'aluminium jamais signalés (Fig. 5.1).

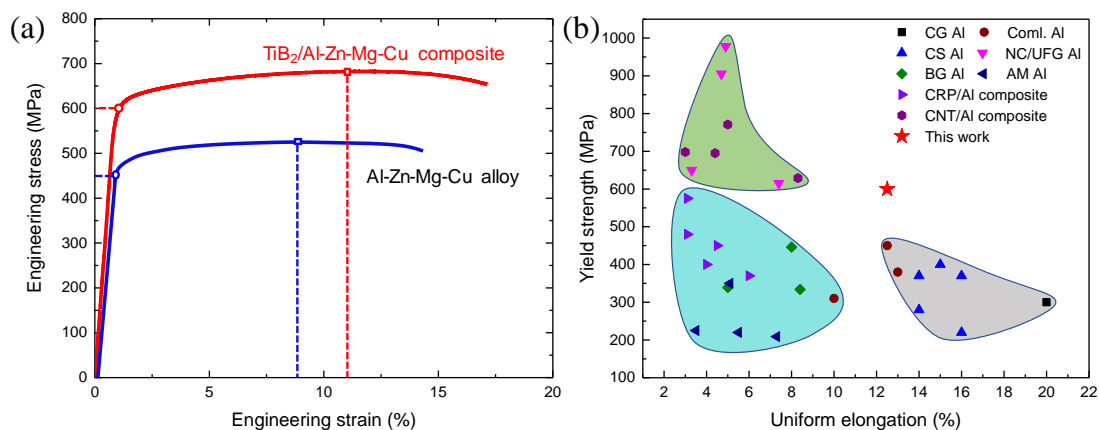


Fig. 5.1 (a) Courbes de contrainte-déformation en traction pour les nanocomposites de  $\text{TiB}_2/\text{Al-Zn-Mg-Cu}$  trempés dans l'eau et les alliages commerciaux d' $\text{Al-Zn-Mg-Cu}$ . b) Un résumé de la limite d'élasticité par rapport à l'allongement uniforme pour divers matériaux d'aluminium, Dans la Fig. 5.2, on a regroupé les résultats issus des différents alliages, tels que les alliages d'aluminium à gros grains (CG Al), les nanocristaux/alliages à grains ultra-fins (NC/UFG Al), les alliages d'aluminium à grains bimodaux (BG Al), les alliages d'aluminium de fabrication additif (AM Al), les composites matriciels en alliage d'aluminium renforcé par MRP (composites MRP/Al), les composites matriciels en alliage d'aluminium renforcé par nano-tube de carbone (composites CNT/Al) et les nanocomposites  $\text{TiB}_2/\text{Al-Zn-Mg-Cu}$  (Ce travail).

### 5.2 Discussion

#### 5.2.1 Renforcement de l'interface assisté par la précipitation

Selon le chapitre 4, la majorité des nanoparticules de  $TiB_2$  ont des OR1 avec la matrice Al. A l'état OR1, les interfaces  $TiB_2/Al$  à haut désaccord avec des contraintes de cohérence élevées sont transformées en interfaces Al/interphase/ $TiB_2$  multi-interfaces à faible désaccord. Il est bien établi que les dislocations inadaptées aux interfaces de phase créent de grandes tensions de cohérence, ce qui peut à son tour favoriser l'initiation de fissures sous contrainte. De même, la réduction de l'inadéquation des interfaces de phase peut être un moyen efficace de renforcer les interfaces de phase. Les interfaces  $TiB_2/Al$  sont ainsi fortement renforcées par la précipitation d'interface hétérogène, qui est proposée comme renforcement d'interface assisté par précipitation (Fig. 5.2).

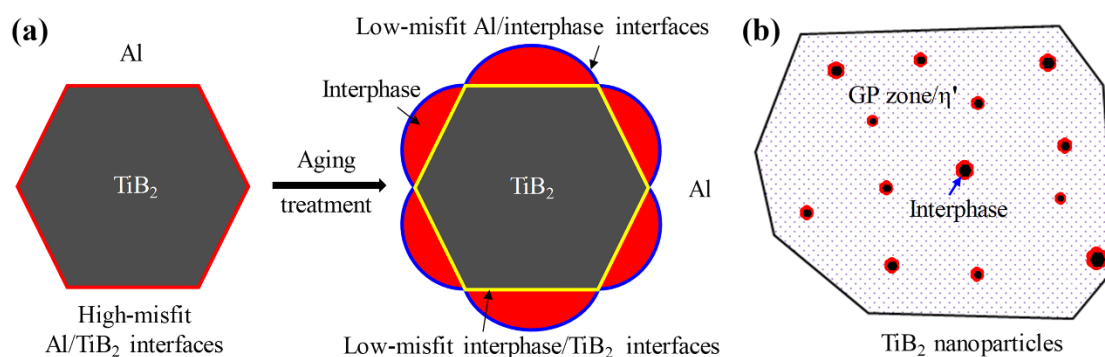


Fig. 5.2 Représentation schématique indiquant (a) l'évolution de l'interface  $TiB_2/Al$  pendant le traitement de vieillissement et (b) les précipitations intragranulaires globales des nanocomposite  $TiB_2/Al-Zn-Mg-Cu$ .

### 5.2.2 Mécanisme de renforcement pour une résistance accrue

Une forte liaison interfaciale entre les nanoparticules et la matrice est favorable au renforcement efficace de la résistance portante et, par conséquent, à l'amélioration de la résistance du composite. La forte adhérence de l'interphase  $Al/(Zn_{1.5}Cu_{0.5})Mg$  et des interfaces multiples  $TiB_2$  contribue donc grandement à la résistance à la traction du nanocomposite  $TiB_2/Al-Zn-Mg-Cu$ .

### 5.2.3 Mécanisme de renforcement pour l'amélioration de la ductilité

Pendant la déformation plastique des nanocomposite  $TiB_2/Al-Zn-Mg-Cu$ , les nanoparticules de  $TiB_2$  uniformément réparties peuvent bloquer/stocker efficacement les dislocations (Fig. 5.3a). Lorsque les dislocations contournent ces nanoparticules de  $TiB_2$ , des boucles de dislocation sont générées et introduites dans la matrice Al (Fig. 5.3b). Ces effets conduisent à une vitesse de trempe élevée permettant de retarder la

déformation localisée (colmatage) sous contrainte de traction, ce qui est essentiel pour un bon allongement uniforme.

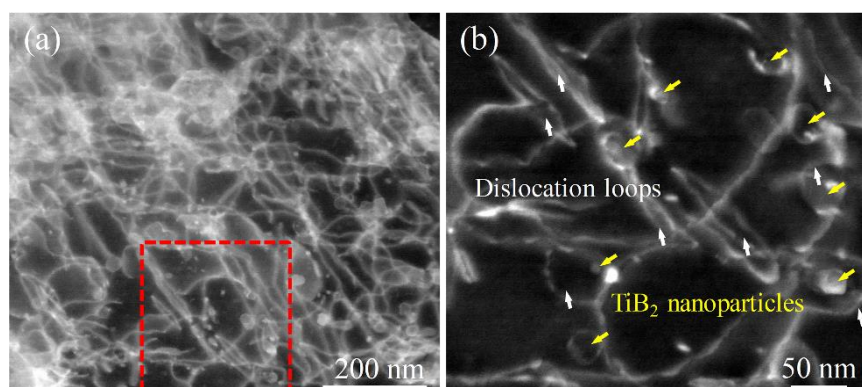


Fig. 5.3 (a) Image STEM à champ sombre des nanocomposite  $\text{TiB}_2/\text{Al-Zn-Mg-Cu}$  à une déformation de 1.5%. b) Image à plus fort grossissement de la zone du rectangle rouge en (a). Les flèches jaunes et blanches marquent respectivement les nanoparticules de  $\text{TiB}_2$  et les boucles de dislocation générées par l'interaction dislocation/ $\text{TiB}_2$ .

Comme montre dans la Fig. 5.4, si le PAIS ne se produit pas aux interfaces  $\text{TiB}_2/\text{Al}$ , la forte densité de dislocations doit s'accumuler directement aux interfaces  $\text{TiB}_2/\text{Al}$ . En même temps que la déformation plastique se poursuit, un nombre croissant de dislocations doivent être piégées et s'accumuler aux interfaces  $\text{TiB}_2/\text{Al}$ . Lorsque la contrainte aux interfaces atteint le seuil que les interfaces peuvent supporter, le décollement interfacial se produit et la déformation localisée (colmatage) a eu lieu par la suite. En ce qui concerne les interfaces  $\text{TiB}_2/\text{Al}$  avec PAIS (c'est-à-dire l'interphase  $\text{Al}/(\text{Zn}_{1.5}\text{Cu}_{0.5})\text{Mg}$  et les interfaces multi-interfaces  $\text{TiB}_2$ ), la forte densité de dislocations doit s'accumuler aux interfaces  $\text{Al}/\text{interphase}$  à faible inadéquation car elles ne peuvent couper l'interphase  $(\text{Zn}_{1.5}\text{Cu}_{0.5})\text{Mg}$ . Si l'on considère que la résistance des interfaces  $\text{Al}/\text{interphase}$  à faible défaut d'adaptation est beaucoup plus élevée que celle des interfaces  $\text{TiB}_2/\text{Al}$  à défaut d'adaptation élevé, le décollement de l'interface et la déformation localisée qui en résulte sont ainsi retardés. Par conséquent, la déformation uniforme des nanocomposites  $\text{TiB}_2/\text{Al-Zn-Mg-Cu}$  est grandement améliorée.

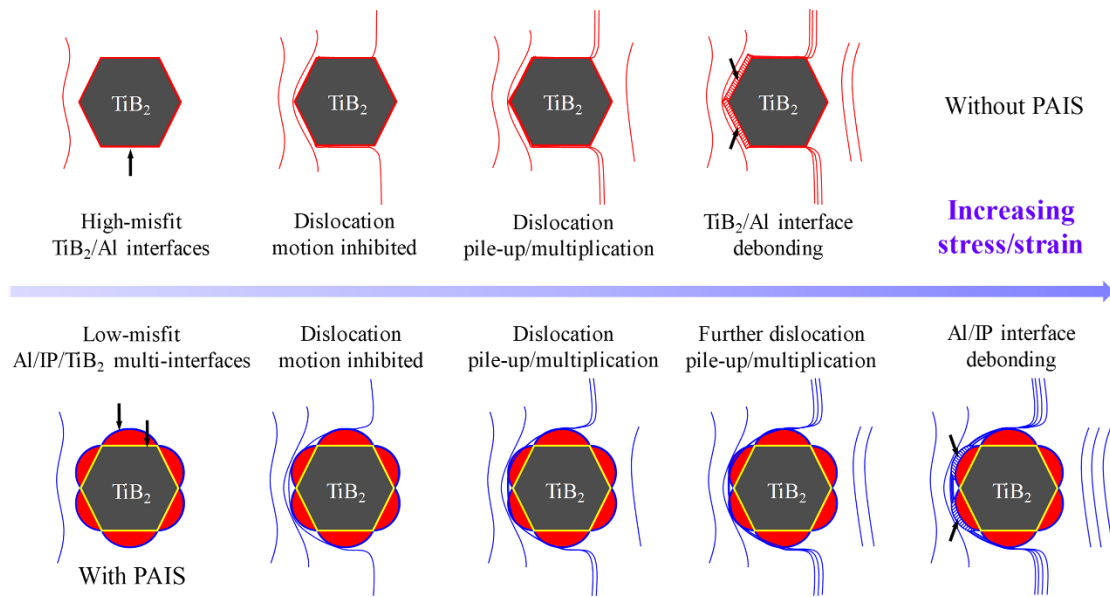


Fig. 5.4 Schéma indiquant l'interaction  $TiB_2$ /dislocation avec et sans PAIS pendant la déformation plastique.

## Chapitre 6 Étude des mécanismes des nanoparticules influençant la croissance des fissures de fatigue dans le composite $TiB_2/Al-Zn-Mg-Cu$

### 6.1 Résultats

#### 6.1.1 Microstructure

Comme montre dans la Fig. 6.1, en raison de l'absence de FSP, la plupart des particules de  $TiB_2$  sont agglomérées aux joints de grains (GBs) présentant une morphologie de bandes de  $TiB_2$  d'une largeur de  $\sim 5-15 \mu m$ . Seules quelques particules de  $TiB_2$  se trouvent dans la zone interbande, qui est considérée comme la zone pauvre en  $TiB_2$ . La granulométrie moyenne des nanocomposites  $TiB_2/Al-Zn-Mg-Cu$  est beaucoup plus fine que celle de l'alliage  $Al-Zn-Mg-Cu$ .

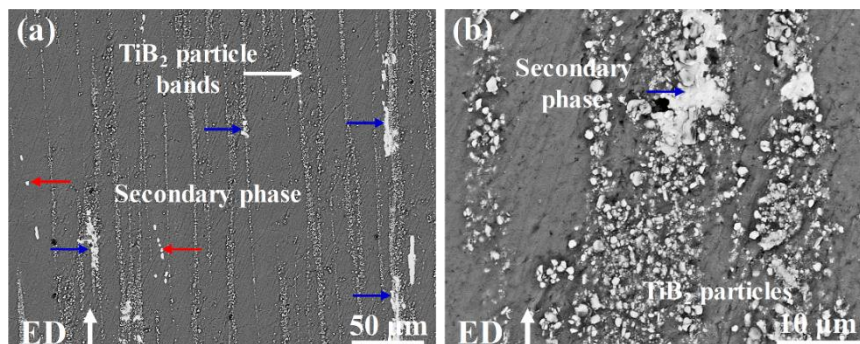


Fig. 6.1 (a) Morphologie typique des nanocomposites  $\text{TiB}_2/\text{Al-Zn-Mg-Cu}$  le long de ED ; (b) image à plus fort grossissement des bandes  $\text{TiB}_2$  en (a).

### 6.1.2 Taux de croissance des fissures de fatigue

Les propriétés de FCG des nanocomposites  $\text{TiB}_2/\text{Al-Zn-Mg-Cu}$  et de l'alliage  $\text{Al-Zn-Mg-Cu}$  non renforcé ont été obtenues (Fig. 6.2). Au stade I ( $6.5 \text{ MPa}\cdot\text{m}^{1/2} < \Delta K < 9.5 \text{ MPa}\cdot\text{m}^{1/2}$ ), les nanocomposites  $\text{TiB}_2/\text{Al-Zn-Mg-Cu}$  présentent un taux de FCG plus faible que l'alliage  $\text{Al-Zn-Mg-Cu}$ . Au stade II ( $9.5 \text{ MPa}\cdot\text{m}^{1/2} \leq \Delta K \leq 21 \text{ MPa}\cdot\text{m}^{1/2}$ ), les nanocomposites  $\text{TiB}_2/\text{Al-Zn-Mg-Cu}$  montrent le même taux de FCG que l'alliage  $\text{Al-Zn-Mg-Cu}$ . Au stade III ( $\Delta K > 21 \text{ MPa}\cdot\text{m}^{1/2}$ ), les nanocomposites  $\text{TiB}_2/\text{Al-Zn-Mg-Cu}$  présentent un taux de FCG plus élevé que l'alliage  $\text{Al-Zn-Mg-Cu}$ .

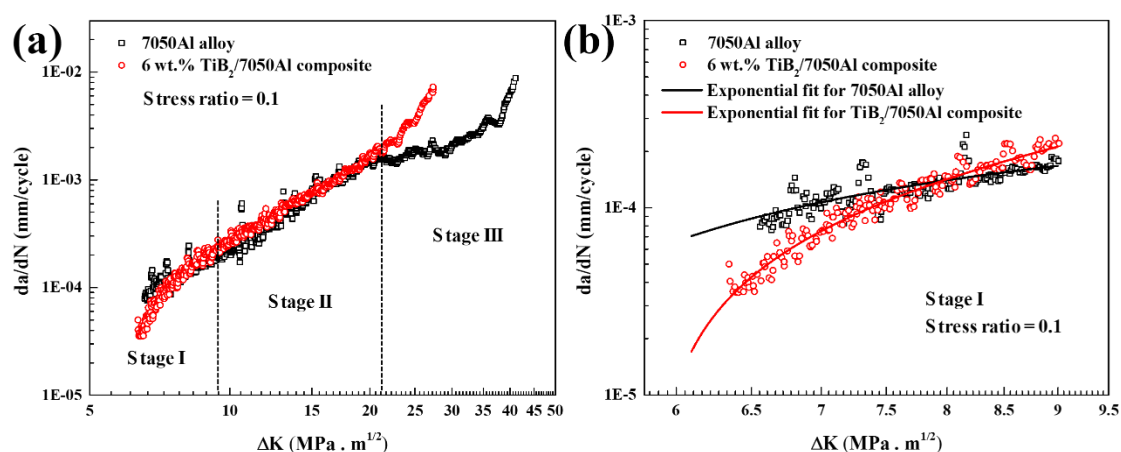


Fig. 6.2 (a) Courbes  $da/dN$  globales par rapport à  $\Delta K$  des nanocomposites  $\text{TiB}_2/\text{Al-Zn-Mg-Cu}$  et de l'alliage  $\text{Al-Zn-Mg-Cu}$ . (b) Les courbes  $da/dN$  versus  $\Delta K$  et les courbes d'ajustement exponentielles correspondantes des nanocomposites  $\text{TiB}_2/\text{Al-Zn-Mg-Cu}$  et de l'alliage  $\text{Al-Zn-Mg-Cu}$  en phase I pour mieux montrer le comportement de la FCG à faible  $\Delta K$ . Le rapport de contrainte est de 0.1.

### 6.1.3 Caractéristiques fractographiques de la propagation des fissures

Les caractéristiques fractographiques de la propagation des fissures ont été caractérisées. A faible  $\Delta K$ , on observe des schémas de clivage typiques des rivières et des zones de protubérance (Fig. 6.3a). La répartition des zones d'avancement est conforme à la répartition des clusters  $\text{TiB}_2$ . La phase S fracturée et plusieurs particules de  $\text{TiB}_2$  sont observées dans les zones d'avancement (Fig. 6.3b). Dans l'intervalle intermédiaire de  $\Delta K$ , on observe des schémas de clivage typiques des rivières et des zones d'amas de  $\text{TiB}_2$  avec les observations fractographiques (Fig. 6.3c). La phase S

fracturée est observée dans les zones d'amas de  $\text{TiB}_2$ . Une densité élevée de particules de  $\text{TiB}_2$  se trouve dans les zones de concentration de  $\text{TiB}_2$  (Fig. 6.3d). Notamment, on n'observe pas de crêtes de déchirure évidentes ou de fossettes profondes autour des particules de  $\text{TiB}_2$  (Fig. 6.3d). A grande valeur de  $\Delta K$ , les observations fractographiques montrent de stries et de zones de fossettes distribuées alternativement (Fig. 6.3e). Les zones de fossettes présentent une forte densité de crêtes de déchirure et de fossettes profondes interconnectées (Fig. 6.3f). Des particules de  $\text{TiB}_2$  sont observées à l'intérieur des poches à fossettes (Fig. 6.3f).

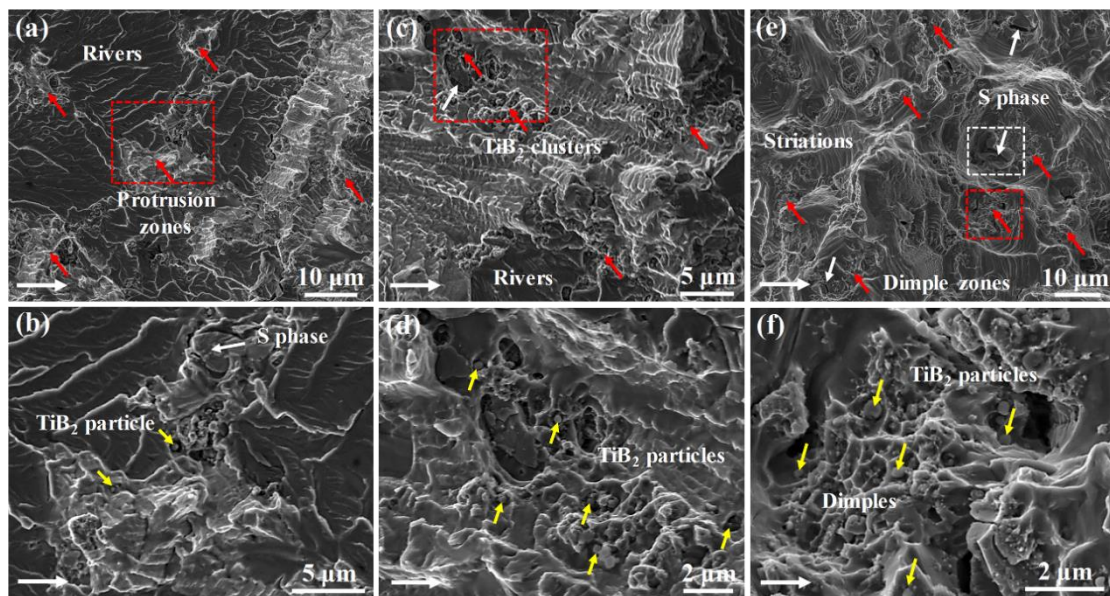


Fig. 6.3 (a) Caractéristiques fractographiques du FCG à faible  $\Delta K$  (b) Image à plus fort grossissement des zones d'avancement marquées d'un carré rouge en (a). (c) Caractéristiques fractographiques de la FCG à une valeur intermédiaire de  $\Delta K$ . (d) Image à plus fort grossissement des zones d'avancement marquées d'un carré rouge en (c). (e) Observations fractographiques de la FCG à une valeur intermédiaire de  $\Delta K$ . (f) Image à plus fort grossissement des zones d'avancement marquées d'un carré rouge en (e).

## 6.2 Discussion

Pour le nanocomposite  $\text{TiB}_2/\text{Al-Zn-Mg-Cu}$ , les fissures de fatigue doivent se propager à travers deux microstructures distinctes sous la contrainte cyclique : (1) Zones pauvres en  $\text{TiB}_2$  à l'intérieur des grains ; (2) Bandes de  $\text{TiB}_2$  coexistant avec les joints de grains (GBs). Par conséquent, le comportement des FCG et les mécanismes correspondants dans ces deux zones distinctes sont complètement différents, et nous

allons en discuter séparément.

### 6.2.1 FCG à l'intérieur des grains

La réduction de la taille des grains entraîne une augmentation du taux de FCG lorsque la taille de la zone plastique cyclique est plus grande que la taille des grains. Dans la présente étude, les tailles de la zone plastique cyclique de l'alliage Al-Zn-Mg-Cu et des nanocomposites TiB<sub>2</sub>/Al-Zn-Mg-Cu sont inférieures à leur propre taille de grain. Par conséquent, l'alliage Al-Zn-Mg-Cu et les nanocomposites TiB<sub>2</sub>/Al-Zn-Mg-Cu devraient avoir un taux de FCG similaire à l'intérieur des grains avec une valeur de  $\Delta K$  basse. Sur la plage intermédiaire de  $\Delta K$ , la taille de la zone plastique cyclique des nanocomposites TiB<sub>2</sub>/Al-Zn-Mg-Cu est supérieure à la taille moyenne des grains. A plus forte valeur de  $\Delta K$ , la taille de la zone plastique cyclique de l'alliage Al-Zn-Mg-Cu et des nanocomposites TiB<sub>2</sub>/Al-Zn-Mg-Cu est supérieure à leur taille moyenne de grain. Par conséquent, par rapport à l'alliage Al-Zn-Mg-Cu, le taux de FCG des nanocomposites TiB<sub>2</sub>/Al-Zn-Mg-Cu est augmenté à l'intérieur des grains en raison de la taille réduite des grains dans la gamme intermédiaire et élevée de  $\Delta K$ .

### 6.2.2 FCG aux GBs

Tout d'abord, on observe une réduction du taux de FCG dans la plage de petite valeur de  $\Delta K$  (Fig. 6.4a-c). A ce stade, la contrainte dans la zone plastique cyclique est relativement faible. Les particules de TiB<sub>2</sub> peuvent favoriser la déflexion des fissures et l'augmentation de la rugosité de la surface de fracture qui en résulte. Il devrait en résulter une fermeture des fissures induite par la rugosité et une meilleure résistance de FCG des nanocomposites TiB<sub>2</sub>/Al-Zn-Mg-Cu.

Deuxièmement, une réduction du taux de FCG dans la plage intermédiaire de  $\Delta K$  (Fig. 6.4d-f) est observée dans la phase II, la valeur de  $\Delta K$  est supérieure à celle de la phase I. La contrainte dans cette zone plastique cyclique est augmentée. Lorsque l'extrémité de la fissure de fatigue s'approche des bandes de TiB<sub>2</sub>, les particules de TiB<sub>2</sub> doivent empêcher la fissure d'avancer en s'inclinant autour des obstacles. Ceci devrait permettre d'améliorer la résistance FCG des nanocomposites TiB<sub>2</sub>/Al-Zn-Mg-Cu.

Troisièmement, le taux de FCG a augmenté dans la plage importante de  $\Delta K$  (Fig. 6.4g-i). La contrainte cyclique dans la zone plastique cyclique est sévèrement augmentée à une valeur élevée de  $\Delta K$  par rapport aux phases I et II. Pendant le processus de chargement cyclique en fatigue, la déformation plastique effective près de

l'interface  $TiB_2/Al$  doit être libérée par décollement interfacial. La fissure de fatigue se propage donc par la conjonction des micropores qui se produisent simultanément au cours de ce processus, ce qui augmente considérablement le taux de FCG des nanocomposites  $TiB_2/Al-Zn-Mg-Cu$  en GBs.

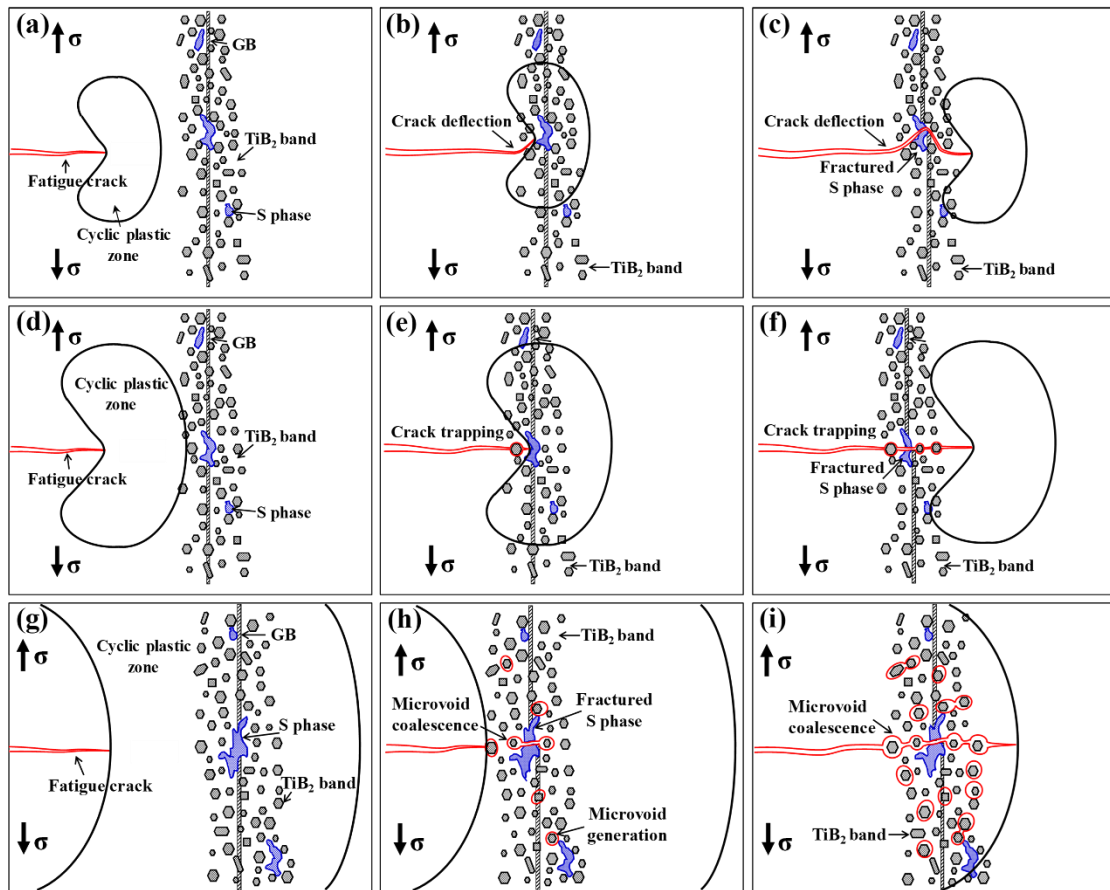


Fig. 6.4 Représentation schématique des caractéristiques de la trajectoire de FCG des nanocomposites  $TiB_2/Al-Zn-Mg-Cu$ . (a-c) à faible valeur de  $\Delta K$ , montrant la fissure de fatigue se propageant à l'intérieur des grains, entravée par la bande de  $TiB_2$  et passée à travers la bande de  $TiB_2$  par déflexion de fissure, en conséquence ; (d-f) à une valeur intermédiaire de  $\Delta K$ , montrant la fissure de fatigue se propageant à l'intérieur des grains, emprisonnée par la bande de  $TiB_2$  et passée à travers la bande de  $TiB_2$  par piégeage de fissure, en conséquence ; (g-i) à haute valeur de  $\Delta K$ , présentant la fissure de fatigue se propageant à l'intérieur des grains, reliée aux micropores générés à l'intérieur de la bande  $TiB_2$  et passés à travers la bande  $TiB_2$  par coalescence des micropores, en conséquence.